NEW STRATEGIES FOR TAGGING QUANTUM DOTS FOR DYNAMIC CELLULAR IMAGING

A Dissertation
Presented to
The Academic Faculty

by

Mary M. Wen

In Partial Fulfillment
of the Requirements for the Degree
Doctor of Philosophy in the
School of Biomedical Engineering

Georgia Institute of Technology
August 2013

NEW STRATEGIES FOR TAGGING QUANTUM DOTS FOR DYNAMIC CELLULAR IMAGING

Approved by:

Dr. Shuming Nie, Advisor
School of Biomedical Engineering
Georgia Institute of Technology

Dr. Alfred Merrill
School of Biology
Georgia Institute of Technology

Dr. Gang Bao
School of Biomedical Engineering
Georgia Institute of Technology

Dr. Philip Santangelo
School of Biomedical Engineering
Georgia Institute of Technology

Dr. Hanjoong Jo
School of Biomedical Engineering
Georgia Institute of Technology

Date Approved: April 11, 2013

To my Father and my Mother

ACKNOWLEDGEMENTS

First, I would like to thank my advisor, Dr. Shuming Nie, for his guidance and support throughout my graduate work. I am grateful to have had the opportunity to start my career by working under one of the world's famous experts in nanotechnology. Second, I would like to thank the members of my thesis committee, Dr. Gang Bao, Dr. Hanjoong Jo, Dr. Alfred Merrill, and Dr. Dr. Philip Santangelo for their insight in improving this thesis. I would especially like to thank Dr. Jo for his valuable advice and guidance throughout my graduate work. I am also deeply appreciative of Dr. Xiaoping Hu's support throughout my studies.

This project would not have been possible without the incredible generosity of Dr. Kate Qin Zhao and Dr. Tetsuo Uyeda of Promega Corporation, who provided HaloTag protein, cell, and ligands for this work. I would like to acknowledge Dr. Andrew Smith for providing quantum dots and for his help throughout this work, as well as the members of the Nie laboratory. Additionally, I would like to extend my gratitude to Ms. Michelle Denney, Ms. Elizabeth Caudle, and Ms. Cynthia Lewis-Webb, our lab administrators who worked tirelessly to ensure our research went smoothly.

I will always remain grateful to Brenda Robledo, Dr. Wakako Takabe, Junghwa Choi, and Pauline Che for their wonderful friendship. I would also like to thank all those who extended various acts of helpfulness to me in graduate school, including Dr. Xiaoyong Zhang, Mr. Dong won Kang, and members of the Jo lab. Each act of kindness, no matter how small, will always be remembered.

Finally, I would like to thank my family for their unconditional love and support: My father, Dr. Fu-chu Wen; my mother, Mrs. Rhoda Wen; and my brother, Daniel Wen. My father is my greatest mentor, and mother is my strongest advocate. This thesis would not have been completed without their guidance, encouragement, and the values of hard work and discipline they've always strived to instill in me.

TABLE OF CONTENTS

LIST OF TABLES

Page

LIST OF FIGURES

LIST OF SYMBOLS AND ABBREVIATIONS

ATP	Adenosine Triphosphate
BG	O^6-Benzylguanine
BRET	Bioluminescence Resonance Energy Transfer
BSA	Bovine Serum Albumin
cAMP	Cyclic Adenosine Monophosphate
CCD	Charge Coupled Device
Cd	Cadmium
CD	Cytoplasmic Domain
CdS	Cadmium Sulfide
CdSe	Cadmium Selenide
CdTe	Cadmium Telluride
CO_2	Carbon Dioxide
Da	Daltons
DHLA	Dihydrolipoic Acid
DLS	Dynamic Light Scattering
DMSO	Dimethyl Sulfoxide
DNA	Deoxyribonucleic Acid
EC	Extracellular Domain
EDC	1-Ethyl-3-(3-dimethylaminopropyl)carbodiimide
EGF	Epidermal Growth Factor
EM-CCD	Electron Multiplying Charge Coupled Device
erbB1	Epidermal Growth Factor Receptor
FBS	Fetal Bovine Serum

FITC	Fluorescein Isothiocyanate
FPALM	Fluorescence Photoactivation Localization Microscopy
FPLC	Fast Performance Liquid Chromatography
fps	Frames Per Second
FRAP	Fluorescence Recovery After Photobleaching
FRET	Fluorescence Resonance Energy Transfer
FWHM	Full Width Half Maximum
g	Gravity
hAGT	Human O^6-Alkylguanine Transferase
HEPES	4-(2-Hydroxyethyl)-1-piperazineethanesulfonic Acid
HIV	Human Immunodeficiency Virus
HTL	HaloTag Ligand
HTP	HaloTag Protein
InAs	Indium Arsenide
InP	Indium Phosphide
kDa	Kilodalton
K_D	Dissociation Constant
MES	2-(*N*-morpholino)ethanesulfonic Acid
MSD	Mean Squared Displacement
MW	Molecular Weight
MWCO	Molecular Weight Cutoff
NIH	National Institutes of Health
Ni-NTA	Nickel-Nitrilotriacetic Acid
NLS	Nuclear Localization Sequence
NMR	Nuclear Magnetic Resonance

PALM	Photoactivated Localization Microscopy
PBS	Phosphate Buffered Saline
PbS	Lead Sulfide
PbSe	Lead Selenide
PEG	Polyethylene Glycol
PEG-QD	Pegylated Quantum Dot
PEG-QD-HTL	Pegylated Quantum Dot- HaloTag Ligand
PSF	Point Spread Function
QD	Quantum Dot
QD-HTL	Quantum Dot-HaloTag Ligand
RESOLFT	Reversible Saturable Optically Linear Fluorescence Transitions
RGD	Arginylglycylaspartic Acid
rpm	Revolutions Per Minute
SDS-PAGE	Sodium Dodecyl Sulfate Polyacrylamide Gel Electrophoresis
SILAR	Successive Ion Layer Adsorption and Reaction
siRNA	Small Interfering Ribonucleic Acid
SNR	Signal-to-Noise Ratio
SP	Signal Peptide
STED	Stimulated Emission Depletion
STORM	Stochastic Optical Reconstruction Microscopy
TEM	Transmission Electron Microscopy
TIRFM	Total Internal Reflection Microscopy
TM	Transmembrane Domain
TMR	Tetramethyl Rhodamine
TRITC	Tetramethylrhodamine Isothiocyanate

UV	Ultraviolet
UV-Vis	Ultraviolet-Visible
v/v	Volume Per Volume
w/v	Weight Per Volume
Zn	Zinc
ZnS	Zinc Sulfide
ZnSe	Zinc Selenide

SUMMARY

In recent years, semiconductor quantum dots (QDs) have arisen as a new class of fluorescent probes that possess unique optical and electronic properties well-suited for single-molecule imaging of dynamic live cell processes. Nonetheless, the large size of conventional QD-ligand constructs has precluded their widespread use in single-molecule studies, especially on cell interiors. A typical QD-ligand construct can range upwards of 35 nm in diameter, well exceeding the size threshold for cytosolic diffusion and posing steric hindrance to binding cell receptors.

The objective of this research is to develop tagging strategies that allow QD-ligand conjugates to specifically bind their target proteins while maintaining a small overall construct size. To achieve this objective, we utilize the HaloTag protein (HTP) available from Promega Corporation, which reacts readily with a HaloTag ligand (HTL) to form a covalent bond. When HaloTag ligands are conjugated to size-minimized multidentate polymer coated QDs, compact QD-ligand constructs less than 15 nm in diameter can be produced. These quantum dot-HaloTag ligand (QD-HTL) conjugates can then be used to covalently bind and track cellular receptors genetically fused to the HaloTag protein.

In this study, size-minimized quantum dot-HaloTag ligand conjugates are synthesized and evaluated for their ability to bind specifically to purified and cellular HTP. The effect of QD-HTL surface modifications on different types of specific and nonspecific cellular binding are systematically investigated. We show that ligand length, ligand valency, polyethylene glycol (PEG) length, and PEG density are all important

factors that govern QD-HTL binding specificity. Once these QD surface parameters are optimized, QD-HTLs are indeed capable of specifically binding HaloTag protein. Finally, these QD-HTL conjugates are utilized for single-molecule imaging of dynamic live cell processes. By applying QD-HTLs to the tracking of cellular β1 integrin-HaloTag fusion proteins, we show that QD-HTLs convey accurate information about cellular protein dynamics while providing far greater luminescence and photostability than fluorescent dyes.

This work is significant because it is the first to synthesize size-minimized QD-HTL probes that bind specifically to HTP and to apply them for single-molecule imaging in living cells. Our results show that size-minimized QD-HTLs exhibit great promise as novel imaging probes for live cell imaging, allowing researchers to visualize cellular protein dynamics in remarkable detail.

CHAPTER 1

INTRODUCTION

1.1 Motivation

Ever since A.H. Coons developed the first methods to conjugate proteins to fluorophores in 1941 [1], and green fluorescent protein was successfully purified from *Aequorea Victoria* in the 1960s [2], fluorescent dyes and proteins have revolutionized the field of biology. Fluorescent dyes and proteins have since become instrumental tools for visualizing the dynamic behavior of biomolecules within living cells using light microscopy. Traditionally, researchers have studied receptor pathways using bulk-averaged measurements derived from whole cell populations of receptors labeled with fluorescent dyes or proteins. In reality, however, individual receptor processes are highly heterogeneous and can deviate greatly from ensemble behavior [3].

In recent years, single-molecule imaging has emerged as a powerful, highly sensitive method capable of providing a wealth of information normally obscured by ensemble averaging. The utility of single-molecule imaging can be illustrated by considering a classic example of a population of molecular beacons, half of which are quenched (closed), and half of which are fluorescent (open). In this example, an ensemble spectrum would not be able to distinguish whether 50% of the molecular beacon population is fully quenched, or whether 100% of the population is half-quenched. Single-molecule detection would not only provide this information, but would also allow the researcher to monitor the spatial and temporal resolution of the opening and closing [4].

Fluorescence imaging has always been an attractive option for single-molecule detection due to the ease of detecting a bright signal against a dark background. However, single-molecule imaging with fluorescent dyes and proteins is difficult to accomplish for several reasons. Foremost, it is technically challenging to achieve a good signal-to-noise ratio when tracking a solitary fluorophore in a complex biological environment. The signal of a single fluorophore can be greatly overpowered just by the Raman scatter from surrounding solvent molecules. For instance, the Raman scatter alone from 1 ml of pure water is already 10^{10} fold greater than the signal from one Rhodamine Green molecule. The background noise is further exacerbated by cellular autofluorescence and complex biological liquids in live cell applications. To diminish the effects of light scattering, a reduction in the surrounding volume (to usually at least 1 femtoliter) is necessary to obtain adequate signal from a single fluorophore [4].

As a means of reducing the detection volume to achieve higher signal-to-noise ratio, complex optical configurations such as total internal reflection microscopy (TIRFM) are commonly applied. To achieve this reduced volume, TIRFM uses an evanescent field, which limits the height of detection to ~100-200 nm [4-6]. One disadvantage of TIRFM is that imaging is consequently limited to close proximity of the cell membrane. Naturally, this would not be ideal for intracellular single-molecule tracking. Other optical setups for single-molecule fluorescence imaging include confocal and two-photon microscopy setups [4, 7], along with more recent super-resolution imaging techniques [8, 9]. Even with these special optical setups, fluorescent single-molecule imaging remains challenging due to the poor photostability of traditional fluorophores. Fluorescence emission from organic dyes and proteins decays very rapidly,

typically bleaching within 10 s, preventing single molecules from being tracked for long periods of time [10-12].

In recent years, inorganic quantum dots (QDs) have emerged as a promising alternative to traditional organic fluorophores, with many properties well-suited for single-molecule imaging. QDs have 10-100x higher extinction coefficients and 100-1000x greater photostability than fluorescent dyes and proteins. As a result, special optical setups are not needed to perform single-molecule imaging with QDs, and QDs can be tracked under a standard epifluorescence microscope for hours without photobleaching. [13-15].

Quantum dots have already found many promising applications in biology and medicine, including *in vivo* animal imaging [16-18], medical diagnostics [19-22], and cellular imaging [23, 24]. In the latter category, QDs have been used to track several types of cell membrane receptors, including G-protein coupled receptors [25], receptor tyrosine kinases [26, 27], and integrins [28, 29] through endocytic pathways. QDs have been delivered into cell cytoplasm by a variety of chemical and mechanical methods [30], and the subsequent interactions of the QD with the active transport machinery of the cell have been studied [31, 32]. Additionally, QDs have been coated with endosome-disrupting coatings to investigate potential mechanisms of nanoparticle delivery and release into cells [33].

However, applications of quantum dots in live cell imaging have remained limited because of the large size and cumbersome tagging strategies of traditional QD probes. The conventional approach for QD tagging is to conjugate the QD to an antibody that has a specific affinity for a protein of interest. Due the large QD surface area available for

coupling, multiple antibodies often bind each nanoparticle, resulting in a bulky structure capable of crosslinking several target proteins. Due to the stochastic nature of chemical conjugation, QDs often contain varied amounts of conjugated antibody on their surfaces, which may be attached in any number of different active or inactive geometric orientations. A typical commercial QD ranges from 15-35 nm in hydrodynamic diameter, and the presence of each surface protein or antibody can contribute an additional 4-15 nm to the total size. Altogether, these factors work together to produce a total QD construct that can reach up to 50 nm in diameter [34]. These bulky constructs pose steric hindrance to binding cell receptors and can crosslink multiple receptors, preventing the imaging of single molecules. They also are too large to diffuse freely inside crowded cellular regions such as the cell cytoplasm. As a result, QD imaging remains largely limited to the surfaces of cell membranes.

In addition to increasing QD probe size, conventional QD targeting approaches are less than ideal for single-molecule tracking. During cellular imaging, it is critical to insure that the QD-targeting ligand construct remains attached to the protein of interest. When antibodies are implemented, they bind to their targets with relatively weak affinity ($K_D = 10^{-6}$ to 10^{-9} M) and may dissociate from proteins of interest during prolonged tracking studies [35].

In this thesis, we seek to address the existing problems with QD size and QD targeting so that quantum dots can obtain greater applicability in dynamic live cell imaging. Recently, several new tagging strategies have emerged that allow fluorophores to bind covalently to their targets [36-39]. Many of these techniques have been previously used with dyes, but very few have yet been implemented or optimized with QDs. These

tagging strategies provide novel approaches for tracking cellular proteins, and have the potential to alleviate many current disadvantages associated with traditional QD probes.

1.2 Dissertation Objective

The focus of this research is to develop QD-tagging strategies that allow QD-ligand conjugates to specifically bind their target proteins while still maintaining a small overall construct size. Our long-term goal is to engineer an ideal QD probe that can be successfully used for dynamic single-molecule imaging of cellular processes in living cells. The rationale is that small QD-targeting ligand constructs are necessary to diffuse in cell interiors, and that a covalent strategy is ideal for preventing dissociation of the QD from the protein of interest. We propose to utilize the HaloTag protein (HTP), a 33 kDa protein commercially available from Promega Corporation that reacts readily with a chloroalkane moiety, or "HaloTag ligand" (HTL), to form a covalent bond [40]. We hypothesize that QDs displaying surface HaloTag ligands will retain the ability to covalently bind cellular proteins of interest genetically fused to a HaloTag protein, thereby providing a new strategy for implementing QDs for single-molecule imaging.

1.3 Dissertation Organization

This dissertation is organized as follows:

In this chapter we have described the importance of live cell imaging in biomedical research and provided an overview of the applications of QDs in live cell imaging.

Chapter 2 will provide background information on the physical properties of quantum dots and their advantages over fluorescent dyes for live cell imaging. We will

discuss traditional methods for QD synthesis and bioconjugation along with opportunities for improvement in the next generation of QDs.

Chapter 3 will discuss the benefits of size-minimized QDs for cellular imaging and highlight some of the current research strategies to reduce quantum dot size and improve tagging strategies. We will present our own research strategy in choosing to use size-minimized multidentate-polymer coated QDs with HaloTag ligands for the purpose of engineering a QD-based probe for dynamic live cell imaging.

In Chapter 4 we discuss the procedures for synthesizing QD-HaloTag ligand conjugates and characterize their ability to bind purified HaloTag proteins *in vitro*.

In Chapter 5 we evaluate the ability of QD-HaloTag ligand conjugates to specifically bind cellular targets.

In Chapter 6 we investigate the use of QD-HaloTag ligand conjugates for single-molecule imaging of dynamic cellular processes.

Finally, in Chapter 7, we summarize the major findings from our study and present future opportunities for application of this technology.

CHAPTER 2

QUANTUM DOTS FOR LIVE CELL IMAGING

2.1 Introduction

Nanotechnology is an exciting field with tremendous potential to revolutionize human life by creating new technologies in electronics, energy production, and medicine. It is a multidisciplinary field that uses chemistry, material science, and engineering to manipulate materials with one or more dimensions sized less than 100 nanometers. In particular, the field of biomedicine is poised to greatly benefit from nanotechnology, since several cellular structures including proteins and DNA fall within the "nano" size regime [41].

Recent advances in nanotechnology have led to the development of various novel structures such as magnetic nanoparticles, carbon nanotubes, and quantum dots. Due to their small size and large surface area-to-volume ratio, nanostructures exhibit several unique properties compared to bulk materials. When attached to biological targeting ligands, nanoparticles have the potential to bind to cellular structures, making them good candidates for medical diagnostics and therapy [42].

In particular, quantum dots are an exciting class of semiconductor nanoparticles that exhibit the special property of intense fluorescence. Quantum dots have already found widespread utility in several applications including solar energy conversion [43, 44], light emitting diodes [45], and quantum computing [46]. In this chapter, we will discuss how the intense fluorescence of QDs can be channeled as a useful tool for biomedical imaging. We will describe several methods of attaching biological targeting

ligands to QDs for developing novel biological imaging probes. Finally, we will focus on the specific application of these probes in the biological imaging of cellular proteins in living cells.

2.2 Properties of Quantum Dots

Physical Characteristics of Quantum Dots

Quantum dots are fluorescent semiconductor nanocrystals that exhibit special optical and electronic properties due to the "quantum confinement effect". They are commonly composed of II-VI (e.g. CdS, CdSe, CdTe), III-V (e.g. InAs, InP), or IV-VI (e.g. PbSe, PbS) semiconductor materials [14]. Figure 2.1 illustrates the difference between semiconductor quantum dots and bulk semiconductors. As shown in the left side of Figure 2.1, bulk semiconductors are characterized by a valence band (blue) and a conduction band (white) separated by a characteristic energy bandgap. When a bulk semiconductor is excited by a photon, an electron leaves the valence band and enters the conduction band, leaving behind a positively charged hole in the valence band. The electron and hole form a pair called an exciton, and the physical distance of separation between them is known as the material's exciton Bohr radius. For bulk semiconductors, the exciton Bohr radius is typically ~2 to 20 nm, much smaller than the size of the material. At any point in time, the electron may relax and recombine with the hole in the valence band to emit a photon with energy equal to the bandgap energy.

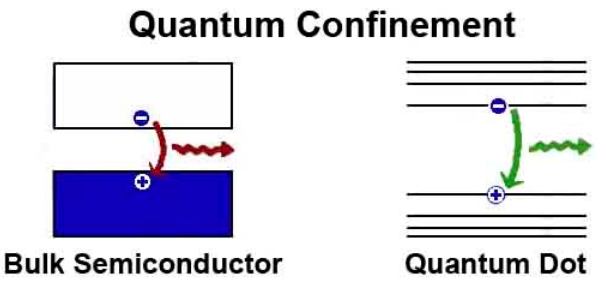

Figure 2.1. Quantum confinement effect of semiconductors. Quantum confinement of semiconductors produces quantum dots with discretized energy levels and larger bandgaps.

When a semiconductor material becomes confined in size in three dimensions such that its size is smaller than its characteristic exciton Bohr radius, its bandgap energy increases and its energy levels become discretized (Figure 2.1 right). As a result, the nanoparticle's wavelength becomes highly dependent upon its size. The greater the degree of confinement and the smaller the nanocrystal is in size, the higher its bandgap energy becomes. Since energy is inversely proportional to wavelength, smaller quantum dots emit at shorter wavelengths while larger quantum dots emit at longer wavelengths. As such, the color of the QD can be modulated by size and material composition to produce nanoparticles with fluorescence emission spanning the ultraviolent, entire visible light, and near-infrared ranges. Figure 2.2 a and b depict the emission wavelengths corresponding to some typical sizes of cadmium selenide (CdSe) quantum dots.

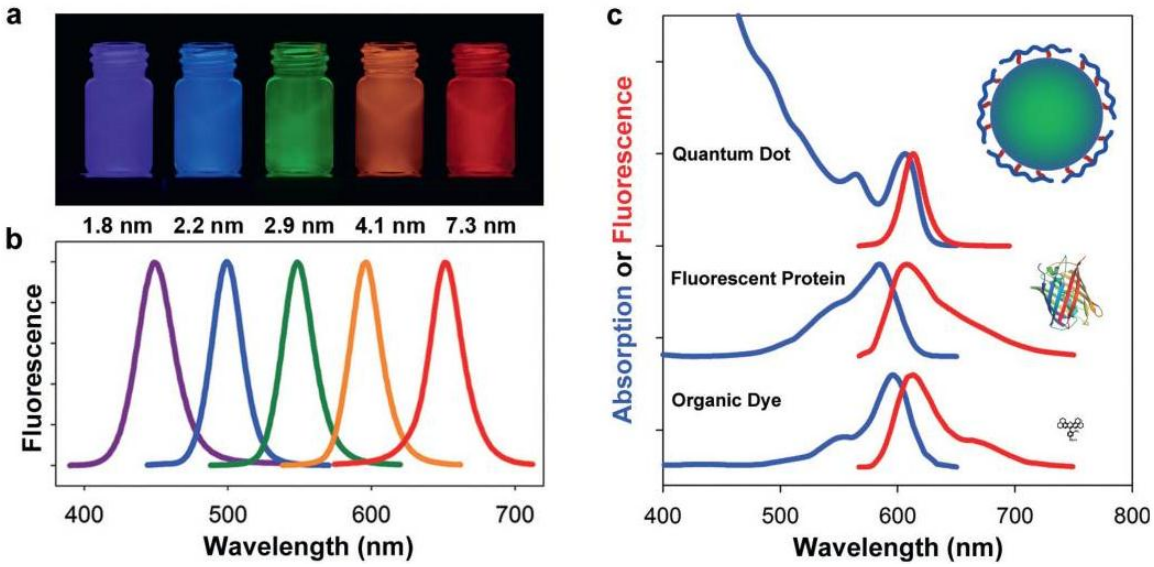

Figure 2.2. Quantum dot optical properties. (a) Six different sizes of cadmium selenide QDs under UV illumination and (b), their corresponding fluorescence emission spectra. (c) Absorption (blue) and emission (red) spectra of QDs compared with traditional fluorochromes, along with their relative sizes. Reprinted from [3].

Comparison of Quantum Dots with Fluorescent Dyes

QDs have several desirable properties that make them exceptional candidates for single-molecule imaging compared to traditional organic fluorophores. Due to their large absorption cross sectional areas, QDs exhibit intrinsically high signal brightness. With molar extinction coefficients commonly ranging between .5 - 5 x 10^6 M^{-1} cm^{-1}, they are on average 10-100x brighter than fluorescent dyes and proteins. The long fluorescence lifetimes (20-50 ns) of QDs are also advantageous, as well as their excellent resistance toward photobleaching [3, 13-15, 47]. In contrast with fluorescent dyes, which bleach almost immediately upon exposure to light, QDs are able to maintain constant fluorescence intensity for hours under UV illumination [11, 48].

As depicted in Figure 2.2c, all QDs possess broad absorption bands and narrow symmetric emission bands. One important consequence is that a single light source can be used to concurrently excite multiple QDs with different emission wavelengths, facilitating the simultaneous detection of several biomarkers in multiplexed assays and multi-color tracking experiments [21, 49]. In contrast, multiplexing is difficult to achieve with fluorescent dyes and proteins due to their relatively narrow, specific absorption bands. Nonetheless, QDs do have their disadvantages. Figure 2.2c shows that QDs (typically 10-40 nm) are an order of magnitude larger than organic dyes (typically < 1 nm) and fluorescent proteins (typically ~5 nm), such that steric effects and nonspecific interactions must be taken into consideration when evaluating probe performance [3].

As detailed in the next section, the large size of QDs partially stems from limitations in traditional QD synthesis and coating strategies, and can be further exacerbated by the choice of bioconjugation strategy. In the meantime, our lab and others have devoted much research to developing improved synthetic techniques for producing QDs with smaller nanocrystalline cores and organic surface coatings, along with reduced nonspecific effects [50-55].

2.3 Quantum Dot Probe Development

Quantum Dot Synthesis

Quantum dots were first synthesized by Alexander Ekimov and Alexei Efros in 1982 by growing nanocrystals in glass matrices [56, 57]. Since then, a wide variety of approaches have been developed to synthesize QDs in organic solvents, aqueous solutions, and on solid substrates. QDs have been fabricated using “top-down”

approaches such as lithography [58], and “bottom-up” approaches such as chemical vapor deposition [59] and molecular beam epitaxy [60, 61].

The most common procedure for producing high quality QDs is to synthesize colloidal suspensions of QDs using semiconductor precursors and organic surfactants. The fundamental procedure for colloidal QD synthesis was established in 1993, when Bawendi and coworkers developed a method for creating extremely monodisperse QDs composed of cadmium sulfide (CdS), cadmium selenide (CdSe), and cadmium telluride (CdTe) [62]. In a typical synthesis of CdSe QDs, a room-temperature Se precursor is quickly injected into a hot solution containing a Cd precursor and an organic surfactant under inert atmosphere. Organic surfactants commonly employed in this synthesis include alkyl phosphines, alkyl phosphine oxides, or alkylamines (e.g. trioctylphosphine, trioctylphosphine, hexadecylamine). At high temperature around 300 ^{0}C, monomers of the semiconductor precursors react quickly and nucleate to form CdSe nanocrystals. The organic surfactant serves as a coordinating ligand that binds to the surface of the nanocrystal and controls its rate of growth. Once the desired nanocrystal size and wavelength is achieved, the entire solution is quickly cooled to room temperature to prevent further growth.

Although synthesis of the QD is completed at this point, many researchers will choose to cap the QD core with another “shell” layer to enhance the luminescence efficiency and photostability of the QD. Because nanocrystals contain a large surface area to volume ratio, a large number of atoms are exposed to the surface of the QD. Some molecular orbitals of the surface atoms are bonded to other atoms, while other orbitals remain either unbonded or weakly bonded with organic coordinating ligands. Because the

bond strength between the surface atom and the coordinating ligand is much weaker than the bond strength between atoms, ligand desorption can occur over time, creating unbonded orbitals. Since unbonded and incompletely bonded "dangling" orbitals can quench QD fluorescence, the additional growth of a semiconductor shell with a larger bandgap helps to provide electronic insulation to the atoms on the surface of the core.

Zinc sulfide (ZnS) is a popular choice for a shell material due to its enhanced resistance to oxidation and greater bond strength with coordinating ligands compared to cadmium. To cap a CdSe with ZnS, the CdSe are first purified from unreacted Cd and Se precursors. In a similar procedure as before, Zn and S precursors are injected into a solution containing CdSe QDs and organic coordinating ligands. This time however, the temperature is reduced to ~160 - 220 ^{0}C and the precursors are slowly added. These conditions help prevent nucleation of ZnS nanocrystals, and instead favor growth of the ZnS shell on the CdSe core.

Unfortunately, direct growth of the ZnS shell on the CdSe core produces high interfacial strain due to a large difference in lattice constants between the core and shell materials. This interfacial strain can result in the formation of defect sites, thereby decreasing the quantum efficiency of the QD. Several researchers have found that the high strain can be alleviated by including intermediate shell layers with successively changing lattice constants [63-65]. As a result, it is very common to find QDs with varied compositions such as CdSe(CdS/ZnS) or CdSe(ZnSe/ZnS).

In 2003, Peng and coworkers showed that high quality core/shell nanocrystals can be formed using "successive ion layer adsorption and reaction" (SILAR), a procedure that forms the fundamental basis of many QD capping protocols used today [66]. The

hallmark of this procedure is that alternating additions of shell precursors can be used to enhance the quality and homogeneity of shell formation. For example, to cap a CdSe core with a CdS/ZnS shell, the Cd precursor is first injected followed by a subsequent injection of S precursor to create a CdS monolayer. This process is repeated multiple times until the desired number of CdS monolayers is achieved and then repeated with alternating Zn and S precursor injections, all while gradually increasing the temperature from ~120 to 260 ^{0}C. Once the desired nanocrystal size is achieved, the reaction is quickly cooled to arrest further growth. Upon successful synthesis and purification of the QDs, they can be transferred to water using various surface coating strategies.

Quantum Dot Coating Strategies

Because QDs are generally synthesized in non-polar organic solvents using hydrophobic coordinating ligands, they must be rendered water-soluble to be useful for biological applications. To do this, one of two methods has traditionally been employed. In the first process known as "ligand exchange," coordinating ligands are displaced from the QD surface using small hydrophilic ligands that chelate the surface (Figure 2.3a). Thiolated ligands such as mercaptoacetic acid, mercaptopropionic acid or (3-mercaptopropyl) trimethoxysilane are frequently used since thiols can bind to Zn or Cd atoms on the QD surface. Amine-containing ligands such as cysteamine can also be used. This method produces very small QDs but provides little colloidal stability, causing decreased fluorescence efficiency and aggregation in biological buffers [67, 68]. Due to the poor stability of the ligands and limitations in the number of different functional groups available for bioconjugation, it is difficult to conjugate antibodies and other ligands to the surface of these QDs.

In the second water solubilization procedure, the coordinating ligands of the QD are encapsulated by an amphiphilic polymer (Figure 2.3b) [16, 17, 22]. Several different types of amphiphilic polymers have been developed for coating quantum dots, including low molecular weight polymers [22, 69] , block copolymers [70], and triblock copolymers [17]. This method generates QDs of much greater brightness and stability, at the expense of producing large QDs in the range of 20-40 nm hydrodynamic diameter [13]. Several different functional groups, including carboxylic acids, amines, and thiols can be easily incorporated into the amphiphilic polymer for subsequent bioconjugation reactions. Consequently, amphiphilic polymer coating is the preferred coating strategy for the majority of commercially available QDs in the market, including Invitrogen Qdots.

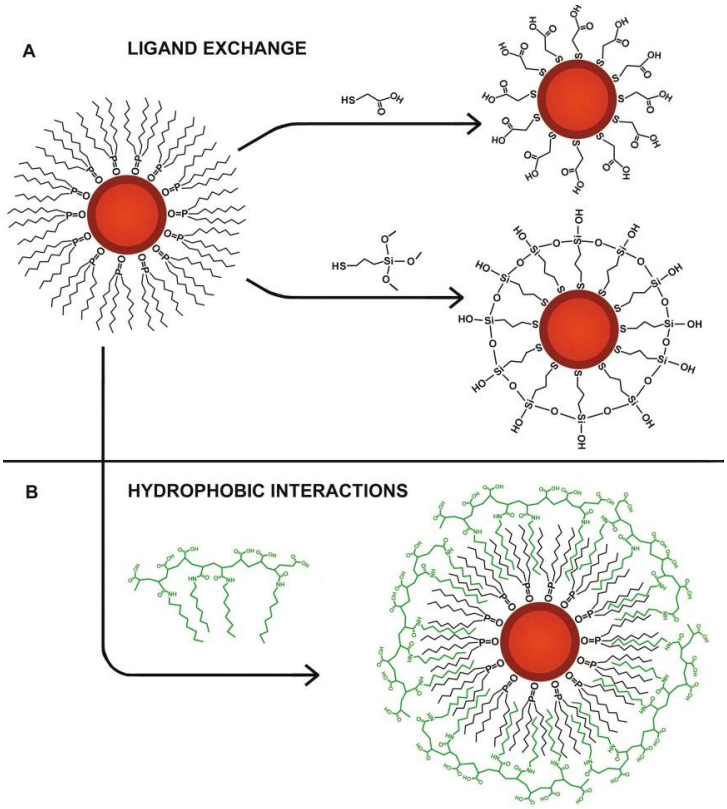

Figure 2.3. Common strategies for water solubilization of quantum dots. Quantum dots can be transferred to water using (a) ligand exchange or (b) amphiphilic polymer coating. Amphiphilic polymers interact with coordinating ligands on the QD surface through hydrophobic interactions. Reprinted from [71].

Quantum Dot Bioconjugation Strategies

To enable specific binding to a target, biomolecules can be attached to the QD surface using either covalent or noncovalent methods. In covalent conjugation, functional groups incorporated on the surface coating of the QD are reacted with specific chemical moieties on the targeting biomolecule. For example, one common method of covalent conjugation is to utilize the chemical crosslinking agent 1-ethyl-3-(3-dimethylaminopropyl)carbodiimide, known as EDC, to react carboxylic acids on the QD

surface with amine groups on peptides. Another method, often used to attach antibodies to QD surfaces, is to react malemide-activated quantum dots with reduced cysteines on the antibody [72].

While covalent conjugation methods are generally preferred for cellular tracking studies, noncovalent conjugation methods can be advantageous in many applications. If the surface coating of a QD is highly charged, electrostatic interactions with an oppositely charged molecule can be exploited to assemble a QD bioaffinity probe. Electrostatic attraction is often used to assemble negatively charged DNA or siRNA molecules with positively charged QDs [73]. As later discussed in Chapter 3, proteins containing specialized peptide sequences such as a histidine tag [74] or an oligoaspartate tag [75] can directly chelate the surface of the QD noncovalently in a high affinity manner.

Figure 2.4 illustrates some of the most typical bioconjugation strategies used in cellular studies. One extremely popular strategy is to use quantum dots covalently conjugated to streptavidin, a 60 kDa tetrameric protein that binds to the vitamin biotin with extremely high affinity ($K_D \sim 10^{-14}$ M) [76]. This strategy is incredibly versatile, as a wide variety of biotinylated antibodies and proteins can be purchased from commercial vendors along with ready-made QD-streptavidin conjugates. Cell surface proteins can also be easily biotinylated using commercial kits and tracked using streptavidin-QDs. The greatest advantage of streptavidin-biotin conjugation is the ease of producing conjugates at near covalent affinity; nonetheless a few disadvantages do exist. Because biotin is a molecule native to cells, nonspecific binding of streptavidin-QDs to endogenous biotin can sometimes be problematic. Additionally, since each streptavidin contains four

binding sites for biotin, multivalent binding and crosslinking of biotinylated receptors can occur when tracking cellular proteins.

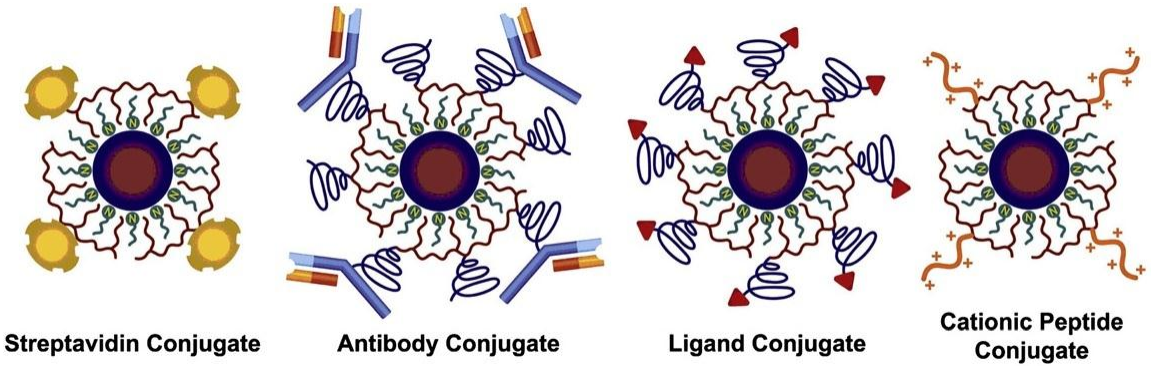

Figure 2.4. Common bioconjugation strategies for quantum dots. Figure adapted from [13].

Since antibodies can be raised with high specificity for a wide variety of antigens, quantum dot-antibody conjugates have become one of the most commonly used QD probes in biological applications. Antibodies can be biotinylated and conjugated to QDs via streptavidin, or they can be directly conjugated to the QD surface. Nevertheless, antibodies also have several limitations. At 150 kDa, antibodies are large with hydrodynamic diameters exceeding 10 nm [77], adding considerable bulk to the QD probe. Antibodies are divalent and bind to their targets with relatively low affinity (K_D~10^{-6} to 10^{-9} M), causing potential problems with crosslinking receptors and receptor dissociation during cellular tracking. Furthermore, since direct QD conjugation can sometimes alter the binding properties of the antibody, a two-layer strategy is often implemented for labeling targets, with a primary antibody used in addition to a QD-secondary antibody conjugate. When this two-layer strategy is implemented, the total QD

complex can be extremely large, reaching up to 50 nm in hydrodynamic diameter [34]. As further discussed in Chapter 3, the large size of this QD complex can adversely affect receptor tracking in several different parts of the cell.

Due to limitations with antibodies, an alternative strategy is to conjugate small ligands that bind to the desired target receptor with high specificity. These ligands include small molecules (e.g. RGD, folate), proteins and peptides. In particular, special cationic peptides, such as the HIV Tat peptide and the nuclear localization sequence (NLS) peptide, can serve as signaling sequences that help transport QDs to particular locations inside the cell [30, 31].

2.4 Quantum Dots in Live Cell Imaging

Indeed, several of these bioconjugation strategies have already been successfully implemented in live cell imaging studies. The vast majority of these studies have utilized QD probes to study the receptor dynamics and endocytosis of cell membrane proteins. In 2003, Maxime Dahan and coworkers published the first paper utilizing QDs to track single receptors in live cells. Using commercial streptavidin-QDs coupled to biotinylated secondary antibody fragments along with a primary antibody, they were able to specifically detect glycine receptors on the surface of cultured spinal neurons. Because single quantum dots exhibit a hallmark “blinking” characteristic in which emitted fluorescence turns on and off intermittently [78], the authors could identify and track single receptors at high resolution. Glycine receptors could be seen alternating between free diffusion in the extrasynaptic space and confined diffusion in the synaptic domain. With QD technology, the movements of individual glycine receptors could be visualized in unprecedented detail, shedding insight into their fundamental dynamics [23].

In 2004, Lidke et al. published the first paper utilizing QDs to visualize receptor signalizing transduction in live cells. They used streptavidin-QDs coupled to biotinylated epidermal growth factor (EGF) to image signal transduction of the classical cell surface EGF receptor, erbB1. They showed that binding of QD-EGF rapidly induced endocytosis of the EGF-QD-erbB1 complex via clathrin coated pits into endosomes. They were able to visualize internalized vesicles containing the EGF-QD-erbB1 complexes undergoing Brownian motion, vesicular fusion, and linear motion directed by microtubule motor proteins. Interestingly, the authors observed a novel process whereby EGF-QD-erbB1 complexes uptaken by cell filopodia were transported in retrograde motion to cell body. This previously unreported mechanism was discovered due to the high resolution single-molecule imaging made possible by QD technology [24]. The authors subsequently extended their study to investigating EGF receptor interactions by simultaneously using two colors of QDs to image EGF receptor dimerization [79].

Since these two early studies, new breakthroughs in understanding membrane receptor dynamics continue to be made with QDs in practically every area of biology. QDs have been used to track numerous membrane receptors and membrane channels, including receptor tyrosine kinases [26, 27], G protein coupled receptors [25], integrins [28, 29], ion channels [80, 81], and aquaporins [82, 83]. In neurobiology, QDs have been used to study a wide variety of neuroreceptors in addition to glycine receptors, including AMPA [84, 85], GABA [86], NMDA [87], and acetylcholine receptors [88].

QD tracking studies performed with intracellular receptors have been much more limited in scope and number. As explained in the next chapter, direct targeting of QDs to intracellular proteins in the cytosol remains a significant bottleneck to progress in

intracellular imaging. Nonetheless, a few advances have been made in this area. QDs have been successfully delivered into the cell cytoplasm using a variety of chemical and mechanical methods, including microinjection, electroporation, chemical transfection, and pinocytic loading [30, 89, 90]. In 2006, Courty and coworkers reported the first study incorporating QDs for intracellular protein tracking. In this study, the authors pre-assembled streptavidin-QDs with biotinylated kinesin motor proteins and delivered the resulting conjugates into cells using pinocytic loading [89]. Inside cells, these QD-kinesin conjugates were shown to migrate processively on microtubules with a velocity and processivity similar to the motion of kinesins observed on purified microtubules *in vitro.* In a similar follow-up study performed with streptavidin-QDs and biotinylated myosin proteins, QD-myosin complexes could be seen processing on actin filaments in a hand-over-hand manner [90].

These studies demonstrate the breadth of versatility and the wealth of information that can be gained from single QD tracking. Nonetheless, they also reveal some significant challenges. Large multi-layer QD antibody conjugates have limited access to crowded locations such as neural synapses, which are typically only about 20 nm wide, and thus are unideal for imaging synaptic receptors [3, 91]. When using QDs to study receptor interactions, the large size of the QD labels may potentially hinder dimerization and other interactions. Furthermore, many challenges remain in the field of intracellular tracking. Delivery of freely diffusing QDs into the cytosol still remains difficult in many cases [92]. Importantly, QD probes that remain unbound to their target cannot be freely washed out from the cytosol. Consequently, direct quantum dot targeting of cytosolic proteins is difficult to achieve, and most studies have been performed by first assembling

QDs with a purified form of the protein of interest *ex vivo* prior to cytosolic delivery. These challenges have formed the incentive for the design of new and improved QD probes for the next generation of cellular tracking studies.

2.5 Challenges and Opportunities

Current-Generation Quantum Dots

In spite of major successes with QDs in live cell imaging applications, traditional QDs have several disadvantages, and several opportunities exist for improving the design of QDs. The bioconjugation strategies depicted in Figure 2.4 represent idealized schematics—in reality, the bioconjugation process is difficult to control and yields highly variable results.

Figure 2.5a shows a schematic of a standard commercial quantum dot with the traditional method of attaching protein targeting ligands to the surface. Slightly elongated in shape, commercial QDs are generally 15-35 nm in hydrodynamic diameter prior to modification with targeting ligands. During chemical conjugation, functional groups displayed on the polymer surface are reacted with random amines or thiols on the protein. Because the process is random, the resulting number of targeting ligands on the QD is random, resulting in a population of polydisperse, multivalent probes. The orientation of the ligands is likewise random, causing several of the protein active sites to be obstructed from binding their target.

Large QDs exhibit increased binding steric hindrance and limited mobility compared to smaller probes. Due to their large surface area to volume ratio, large particles also display an increased propensity for nonspecific binding. The attachment of targeting ligands only serves to exacerbate the size of the existing QD, further reducing

its mobility in cellular environments. Large numbers of surface ligands can also increase nonspecific binding while causing unwanted crosslinking of receptors during cellular imaging.

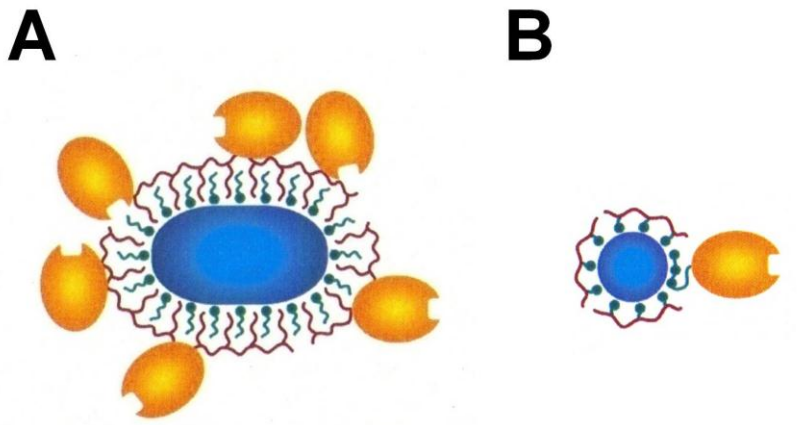

Figure 2.5. Comparison of traditional commercial quantum dot probes and the next generation of improved quantum dot probes. (a) Traditional amphiphilic polymer-coated QDs conjugated to targeting ligands using stochastic chemical conjugation methods are large and multivalent. (b) Next-generation quantum dot probes should ideally be small and monovalent. Figure adapted from [12].

Next-Generation Quantum Dots

Several laboratories including our own are currently working towards reducing the size of QDs and improving their targeting strategies [51, 53, 93-96]. Figure 2.5b depicts a schematic of an ideal QD probe with improved binding characteristics. Ideally, these QD probes would have overall sizes comparable to globular proteins, which are generally 5 to 15 nm in hydrodynamic diameter. These QD probes would be monovalent with functional active sites directed outward. Not only would monovalent probes prevent unwanted receptor crosslinking and cell signaling, but limiting the number of targeting

ligands would also help to reduce the total size of the QD probe. The overarching goal in developing the next generation of QDs is to produce probes that are able to diffuse freely under a wide variety of cellular conditions, exhibiting reduced binding steric hindrance and enhanced resistance to nonspecific binding.

2.6 Conclusions

In recent years, quantum dots have garnered intense interest as biological imaging probes due to their intense and stable fluorescence. Since the first reports by Paul Alivisatos and Shuming Nie demonstrating utility of QDs in biological research in 1998, quantum dots have found widespread application in small animal imaging, disease biomarker detection, and cellular imaging [97, 98]. In the field of cellular imaging, the emergence of QD technology has allowed researchers to visualize receptor dynamics and protein interactions in an unprecedented detail previously not achievable with fluorescent dyes. Opportunities now exist for improving the design of QDs to enhance their applicability in a broader range of cellular conditions. This work will focus on reducing the overall size of QDs and their attached targeting ligands so that QDs can gain access to crowded locations such as neural synapses and the cellular cytosol. We will investigate new strategies for attaching targeting ligands to QDs with improved binding properties to their cellular proteins of interest. The results of our studies will help guide the design of next-generation nanoparticle-based imaging agents, paving the way for new scientific breakthroughs in understanding cellular and biomolecular interactions.

CHAPTER 3

SIZE-MINIMIZED QUANTUM DOTS AND TAGGING STRATEGIES

3.1 Introduction

The size of nanoparticles has been shown to be an important parameter in many biological applications [99]. Nanoparticle size has been shown to have broad-ranging effects both on the cellular level, affecting cellular uptake [100, 101] and cellular toxicity [102], and on the whole-organism level, affecting nanoparticle biodistribution and clearance [77, 103, 104]. In several areas, small nanoparticles have been shown to exhibit several desirable advantages over their larger counterparts. For instance, in *in vivo* imaging applications, nanoparticles less than 6 nm have been shown to extravasate more uniformly into tumor tissue [104] and are cleared more rapidly from the body [77].

The size of nanoparticles is likewise critical in live cell imaging. As discussed in Chapter 2, quantum dots have emerged as an incredibly promising tool for live cell imaging, especially single-molecule imaging. Nonetheless, the large size of conventional quantum dots has precluded their widespread use in imaging crowded cellular locations such as extracellular synapses, intracellular compartments, and organelles.

In this chapter we summarize the effects of nanoparticle size on the cellular diffusion and nonspecific binding, focusing on the advantages of size-minimization. We discuss current research strategies to reduce the size of quantum dots and their targeting ligands. Finally, we present our own research strategy in choosing a size-minimized

quantum dot and tagging strategy for designing a novel optical imaging probe for cellular imaging.

3.2 Size Effect on Quantum Dot Imaging of Various Cellular Compartments

Size Effect on Intracellular Diffusion of Quantum Dots

The cell cytoplasm is a crowded compartment comprised of a network of actin, myosin, and intermediate filaments densely packed with proteins and macromolecules [105, 106]. The classic drawing by David Goodsell shown in Figure 3.1 depicts a view of the crowded cellular interior, drawn to scale with all cytosolic components shown at physiologically accurate concentrations. The protein concentration in the cytoplasm of mammalian cells is extremely high, estimated to be 200-300 mg/ml, and can reach up to 35% of the cell's total weight [107]. At this concentration, transport of macromolecules in cellular interiors is significantly affected by intermolecular interactions. Consequently, physical properties such as size, geometry, and surface chemistry all play important roles in macromolecular diffusion.

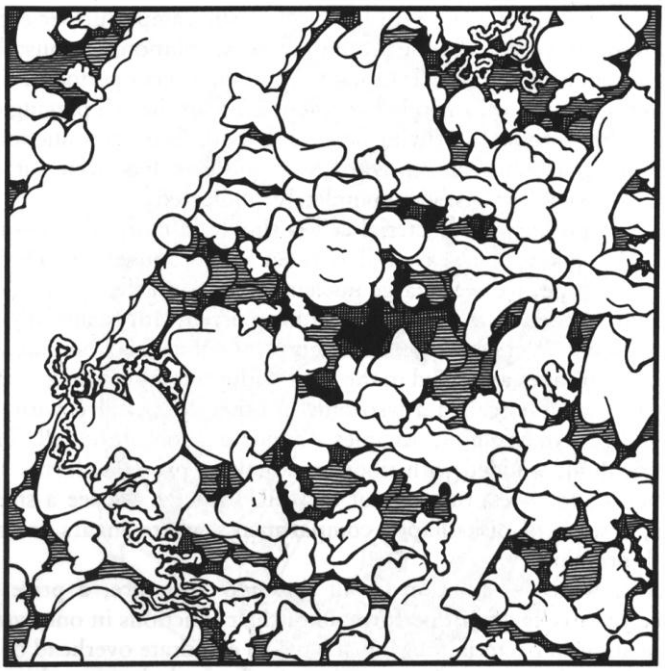

Figure 3.1. An illustration depicting the crowded cytoplasm of yeast, *S. cerevisiae*. All components are drawn accurately to scale and at the correct concentrations. Reprinted from [108].

Several previous studies have characterized the role of size on the diffusion of macromolecules within the cytoplasm [109-112]. For example, Verkman and coworkers measured the effect of molecular weight on the diffusion of FITC-labeled polysaccharides in cytoplasm using fluorescence recovery after photobleaching (FRAP). As shown in Figure 3.2, dextrans smaller than 500 kDa were found to diffuse freely inside the cytoplasm at approximately a 4.5-fold slower rate than their diffusion in water. Dextrans larger than 1000 kDa (~15 nm hydrodynamic diameter) started to exhibit impaired mobility, while 2000 kDa dextrans (~30 nm hydrodynamic diameter) were almost immobile [106].

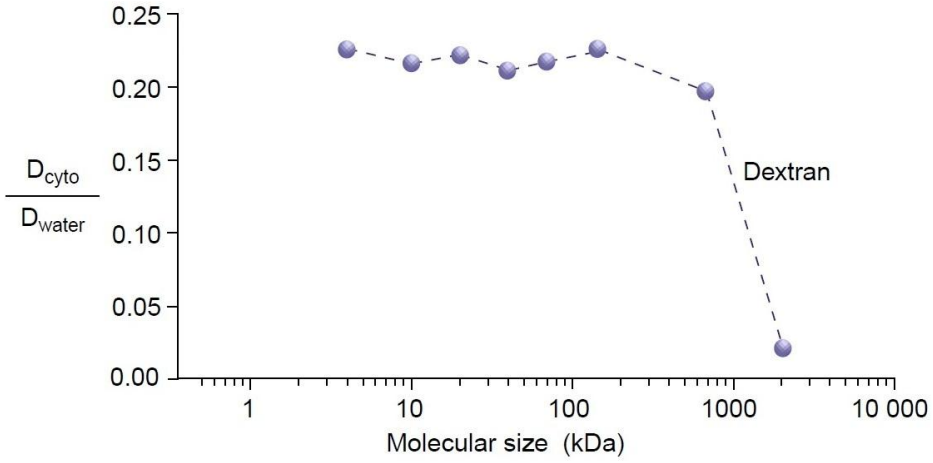

Figure 3.2. Effect of molecular size on the diffusion of FITC-labeled dextrans in cytoplasm as compared to their diffusion in water. The ratio of the dextran's diffusion coefficient in cytoplasm (D_{cyto}) to its diffusion coefficient in water (D_{water}) is plotted as a function of the dextran's molecular weight. Adapted from [106].

Our laboratory has studied the effect of size on the cytoplasmic diffusion of quantum dots and found the results to be consistent with the data obtained for diffusion of dextrans. In this study, multidentate polymer coated quantum dots of three different sizes were loaded into the cytoplasm of A431 cells using a technique called pinocytic loading [113]. As shown in Figure 3.3, large QDs with 40 nm and 28 nm hydrodynamic diameters both exhibited strongly limited mobility in the cell interior. Only the 10 nm QDs were observed to exhibit free Brownian diffusion.

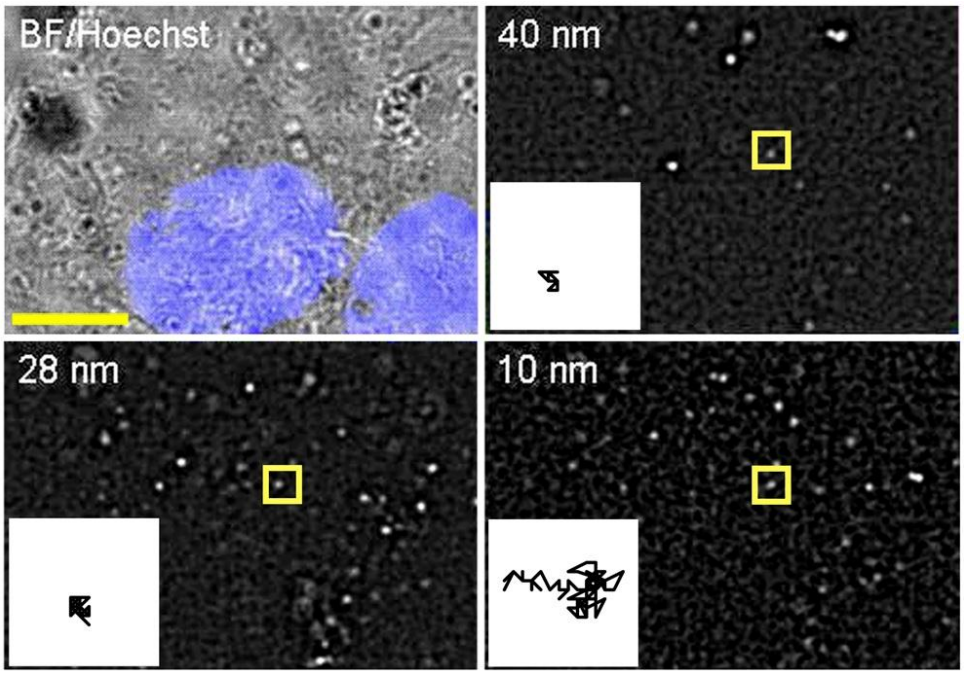

Figure 3.3. Effect of nanoparticle size on the diffusion of QDs in cytoplasm. Representative trajectories are shown for QDs of three different sizes, 10 nm, 28 nm, and 40 nm that have been loaded into the cytoplasm of A431 cells using pinocytic loading. Reprinted from [3].

In summary, studies have shown that small particles are able to diffuse freely in cytoplasm, while the diffusion of large particles can be greatly impaired. For both QDs and dextrans, the size cutoff for free diffusion has been observed to be about 15-20 nm, although this size cutoff may naturally vary for different macromolecules with different surface properties.

Size Effect on Cellular Surface Diffusion of Quantum Dots

While nanoparticle size has a great effect on diffusion in confined environments such as the cell interior, it has little effect on diffusion in unconfined regions of the cell

surface. In general, tracking of cell surface receptors is not affected by the size of nano-sized probes. Because the viscosity of the cell membrane is 100- to 1000-fold greater than the viscosity of the extracellular medium, nanoparticles exhibit very little drag force on the surrounding medium. Consequently, the viscosity of the cellular membrane is the limiting factor governing cell surface receptor diffusion in unconfined environments.

In contrast, the size and valence of nanoparticle probes do exhibit significant effects on receptor movement in confined regions of the cell surface such as neural synapses [84]. The width of the synaptic cleft is only an average of ~20 nm [91]. As a result, commercial QDs, which typically range from 15 to 35 nm in hydrodynamic diameter, often exhibit difficulty accessing the synaptic cleft. In 2007, Groc et al. compared the labeling of glutamate receptors in the synaptic clefts of hippocampal neurons using commercial QD-antibody, dye-antibody, and dye-ligand complexes. They discovered that the smaller probes were able to penetrate the synaptic clefts more easily, with the number of dye-ligand complexes inside the synaptic cleft found to be four times greater than the number of QD-antibody complexes. They further discovered that the small dye-ligand probes were able to detect populations of fast diffusing synaptic receptors better than the larger QD-antibody probes [84]. In conclusion, the results of this study suggest that the development of smaller probes could allow researchers to obtain more accurate information about receptor movements in confined environments.

Size Effect on Quantum Dot Transport into Cell Nucleus

Interestingly, several groups have observed an effect of nanoparticle size on the translocation of QDs from the cytoplasm into the nucleus [32, 114-116]. In a study reported in 2005, Lovric and coworkers prepared green cysteamine-coated CdTe QDs

with 2.2 nm hydrodynamic diameter and red cysteamine-coated CdTe QDs with 5.5 hydrodynamic diameter. When these QDs were passively loaded into murine microglial cells, the green QDs were found to spontaneously translocate into the nuclei of cells while the red QDs remained only in the cytoplasm. The authors found that entry of the green QDs into the nuclei could be abolished if the green QDs were coated with albumin, suggesting that an increase in overall nanoparticle size could block entry into the nucleus [114]. Nabiev et al. later confirmed this size effect in a similar study with human macrophages, reporting a size-cutoff of approximately 3 nm for QD entry into the nucleus. The researchers further determined that the mechanism for nuclear transport of small QDs occurs via active transport on microtubules, and not passive diffusion [32].

The nuclear pore typically allows passage of macromolecules up to 9 nm in diameter [117]. Therefore, it is interesting that the apparent size-cutoff for nanoparticle entry appears to be much smaller. Since nanoparticles coated with small ligand coatings like cysteamine exhibit poor colloidal stability in biological buffers, it is possible that particle aggregation may account for an increase in size. It is also possible that absorption of proteins onto the nanoparticle surface may increase the effective size of the red QDs, precluding their entry into nuclear pores. As discussed in the next section, the size of a nanoparticle can influence its propensity to nonspecifically adsorb to proteins.

3.3 Size Effect on Nonspecific Binding of Quantum Dots

In addition to enhancing nanoparticle access to confined regions of the cell, another compelling reason for moving towards size-minimized nanoparticles is that small colloids are inherently more resistant to nonspecific binding than larger ones. Smaller colloids diffuse faster than larger colloids as shown by the Stokes-Einstein equation,

$$D = \frac{kT}{6\pi\eta r}$$ Equation 3.1

where r is the radius of the colloid, η is the viscosity of the solvent, T is the temperature, and k equals the Boltzmann's constant. The high diffusivity of small colloids renders them less capable of forming bonds with other molecules while concomitantly helping to disrupt weak intermolecular interactions. As a result, small colloids are less likely to form nonspecific interactions than larger colloids.

The high degree of surface curvature inherent to small colloids also helps to prevent nonspecific binding. As shown in Figure 3.4, large colloids have a flatter surface, thereby increasing the effective surface area capable of forming multivalent interactions. On the other hand, small colloids are less capable of forming multivalent interactions with other surfaces.

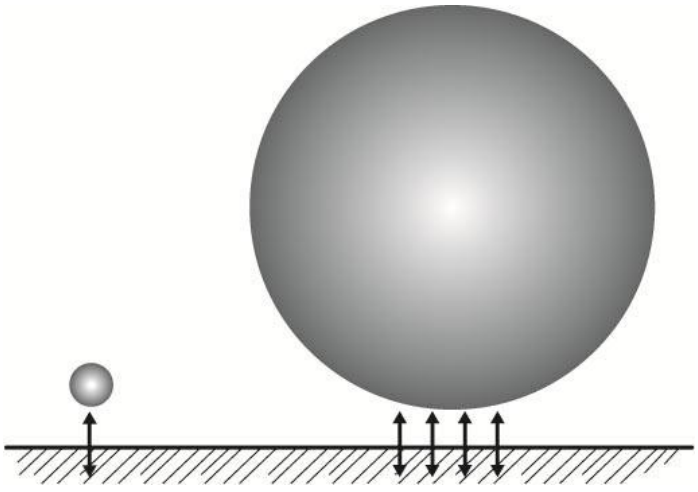

Figure 3.4. Effect of nanoparticle surface curvature on multivalent binding interactions. Small nanoparticles have a higher degree of surface curvature and are less likely to form multivalent interactions than larger nanoparticles.

Previous work done in our laboratory has provided evidence to support the theory that small nanoparticles are inherently resistant to nonspecific binding. In particular, small quantum dots less than ~6 nm in hydrodynamic diameter were observed to exhibit a dramatically enhanced resistance towards nonspecific binding to serum proteins compared to larger quantum dots. In this study, CdTe QDs with 3 nm cores and 5 nm cores were fully coated with thioglycerol to achieve particles with final hydrodynamic diameters of 4 nm and 6 nm respectively. The thioglycerol coated QDs were incubated in either phosphate buffered saline (PBS), 50% fetal bovine serum (FBS), or 3% bovine serum albumin (BSA) at 37^0C for 1 hour. Samples were subsequently resolved in a 0.7% agarose gel and visualized under ultraviolet illumination. As shown in Figure 3.5, 6 nm QDs exhibited great changes in electrophoretic mobility when incubated in serum and albumin, indicating that nonspecific binding between QDs and serum proteins has occurred. In contrast, 4 nm QDs exhibited little change in electrophoretic mobility when incubated in these protein solutions [118].

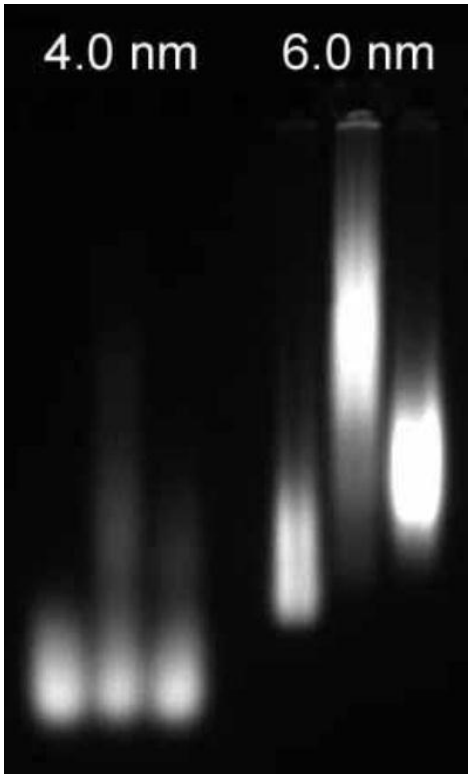

Figure 3.5. Nonspecific binding of quantum dots of different sizes to serum and albumin. QDs with 4 nm and 6 nm hydrodynamic diameters were incubated in PBS (left lane), 50% FBS (middle lane), or 3% BSA (right lane) at 37^0C for 1 hour and resolved using agarose gel electrophoresis. Reprinted from [118].

We also observed the same property of resistance towards nonspecific binding for other types of small nanoparticles. In a study performed with gold nanoparticles, three sizes of gold nanoparticles (Ted Pella)—2 nm, 5 nm, and 10 nm—were fully coated with methoxy-PEG-thiol (356.48 Da, Quanta Biodesign) to achieve particles with final hydrodynamic diameters of 5 nm, 9 nm, and 13 nm respectively. Pegylated gold nanoparticles were incubated in either PBS or 50% FBS at 37^0C for 1 hour. Samples were subsequently resolved on a 1% agarose gel and visualized using silver enhancement (LI Silver Enhancement Kit, Nanoprobes). Out of the three different sizes of gold shown in

Figure 3.6, only the smallest gold nanoparticles with a final hydrodynamic diameter of 5 nm exhibited resistance to nonspecific binding when added to serum.

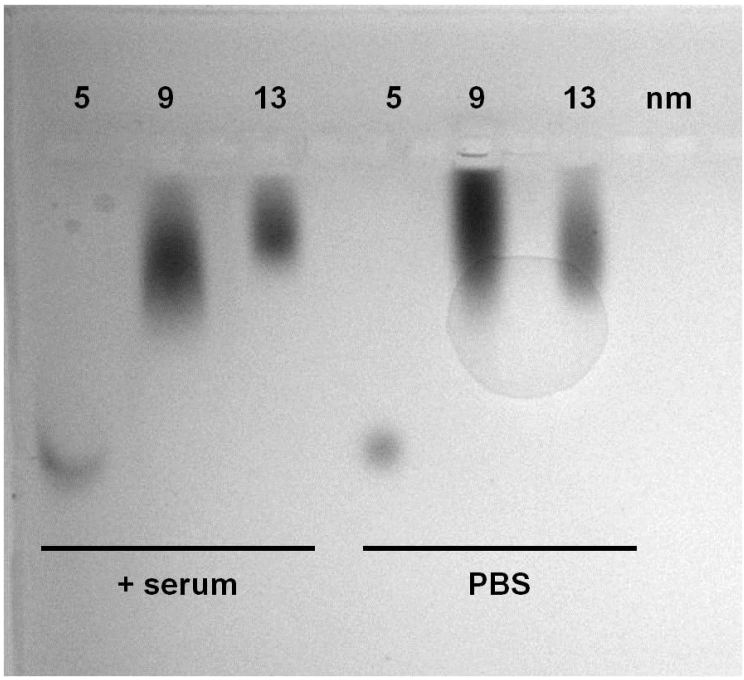

Figure 3.6. Nonspecific binding of gold nanoparticles of different sizes to fetal bovine serum. Three sizes of gold nanoparticles with final hydrodynamic diameters of 5, 9, and 13 nm were incubated in either PBS or 50% fetal bovine serum at 37^0C for 1 hour and resolved using agarose gel electrophoresis.

Due to the advantages of size-minimized nanoparticles in reducing nonspecific binding and enhancing cellular diffusion, the development of new strategies to minimize the size of QD probes has become an active area of research. Although ultra-small QDs (<6 nm diameter) have already been incorporated in some of the studies mentioned above, virtually all of these studies have implemented uncapped CdTe QDs containing small ligand coatings such as cysteamine and thioglycerol. “Core-only” QDs such as CdTe are typically smaller than their core-shell counterparts but exhibit much lower

photostability. Small-ligand coatings easily desorb from the QD surface in complex biological fluids, offering little colloidal stability to the underlying QD [67, 68]. Thus, an express need remains for engineering new types of small QDs with high photostability and colloidal stability. So far, many of the advances in producing size-minimized QDs have been driven by an effort to improve the stability of thin coatings. These efforts are summarized in the next section.

3.4 Size-Minimized Quantum Dots

As discussed in Chapter 2, QDs are often synthesized in organic solvents using hydrophobic coordinating ligands to control their growth rate. As a result, QDs must be phase transferred to water prior to use with biological systems. The most common method of water solubilization is to encapsulate the QD's coordinating ligands with an amphiphilic polymer (Figure 3.7a). This strategy is used to coat the majority of commercially available QDs, including the widely popular Invitrogen Qdots. Coating with amphiphilic polymer generates QDs with excellent brightness and stability at the expense of producing large QDs in the range of 20-40 nm hydrodynamic diameter [13, 15].

Since decreased stability and increased nonspecific interactions often accompany a reduction in the thickness of the surface coating, reducing QD size remains a considerable challenge. Early generations of QDs with thin coatings often incorporated small monodentate ligands such as mercaptoacetic acid and mercaptopropionic acid that could chelate atoms on the QD surface. These hydrophilic ligands were used to displace the hydrophobic coordinating ligands from the QD surface to produce extremely compact QDs. Unfortunately, due to the weak interaction of monodentate ligands with QD surface

atoms, desorption of these ligands from the QD surface could occur in less than 24 hours [67, 119].

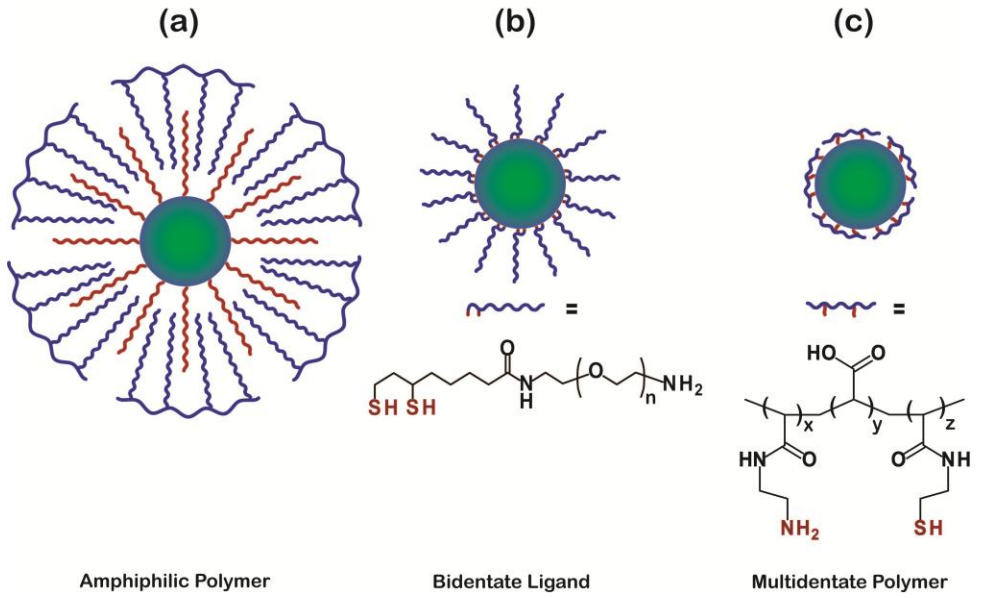

Figure 3.7. Traditional versus new compact QD coatings. (a) Schematic diagram of a traditional amphiphilic polymer coated QD. Novel compact coatings include (b) bidentate ligands such as dihydrolipoic acid-PEG ligands developed by Mattoussi and Bawendi, along with (c) multidentate polymer coatings developed by Nie et al. Adapted from [3].

As such, recent advances have focused on increasing the binding affinity of these hydrophilic ligands to the QD surface through multidentate interactions. The Mattoussi and Bawendi groups have developed a bidentate ligand coating based on dihydrolipoic acid grafted to a short linear PEG chain. This DHLA-PEG coating (Figure 3.7b) is anchored to the QD via coordination of dithiols in a brush-like monolayer [53, 55]. Quantum dots coated with DHLA-PEG have already been successfully implemented in several live-cell imaging studies [10, 53]. Nonetheless, oxidation and dimerization of the

thiol groups can cause the bidentate ligands to become unstable over time, and the effects of this instability have been reported in as little as 1 week [54].

We have observed that the long-term colloidal stability and photostability of the QD can be enhanced by further increasing the number of binding motifs in the polymer coating. Our laboratory has developed a multidentate polymer coating based on a polyacrylic acid backbone modified with thiols and amines that chelate the QD surface in a flat-wrapping conformation [50, 51] (Figure 3.7c). Because this conformation is very stable thermodynamically, these multidentate polymer coated QDs exhibit excellent optical properties and maintain their stability for several months, even years. Similarly, the Bawendi group has developed a polymer coating that binds to the QD surface through multiple imidazole groups in a multidentate fashion [54]. The development of these new multidentate surface coatings enables QD size reduction without compromising QD stability—a remarkable achievement that will prove to be beneficial in many biological imaging applications.

3.5 Size-Minimized Tagging Strategies

The size of the QD is of paramount importance in reducing steric hindrance and ensuring adequate diffusivity in cellular compartments. Equally as crucial is the "tagging strategy", the method by which the QD recognizes or is attached to its target biomolecule of interest. Ideally, QD-probes should bind their targets with high affinity and be monovalent to avoid crosslinking receptors. Size and tagging are intricately related, as monovalent probes would be smaller and able to diffuse faster than their multivalent counterparts.

As shown in Figure 3.8a, the most popular conventional approach to QD targeting involves the use of antibodies. At 150 kDa, the antibodies used to target QDs to cell surface proteins are large, divalent, and bind with relatively low affinity (K_D~10^{-6} to 10^{-9} M) [35]. Due to the large QD surface area available for coupling, multiple antibodies are usually bound to the surface, resulting in a total construct that can reach up to 50 nm in size [34, 120].

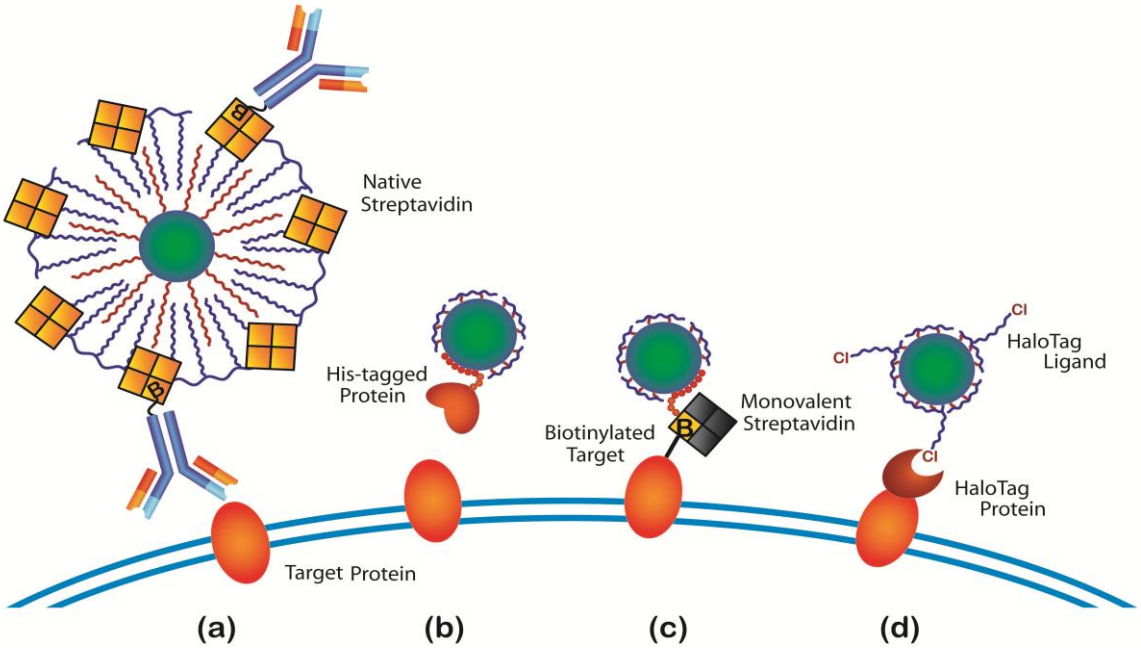

Figure 3.8. Traditional versus new tagging strategies. (a) A popular traditional tagging strategy involves coupling of biotinylated antibodies to commercially available streptavidin-coated QDs. New size-minimized tagging strategies include: (b) His-tag chelation, (c) Monovalent streptavidin – biotin binding, and (d) HaloTagging. See text for details. Adapted from [3].

Recently, the emergence of new site-specific tagging strategies has eliminated the need for antibodies altogether. These techniques include a variety of affinity chelation, enzyme-mediated, and covalent labeling techniques. Figure 3.8 b – d highlights some of the most promising tagging strategies for quantum dots.

One such approach utilizes the polyhistidine tags ("his-tags") commonly introduced into recombinant protein sequences for Ni^{2+} -NTA purification to chelate QD surfaces containing Zn^{2+} or Cd^{2+}. His-tagged proteins can self-assemble onto a QD surface at well-defined orientations if the QD surface coating is adequately porous, a requirement met by most new compact multidentate coatings [53, 74, 121] (Figure 3.8b). One disadvantage is that the his-tag-QD interaction is relatively weak (K_D ~10^{-7} to 10^{-10} M) [122], and further studies are needed to see if the his-tag-QD interaction can withstand complex biological environments for long periods of time without dissociation. Nonetheless, the Mattoussi group has shown that DHLA-PEG QDs conjugated to his-tagged peptides are able to retain their integrity in intracellular endosomes up to 72 hours [123, 124]. As an alternative to direct his-tag chelation of the QD surface, Roullier and coworkers used QDs displaying a surface trisNTA moiety to enhance the his-tag binding affinity. By expressing type I interferon receptors fused to a decahistidine tag on the surfaces of cells, the authors could track these receptors on a single-molecule level using QD-trisNTA conjugates [93].

Using a combination of the his-tag and biotin-streptavidin binding techniques, the Ting group has developed an elegant method for achieving monovalent binding (Figure 3.8c). This technique successfully exploits the strength of streptavidin-biotin binding (K_D ~10^{-15} M) while circumventing the multivalency problems associated with native

streptavidin, which contains four biotin-binding sites. First, the authors engineered a monovalent version of streptavidin that can be chelated to DHLA-PEG-QDs using a his-tag. Next, they recombinantly fused their cellular surface protein of interest to a small acceptor peptide that can be biotinylated upon the addition of a biotin ligase known as "BirA." Upon adding BirA, ATP, and biotin to the cellular medium, specific staining could be achieved with monovalent streptavidin-QDs at high affinity. Due to the compact size of the monovalent streptavidin-QDs, Howarth and coworkers were able to successfully track glutamate receptors in crowded neuronal synapses [10].

While Ting's "monovalent streptavidin" technique requires the addition of a separate enzyme to produce labeling, other techniques directly incorporate an enzymatic tag for labeling. As shown in Figure 3.8d, the "HaloTagging" technique employs a 33 kDa haloalkane dehalogenase ("HaloTag protein") that has been mutated to form a covalent bond with a 6-carbon chloroalkane group ("HaloTag ligand"). When the HaloTag protein is genetically fused to the cellular protein of interest, it can readily react with QDs displaying surface HaloTag ligands. We have isolated this technique as a promising candidate for single-molecule imaging studies due to several notable advantages. In addition to the covalent nature of the binding and the small size of the HaloTag ligand, the chloroalkane is able to recognize its target with a fast on-rate ($\sim 2.7 \times 10^{-6}$ $M^{-1}s^{-1}$). Most importantly, HaloTagging is compatible with intracellular labeling, whereas most current techniques are limited only to cell surface labeling [40, 125].

A few other enzymatic labeling techniques have also been applied to QDs. The "SNAP-Tagging" technique involves a 20 kDa human DNA repair protein that has been

mutated to form a covalent bond with O^6-benzylguanine (BG) groups. In the same manner that HaloTag fusion proteins bind covalently to chloroalkane groups, SNAP-Tag proteins can bind covalently to benzylguanine groups, both on the cell surface and intracellularly [126]. One preliminary study has shown that QDs displaying surface BG groups can bind to purified SNAP-Tag proteins in solution, although this technique has not yet been extended successfully to labeling of cellular proteins [127]. Bonasio and coworkers have developed another strategy involving cutinase, a 22 kDa fungal serine esterase that forms covalent adducts with p-nitrophenyl phosphonate presenting alkyl chains. In a proof-of-concept study, Bonasio et al. demonstrated that QDs displaying p-nitrophenyl phosphonate groups could bind to cells expressing cell surface proteins grafted with cutinase [128].

Several other site-specific labeling techniques have been demonstrated with fluorescent dyes, some which may potentially be adopted with QDs [36-39]. These include, but are not limited to affinity methods such as the tetracysteine [129] and oligo-aspartate tags [75], and enzymatic methods such as the CLIP-Tag [130] and acyl carrier protein methods [131]. Table 3.1 summarizes several of the major site-specific labeling techniques described in the literature. Research in new tagging strategies is vital for generating orthogonal labeling techniques that can be used for multi-color QD tracking experiments. Indeed, the possibilities are endless, and new tagging strategies continue to be developed each year [132-136].

Table 3.1. Site-specific tagging strategies for targeting fluorophores to cellular proteins. Reprinted from [37].

Name of tag	Tag (size in amino acids)	Label	Transferase/ligase required?	Intracellular imaging?	Cell-surface imaging?
Labeling by specific chelation of fluorescent ligands					
Tetracysteine (TC)	CCPGCC (6–12)	Biarsenicals: FlAsH, ReAsH, etc.	No	Yes	With reducing agents
Hexahistidine	H6 (6)	Ni–NTA conjugates, Zn conjugates	No	Not shown	Yes
Polyaspartate	D4 × 3 (12)	Zn conjugates	No	Not shown	Yes
Enzyme-catalyzed labeling by post-translational modification					
ACP	ACP (77) or A1 (12)	CoA derivatives	AcpS (PPTase from *E. coli*)	Not shown	Yes
PCP	PCP (80) or S6/ybbR (12)	CoA derivatives	Sfp (PPTase from *Bacillus subtilis*)	Not shown	Yes
Biotin acceptor peptide (AP) or AviTag	Acceptor peptide (13–15)	Biotin plus streptavidin-fluorophores, or reactive biotin analog	BirA (*E. coli* biotin ligase)	Not shown	Yes
Q-tag	PKPQQFM (7)	Cadaverin derivatives	Transglutaminase	Not shown	Yes
Farnesylation motif	CVIA (4)	Geranyl alkyne diphosphate derivatives	Protein farnesyltransferase	Not shown	Not shown
Formyl glycine tag	LCTPSR (6) sulfatase motif	Formyl glycine (for reaction with hydrazides)	Formyl glycine generating enzyme	Not shown	Not shown
Self-labeling					
SNAP-tag	Mutant hAGT (182)	Benzylguanine derivatives	No	Yes	Yes
HaloTag	Mutant dehalogenase (296)	Chloroalkane derivatives	No	Yes	Yes

3.6 Size-Minimized Quantum Dot and Tagging Strategy Selection

Our goal is to engineer a quantum-dot targeting ligand complex that provides enough versatility to accommodate as many different types of single-molecule tracking studies as possible. Ideally, this means that the QD-ligand complex should be compatible with both intracellular and cell surface environments. This would require QDs to be as small as possible while still providing the photostability needed to sustain prolonged UV illumination for long-term tracking. Core-shell QDs composed of materials as CdSe(ZnS) and CdSe(CdS/ZnS) lend far greater photostability than "core-only" QDs such as CdTe, although the latter are slightly smaller in size [47]. Hence, we have chosen to use

CdSe(CdS/CdZnS/ZnS) QDs, taking advantage of novel surface coatings to reduce QD size.

As a surface coating, we have chosen to use the multidentate polymer coating (Figure 1c) previously engineered in our laboratory [50, 51]. Multidentate-coatings QDs offer greater stability than bidentate coatings (Figure 1b), and a flat-wrapping conformation results in a smaller size than the extended-brush conformation of bidentate ligands. Moreover, the multidentate polyacrylic acid-based polymer contains several convenient functional groups, including carboxylic acids, thiols, and amines, readily available for bioconjugation.

After carefully considering the plethora of site-specific tagging strategies that have been used previously with fluorescent dyes, we chose the HaloTag tagging strategy based on the following four criteria: (1) labeling kinetics/speed of reaction, (2) quantum dot compatibility, (3) intracellular compatibility, (4) tag size, and (5) feasibility of use. Thus far, very few existing techniques are compatible with intracellular imaging. Of the site-specific labeling strategies listed in Table 3.1, only three techniques—tetracysteine, SNAP-Tag, and HaloTag labeling—are compatible with intracellular labeling. Of these three techniques, the compatibility of tetracysteine tagging with QD use remains questionable. While the tetracysteine tag may potentially chelate the surface of QDs containing cadmium and zinc, it is unclear whether the binding affinity will be strong enough to withstand harsh biological environments.

Both the SNAP-Tag and HaloTag labeling strategies result in covalent binding to their targets. Although the SNAP-Tag (~20 kDa) is slightly smaller in size than the HaloTag (33 kDa), it exhibits much slower labeling kinetics than the HaloTag. The

second-order rate constant for HaloTag protein binding to TMR ligand, a HaloTag ligand-fluorescent dye conjugate, is measured to be $2.7 \times 10^6\ M^{-1}\ s^{-1}$, only slightly lower than the second-order rate constant for streptavidin binding to biotin ($8.5 \times 10^6\ M^{-1}\ s^{-1}$). As a result, the HaloTag binding reaction reaches completion in less than 5 minutes at 25 ^{0}C [40]. In contrast, the second-order rate constant for SNAP-Tag binding to benzylguanine is only 3000 $M^{-1}\ s^{-1}$ [126].

Another particularly attractive advantage is that the HaloTag technology is further developed and more thoroughly characterized than many of the other tagging strategies. Several HaloTag vectors and fluorescent ligands are already commercially available through Promega Corporation (Madison, Wisconsin). The binding specificity of the HaloTag ligand to both intracellular and cell surface HaloTag protein has also been thoroughly demonstrated. For example, Los and coworkers showed that the TMR ligand could specifically bind to an intracellular p65-HaloTag fusion protein inside the cytoplasm of living cells. In this experiment, HeLa cells were transfected with the p65-HaloTag protein and stained with TMR ligand. The cell lysate was subsequently collected and resolved using an SDS-PAGE gel. A fluorescent band corresponding to the TMR ligand-labeled p65-HaloTag protein was found only in transfected cells; nontransfected cells stained with TMR ligand exhibited no fluorescent protein bands. These results indicate that the HaloTag ligand can indeed recognize target HaloTag protein with high specificity in complex intracellular environments [40]. In another experiment, Svendsen and coworkers showed that HEK293 cells expressing a surface HaloTag protein could be labeled with biotinylated HaloTag ligand and captured onto streptavidin coated plates. Native HEK293 cells labeled with biotinylated HaloTag ligand

remained uncaptured, thereby demonstrating specific binding of the HaloTag ligand to cell surface HaloTag proteins [137]. Altogether, the high specificity of HaloTag binding has permitted its successful application in a wide range of cellular and *in vivo* imaging studies [138-142]. Based on these initial qualities, the HaloTag strategy appears to be a promising tagging strategy for designing size-minimized QD probes for cellular imaging.

3.7 Conclusions

In recent years new strategies for reducing the size of quantum dots have emerged along with improved tagging strategies for site-specifically labeling target proteins. These strategies have the potential to greatly advance the field of quantum dot imaging by improving QD access to many regions of the cell. In particular, the HaloTag strategy is especially noteworthy due to its covalent nature, fast labeling kinetics, and ability to be used intracellularly. Early reports have indicated that HaloTag ligands can indeed be coupled to commercial QDs, and that the resulting conjugates do retain their ability to bind HaloTag protein [125, 143]. The next step is to investigate whether this technology can be translated into a size-minimized technology. In the remaining chapters, we will investigate whether size-minimized HaloTag ligands can be coupled to size-minimized multidentate polymer coated QDs. It will be critical to determine if QD-HTL conjugates can bind to their target proteins at the low staining concentrations required for single-molecule imaging. It will also be fundamentally important to determine whether QD-HTLs can be prepared at the monovalency required to prevent receptor crosslinking.

This work is *significant* because it will present a systematic study of the parameters needed to optimize HaloTagging as a direct QD labeling procedure. It is the first study that seeks to optimize an entirely covalent strategy for site-specifically labeling

and tracking cellular proteins using small QDs. It is the first study that seeks to apply size-minimized quantum dot-HaloTag ligand conjugates for single-molecule imaging in live cells. Finally, this work is *significant* due to its potential for intracellular labeling. This work will shed new insight on the interaction between QDs and covalent size-minimized tagging strategies, establishing a foundation of knowledge for developing new technologies that transform our ability to visualize cellular and molecular interactions.

CHAPTER 4

SYNTHESIS AND CHARACTERIZATION OF SIZE-MINIMIZED QUANTUM DOT-HALOTAG LIGAND CONJUGATES

4.1 Introduction

The goal of our study is to engineer a quantum dot targeting ligand complex that provides enough versatility to perform single-molecule imaging under a wide variety of cellular conditions. As discussed in Chapter 3, we have isolated the HaloTag tagging strategy as having exceptional promise for single-molecule QD imaging due to its covalent nature and potential for intracellular labeling. We have further decided to use this tagging strategy in conjunction with in size-minimized multidentate polymer coated QDs, which have been shown to exhibit high colloidal stability in complex biological environments compared to other types of small QDs. The rationale is that small QD-targeting ligand constructs are necessary to diffuse in cell interiors, and that a covalent strategy is ideal for preventing dissociation of the QD from the protein of interest during imaging.

In this chapter, we seek to identify the reaction conditions needed to react the HaloTag ligand with compact multidentate polymer coated QDs. We seek to optimize the quantum dot surface chemistry needed to achieve specific binding between QD-HTL conjugates and their target HaloTag proteins. As a preface to investigating the performance of our QD-HTL conjugates in more complex cellular environments, we will assess their binding to purified HaloTag protein in simple aqueous solutions.

Although our primary focus is to use QD-HTLs for direct targeting of specific proteins in the cellular context, purified QD-HaloTag fusion protein conjugates have a wide variety of uses. QD-HaloTag fusions with fluorescence proteins or luciferases can be used as fluorescence or bioluminescence resonance energy transfer (FRET or BRET) sensors [143]. As an alternative to direct targeting of cellular HTP, QDs can first be assembled with HaloTagged proteins of interest *in vitro* prior to delivery into living cells or whole organisms. In all of these methods, the HaloTag strategy offers the advantage of providing covalent conjugation at a controlled orientation and stoichiometry. Thus, a systematic characterization of QD-HTL binding to purified HaloTag protein, as presented in this chapter, will be beneficial not only for cellular labeling, but for all of these applications.

4.2 Materials and Methods

Multidentate Polymer Coated Quantum Dots

CdSe(CdS/CdZnS/ZnS) QDs were synthesized according to the following procedure. Briefly CdSe QD "cores" of roughly 3.43 nm were synthesized as previously described [144] and then purified from unreacted precursors via extraction with hexane and methanol three times [145]. The QDs in the hexane layer were collected into a 50 ml centrifuge tube and precipitated using an excess of acetone. Following centrifugation at 5000 g for 15 min, insoluble QDs were resuspended in a mixture of octadecene and oleic acid. The CdSe QDs were then capped with two monolayers of CdS, one monolayer of CdZnS, and one and a half monolayers of ZnS while gradually increasing the temperature from 160 to 220 ^{0}C [63, 64, 66]. The resulting QD mixture was cooled to room temperature and purified with six rounds of hexane-methanol extraction. Again, the QDs

were precipitated using acetone and pelleted by centrifugation at 5000 g for 15 min. Finally, the purified QDs were resuspended in chloroform, where they could be stored long term at -20 ^{0}C. The theoretical QD size was calculated from its known correlation with the first exciton peak [145-147], and also verified empirically using TEM. CdSe(CdS/CdZnS/ZnS) QDs were subsequently coated with multidentate polymer as detailed extensively by Nie et al [51].

HaloTag Ligands

Nitrophenol carbonate terminated HaloTag ligands of two sizes, 700 MW (697.16 g/mol) and 2500 MW (~2503 g/mol) were generously synthesized by Promega Corporation. 500 MW (508.99 g/mol) succinimidyl ester O4 ligand was purchased from Promega Corporation. The structure of these ligands is displayed in Figure 4.2. HaloTag ligands were typically dissolved to 100 mM stock concentrations in anhydrous DMSO, aliquoted and stored in a dessicator at -20 ^{0}C.

Polyethylene Glycols

1000 MW PEG (1074.20 g/mol, amino-dPEG24-alcohol) and 370 MW PEG (369.45 g/mol, amino-dPEG8-alcohol) were obtained from Quanta Biodesign. 2000 MW PEG (CH_3O-PEG-NH_2) was obtained from Rapp Polymere. 1000 MW Fluorescein-PEG-amine (FITC-PEG-NH2) was obtained from Nanocs.

Determination of Nitrophenol Carbonate HaloTag Ligand-Quantum Dot Reaction Kinetics

The nitrophenol carbonate group of the 700 and 2500 MW HTLs react with primary amines of the QD multidentate polymer coating under basic pH (pH 8-10) to

produce a covalent urethane linkage [148] (Figure 4.1). For determination of the reaction kinetics between nitrophenol carbonate HTLs and multidentate polymer coated QDs, a 10-fold molar excess of HTLs was incubated with QDs in 10 mM borate buffer (pH 8.5) at 27 ^{0}C. Simultaneously, an identical sample was prepared containing only HTL at the identical concentration. Nitrophenol absorbance at 400 nm was monitored at several time points over the course of a 24 hour period. To obtain the final reaction kinetic curve, absorbance of the "ligand only" sample was subtracted from the QD-ligand reaction sample to account for hydrolysis of the ligand over time. This procedure was performed for both 700 MW and 2500 MW ligands.

Quantum Dot Surface Functionalization with Nitrophenol Carbonate HaloTag Ligands

Nitrophenol carbonate HaloTag ligands were added dropwise to QDs and allowed to react in 10 mM borate buffer (pH 8.5) while stirring for at least 20 hours at 27 ^{0}C. Nitrophenol by-product and unreacted ligand were then either removed with ultrafiltration or dialysis, as described below. For non-pegylated QD-HTLs, the final QD-HTLs were collected into PBS buffer (pH 7.4). If subsequent PEG modification was desired, QD-HTLs were collected into 25 mM MES buffer (pH 6). Final conjugates were centrifuged at 7000 g for 10 minutes to remove aggregates.

Quantum Dot Surface Functionalization with Succinimidyl Ester HaloTag Ligands

Succinimidyl ester HaloTag ligands were added dropwise to QDs and allowed to react in 10 mM borate buffer (pH 8.5) while stirring for at least 20 hours at 27 ^{0}C. Succinimide by-product and unreacted ligand were then either removed with

ultrafiltration or dialysis, as described below. Final QD-HTLs were collected into PBS buffer (pH 7.4).

Pegylation of Quantum Dot-HaloTag Ligand Conjugates

Linear PEG polymers containing terminal amine groups were reacted to carboxylic acids on the multidentate polymer coated QDs using standard carbodiimide chemistry. Briefly, a solution of 1-ethyl-3-(3-dimethylaminopropyl)carbodiimide (EDC) crosslinking reagent (Sigma Aldrich) was added dropwise to a well-stirred solution of QD-HTLs and amine-terminated PEGs in 25 mM MES (pH 6) and allowed to react overnight at 27 ^{0}C.

To optimize the pegylation procedure, parameters affecting the stability of the PEG-QD conjugates were investigated. QD samples containing various amounts of PEG (from 5 to 200,000 molar excess) and EDC (from 1,000 to 100,000 molar excess) were monitored over the course of a week. Samples were examined using three methods: (1) visually, for examination of pellet; (2) by spectrofluorometry to detect loss of fluorescence intensity; and (3) by gel electrophoresis to detect aggregation. Additionally, gel electrophoresis was used to determine the amount of PEG needed to completely coat the QD surface.

Purification of Quantum Dot-HaloTag Ligand Conjugates

Two different methods of purifying QD-HTL conjugates were investigated: (1) purification using ultrafiltration columns and (2) dialysis. In the first method, ~200 µl of QD-HTL was loaded into a Nanosep 10K centrifugal device (Pall Lifesciences) and centrifuged at 6000 rpm for 5 min. The retentate was resuspended back to 200 µl in PBS, and the centrifugation was repeated. Samples were typically purified with 2-4 rounds of

centrifugation at 6000 rpm for 5 min each, depending on the amount of excess HTL used during reaction. If subsequent pegylation was required, QD-HTL samples were collected into MES buffer during the final round of centrifugation.

In the second method, QD-HTL samples were dialyzed in PBS using 20K molecular weight cutoff (MWCO) Slide-a-lyzer MINI dialysis devices (Thermo Scientific Pierce) with at least 5 buffer changes over the course of 3 hours, then allowed to dialyze overnight with one final buffer change. If subsequent pegylation was required, QD-HTL samples were exchanged into MES buffer during the final few rounds of dialysis.

For pegylated QD-HTLs, the number and placement of the purification steps was also investigated. QD-HTLs were either purified (1) before pegylation, (2) after pegylation, or (3) both prior to and after pegylation.

Estimation of the Number of PEGs on the Quantum Dot Surface

The number of PEG molecules on the surface of the QD was estimated using fluorescein terminated PEG. QDs were reacted with 10,000 molar excess of fluorescein-1K PEG-amine (Nanocs, Inc) using 7,500 molar excess of EDC. The resulting conjugates were loaded into 20K MWCO dialysis units and dialyzed extensively into PBS for 4 days. A control sample containing only QDs and 10,000 excess fluorescein-1K PEG was simultaneously purified to ensure complete removal of fluorescein-1K PEG. Upon purification, the number of PEGs on the QD surface was estimated using the extinction coefficient of FITC-PEG at its absorption peak in PBS (77,000 $M^{-1}cm^{-1}$ at 490 nm).

Estimation of the Number of HaloTag Ligands on the Quantum Dot Surface

The number of ligands on the QD surface was estimated by comparing the number of free primary amines on the QD before and after conjugation with HTL, as measured using a fluorescamine assay. A series of glycine standards ranging from 500 nM to 20 µM was prepared in 50 mM borate buffer (pH 8.5), and a 5 mg/ml solution of fluorescamine was freshly prepared in DMSO. The assay was initiated by mixing equal parts of fluorescamine solution with glycine standard. After 30 minutes of reaction in the dark, the fluorescence intensity was measured at 470 nm using 380 nm excitation. In the same manner, a series of QD-HTLs containing various amounts of ligand on the surface were prepared in 50 mM borate buffer and assayed at a final concentration of 600 nM.

QD-HTL Hydrodynamic Size Analysis

The hydrodynamic size of the QD-HTLs was determined by dynamic light scattering (DLS) using a Brookhaven Instruments 90Plus Particle Size Analyzer. In general, 300 µl of at least 750 nM of QD-HTL was required in order to achieve an ideal count rate of 1 million counts per second and a sample quality ranging from 9-10 (with 10 being the highest quality). To ensure complete removal of by-products and unreacted reagents, which can interfere with size measurement, samples were dialyzed in PBS using 20K MWCO Slide-a-lyzer MINI dialysis devices (Thermo Scientific Pierce) with 8 buffer changes for 22 hours before DLS measurement. Samples were sonicated for 15 min immediately prior to start. Typically, the experiment was carried out for 3 runs of 2 minutes each and analyzed using the “number” (first-order) Multimodal Size Distribution.

QD-HTL UV-Vis Absorption and Photoluminescence Spectra

Absorption spectra were measured on a Shimadzu UV-2401PC scanning spectrophotometer. Photoluminescence spectra were measured on a spectrofluorometer from Photon Technology International with a xenon excitation lamp and photomultiplier tube detector.

TEM Imaging

TEM imaging was used to validate the size of the QDs after synthesis. Briefly, 5 µl of QD sample was pipette onto a carbon TEM grid. After 15 minutes, the solvents were slowly wicked away with filter paper. For visualization of the polymer shell, samples were counterstained with a 1% phosphotungstic acid solution (pH 6) for 30 seconds. Again, the staining solution was slowly wicked away with filter paper and allowed to dry. TEM grids were imaged on a Hitachi H-7500 Transmission Electron Microscope at an acceleration voltage of 80 kV.

QD-HTL and HTP Gel Electrophoresis Binding Assays

Samples were resolved using a 1% (w/v) agarose gel in 50 mM borate buffer (pH 8.5). Briefly, 250 mg of agarose (EMD Biosciences) was weighed into a 250 ml beaker, to which 50 ml of 50 mM borate buffer was added. The solution was heated in a microwave until completely dissolved, and subsequently cast into a gel electrophoresis tray with a 1.5 mm 15 well comb. Meanwhile, QD-HTLs samples were incubated with HaloTag protein (HaloTag standard protein, Promega Corporation) or an equivalent concentration of cell lysate (non-denatured U2OS cell lysate, Abnova) in mg/ml. Samples were allowed to incubate for 30 min at room temperature from the start of incubation to the start of the electrophoresis run, unless indicated otherwise. Once the gel

solidified, it was loaded into a gel electrophoresis tank (Mini-SubCell GT, Bio-Rad) and fully submerged in 50 mM borate buffer as the running buffer. 18 µl of sample was loaded into each well along with 2 µl of 10x borate loading buffer (500 mM borate, 25% v/v glycerol, 0.25% w/v Orange-G dye). Gels were run for 20 minutes at 100 V using a Bio-Rad Power Pac Basic and imaged using a Bio-Rad Gel Reader.

4.3 Results and Discussion

Quantum Dot-HaloTag Ligand Development and Conjugate Design

Thus far, there have only been a few literature reports employing HaloTagged nanoparticles for cellular studies. The HaloTag-nanoparticle conjugates used in these studies have mainly been assembled using commercially available nanoparticles. The first study, performed by So et. al, utilized commercial streptavidin-QDs coupled to biotinylated HaloTag ligands [125]. A second study performed by Liβe et al. reported great difficulties with nonspecific binding when using commercially available QDs. Unable to achieve any specific cellular staining with QDs, the authors chose instead to conjugate HTLs to commercially available dye-loaded polystyrene nanoparticles. These fluorescent nanoparticles were coupled to HTLs using click chemistry by reacting dibenzocyclooctyne-functionalized fluorescent nanoparticles to azide-functionalized HTLs [149].

We sought to improve upon these existing methods by (1), using smaller QDs than currently available on the commercial market and (2), attaching the HTL directly to the QD without the presence of any bulky intermediate groups. Instead of using a non-covalent conjugation strategy like the biotin-streptavidin interaction, we sought to attach the HTL covalently to the QD surface. We further sought to reconcile some of the

differences between the studies performed by So and Liβe by investigating whether changes in surface parameters such as linker length play a role in determining binding specificity.

Our multidentate polymer coated QDs serve as an ideal “size-minimized” alternative to commercial, amphiphilic polymer coated QDs. Our lab has previously shown that a multidentate polymer coated QD is roughly only half the size of an amphiphilic polymer coated QD of the same wavelength and core size. Furthermore, the multidentate polymer contains several convenient functional groups readily available for bioconjugation [51], as shown in Figure 3.7c. For example, a red CdSe(CdS/CdZnS/ZnS) quantum dot coated with multidentate polymer contains roughly twenty amines, twenty thiols, and tens of thousands of carboxylic acids available for conjugation.

Although many available options exist for covalent conjugation with these functional groups, we chose to react nitrophenol carbonate terminated HaloTag ligands with QD surface amines to produce the QD-HTL (Figure 4.1). Nitrophenol carbonate is a good choice for several reasons—it hydrolyzes slowly and is compatible for use in both aqueous and organic solvents. Moreover, the stability of the urethane linkage under stringent conditions has already been demonstrated [148]. One especially fortuitous advantage is that the absorbance of the yellow 4-nitrophenol byproduct, which absorbs strongly at 400 nm, can be used to monitor the kinetics of the reaction between the HTL and QD. By choosing to react the HTLs with the surface amines, the tens of thousands of carboxylic acids can then be functionalized with PEG molecules to reduce nonspecific binding.

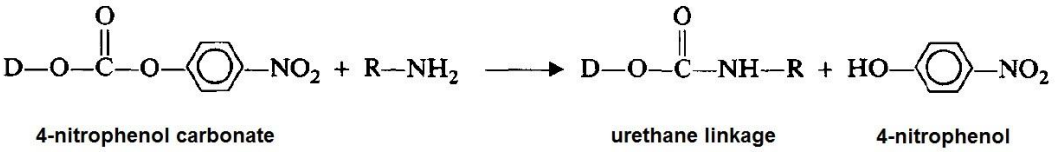

Figure 4.1. Reaction chemistry between nitrophenol carbonate HaloTag ligands and QD surface amines. "D" = HaloTag ligand. "R" = Multidentate polymer coated QD. Figure adapted from [148].

Despite the fact that the chloroalkane linker on Promega's fluorescent dye-HaloTag ligand conjugates is only ~250 g/mol in molecular weight (MW), preliminary evidence from several sources [40, 125, 149] has suggested that chloroalkane linkers of longer lengths should be used with nanoparticles to reduce steric hindrance of binding. The longest commercially available ligand, the Promega O4 succinimidyl ester ligand, is roughly 500 MW. We chose two more ligands of higher molecular weights, 700 and 2500 MW, to investigate the effects of linker length on HaloTag binding ability. As shown in Figure 4.2, the 6-carbon chloroalkane group remains constant for each HaloTag ligand, with any differences in ligand length arising predominantly from changes in the length of the PEG linker.

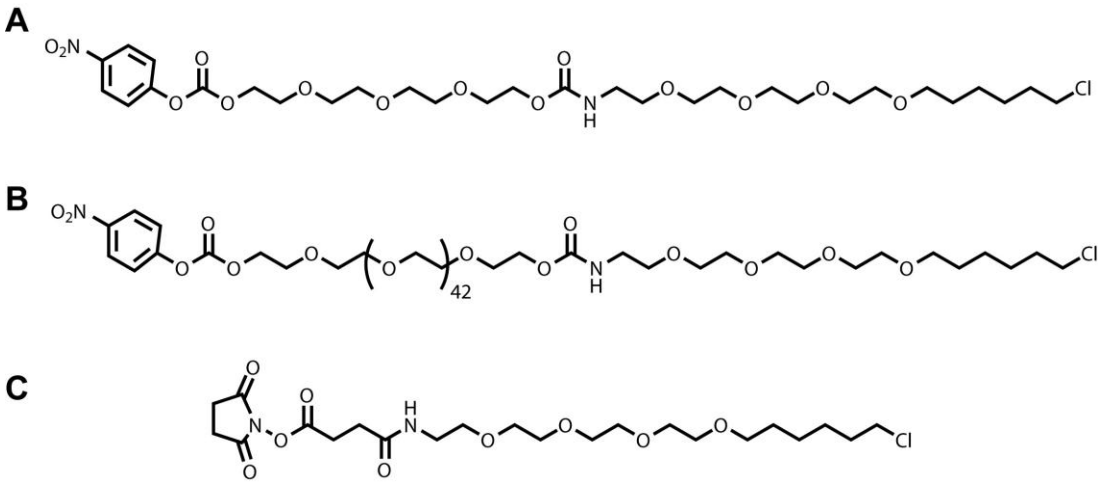

Figure 4.2. Structure of HaloTag ligands. (a) 700 MW Nitrophenol Carbonate HaloTag ligand (697.16 g/mol) (b) 2500 MW Nitrophenol Carbonate HaloTag ligand (2503.35 g/mol) (c) Succinimidyl ester O4 ligand (508.99 g/mol).

Multidentate Polymer Quantum Dot Synthesis and Characterization

Red CdSe(CdS/CdZnS/ZnS) QD of 629 nm emission were synthesized and used throughout the work. The absorption and emission spectra of the synthesized QDs are displayed in Figure 4.3.

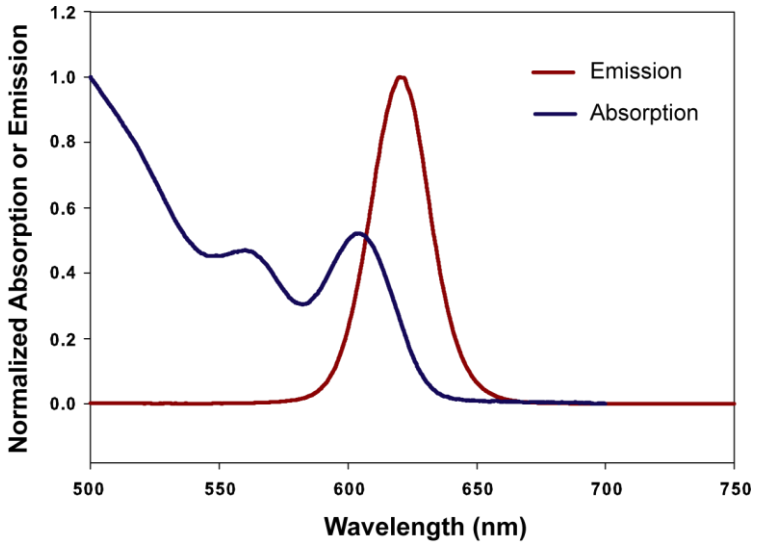

Figure 4.3. Normalized absorption and emission spectra of CdSe(CdS/CdZnS/ZnS) QDs. The absorption spectrum is indicated in blue, and the emission spectrum is indicated in red.

As shown in Figure 4.4, a TEM image of the synthesized QDs shows that the QDs are fairly monodisperse. An analysis of 100 particles in the TEM image indicates that these QDs have an average size of 6.1 nm. This size is in close agreement with the theoretical diameter of predicted by known correlation with the first exciton peak. A summary of the properties of the QDs prior to multidentate polymer coating can be found in Table 4.1.

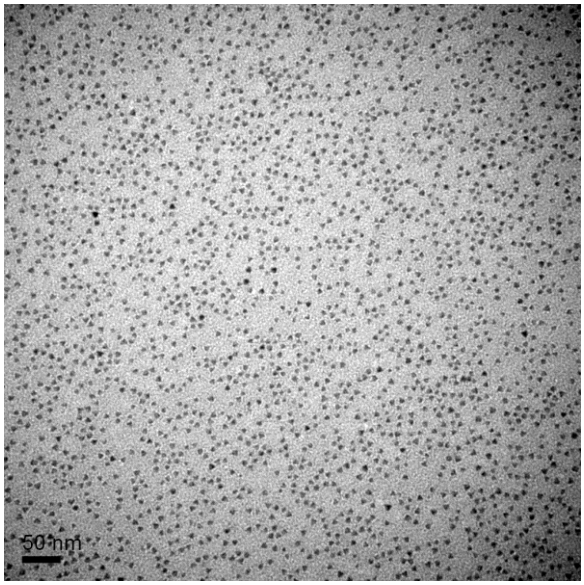

Figure 4.4. TEM image of CdSe(CdS/CdZnS/ZnS) QDs.

Table 4.1. Composition and spectral properties of CdSe(CdS/CdZnS/ZnS) QDs prior to multidentate polymer coating.

Core Material	Core Diameter (nm)	Shell Composition	Shell Thickness (monolayers)	Theoretical Diameter (nm)	Diameter by TEM (nm)	1st Exciton Peak (nm)	Extinction Coefficient at 1st Exciton Peak ($M^{-1}cm^{-1}$)	Fluorescence Peak (nm)	FWHM (nm)
CdSe	3.43	CdS/CdZnS/ZnS	2/1/1.5	6	6.1	606	194,600	628.5	28.5

Upon coating the QD with multidentate polymer in DMSO, QDs were phase transferred to aqueous solution for subsequent conjugation reactions. Coating with multidentate polymer and subsequent phase transfer to water produced no significant changes to the absorption and emission spectra of the QDs. The average hydrodynamic size of the polymer coated QD in PBS was determined to be 7.5 nm as measured by DLS (Figure 4.14).

Quantum Dot Surface Functionalization with Nitrophenol Carbonate Ligands

We chose to modify the QD with the HaloTag ligand after coating the surface with the multidentate polymer, rather than making ligand modifications to the polymer prior to coating the QD. The former method grants us more precise control over the exact surface chemistry and helps ensure that the functional groups of the conjugated ligands do not interfere with the coating process. We also chose to carry out conjugation reactions in aqueous solution rather than DMSO, as multidentate polymer coated QDs were observed to have greater long term stability in water than organic solvent.

Reactions between QD and nitrophenol carbonate terminated HaloTag ligands were performed in aqueous solution at room temperature at pH 8.5. The basic pH is crucial for ensuring the QD surface amines are deprotonated for the reaction to proceed. By monitoring the kinetics of the release of the nitrophenol group, we found that the reaction between QD and HaloTag ligand reaches equilibrium in 18-20 hours under these conditions (Figure 4.5). Henceforth, HTLs were allowed to react with QDs for at least 20 hours before subsequent purification.

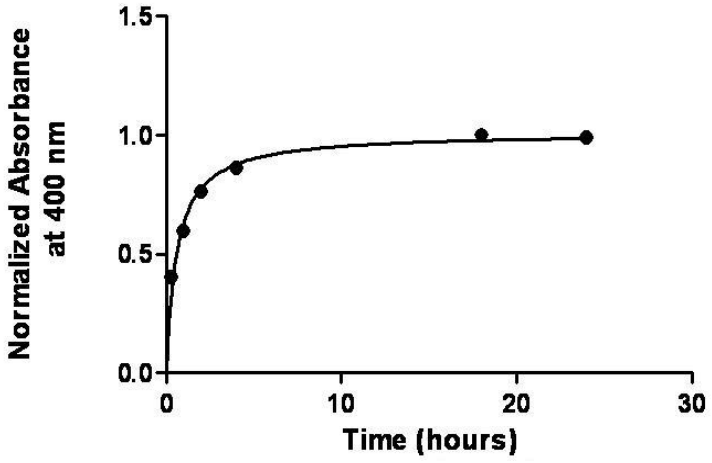

Figure 4.5. Reaction kinetics of nitrophenol carbonate HaloTag Ligands to multidentate polymer coated QDs. Reaction was performed with a ten-fold molar excess of 2500 MW nitrophenol carbonate ligand to QD at room temperature and pH 8.5, with a final QD reaction concentration of 900 nM.

As previously stated, the reaction was carried out in aqueous solution due to the increased long term stability of multidentate polymer QDs in water. However, one disadvantage of performing an aqueous reaction is that the nitrophenol carbonate ligand hydrolyzes much more rapidly in water than in organic solvent. To address this issue, nitrophenol carbonate ligands were first diluted to in anhydrous DMSO to the appropriate concentration before addition to an aqueous solution of QDs. The amount of DMSO added to the reaction volume was optimized accordingly. When the amount of ligand in DMSO added was less than 10% of the final reaction volume, we found that the ligand hydrolyzed too rapidly for efficient reaction to occur. On the contrary, if the amount of ligand added exceeded 20%, the resulting QD-HTL conjugates were difficult to purify due to the incompatibility of many purification membranes with high concentrations of DMSO. Henceforth, we made sure the amount of ligand added during reaction was between 10-15% of the final reaction volume.

Purification of Quantum Dot-HaloTag Ligand Conjugates

The purpose of purifying the resulting QD-HTL conjugates is to remove any unreacted ligand as well as 4-nitrophenol by-product. Removing unreacted ligand is essential as free ligands will compete against QD-HTLs for binding with HTP, and excess nitrophenol may cause toxicity to cells.

Two different methods were examined for the purification of QD-HTL conjugates: ultrafiltration and dialysis. Both methods rely on a size difference between the sample and by-product as the basis for purification, utilizing a porous membrane and a driving force for removal of by-products. Ultrafiltration is a popular method in the literature for purifying free ligand from QD, and is also the method of choice employed by So et al. to remove unreacted biotinylated HTLs from streptavidin-QDs [53, 125, 127]. Like So, we chose to use the 10K Nanosep filter available from Pall Lifesciences, which utilizes centrifugation as the driving force for purification. In this device, buffer containing the QD-HTL sample is loaded on top of a porous membrane. During centrifugation, molecules smaller than the molecular weight cutoff are eluted through the membrane, while the QD-HTLs are retained at the top of the membrane. Dialysis uses an osmotic pressure gradient for removal of unwanted by-products. Samples are loaded into a semi-permeable membrane and placed in a large tank of buffer, allowing small by-products to diffuse out of the membrane according to their concentration gradient. For dialysis, we used 20K MWCO Slide-a-lyzer Mini Dialysis Devices available from Thermo Scientific Pierce.

In both of these methods, selection of an appropriate molecular weight cutoff is critical. In general, the MWCO should be at most half the molecular weight of the

product to be retained and at least twice the molecular weight of the product to be removed [150]. According to Fast Performance Liquid Chromatography (FPLC) studies comparing the size of our multidentate polymer QD to protein standards of known molecular weight, a QD with 7.5 nm hydrodynamic diameter roughly corresponds to a molecular weight of 100 kDa. Thus, a molecular weight cutoff of 10-20 kDa was well-suited for removing 2500 MW HaloTag ligands and smaller by-products from the QD-HTL conjugates.

Both ultrafiltration and dialysis have their advantages and disadvantages. Ultrafiltration has the advantage of being a rapid procedure, allowing purification to be completed in less than an hour. However, centrifugation can be relatively harsh on the nanoparticles, and special care was taken to minimize the speed of centrifugation as much as possible. We found that repeated centrifugation (6 or more repetitions) can result in a moderate amount of aggregation. In general, we tried to limit the QD-HTL conjugates to at most 4 rounds of centrifugation. When present, aggregates could be pelleted and removed by centrifugation at 7500 rpm or by passing the sample through a 0.2 μm syringe filter.

In contrast, dialysis is a far gentler procedure, resulting in little to no aggregation. Dialysis has the disadvantage of being a time consuming process, requiring several buffer changes over several days to achieve the same purity as ultrafiltration. Moreover, dialysis requires several liters of buffer, making it a potentially expensive process if dialyzing into special buffers other than water or PBS.

Figure 4.6 depicts the difference between QD-HTL conjugates purified using these two purification procedures. In this experiment, QD-HTL conjugates were purified

with either ultrafiltration or dialysis and then incubated with HTP for 30 minutes. The samples were subsequently resolved using agarose gel electrophoresis, a technique for separating macromolecules based on their size and charge. Due to the negative zeta potential of the multidentate polymer QDs, QD-HTLs migrate to the cathode, located at the bottom of the gel image. Binding to HTP results in slower migration and a band shift towards the anode due to an increase in size and reduced charges from protein shielding.

QD-HTL conjugates purified by ultrafiltration produced broad, smear-like bands in gel electrophoresis. Interestingly, other researchers have likewise observed this smear when performing gel electrophoresis with QD conjugates purified by ultrafiltration [127]. While Petershans and coworkers had attributed the smear to broad distributions in the number of proteins bound to the QD surface, our experiments indicate that the smear can be almost entirely abolished by changing the purification procedure to dialysis. While the exact reason for smearing remains unknown, it is possible that the centrifugation process may introduce slight rearrangements to the QD coating, causing a change in the size distribution of some of the particles. Nonetheless, ultrafiltration does not seem to adversely affect QD-HTL binding ability, and conjugates purified by ultrafiltration still retain their capacity to bind to HTP as well as those purified by dialysis.

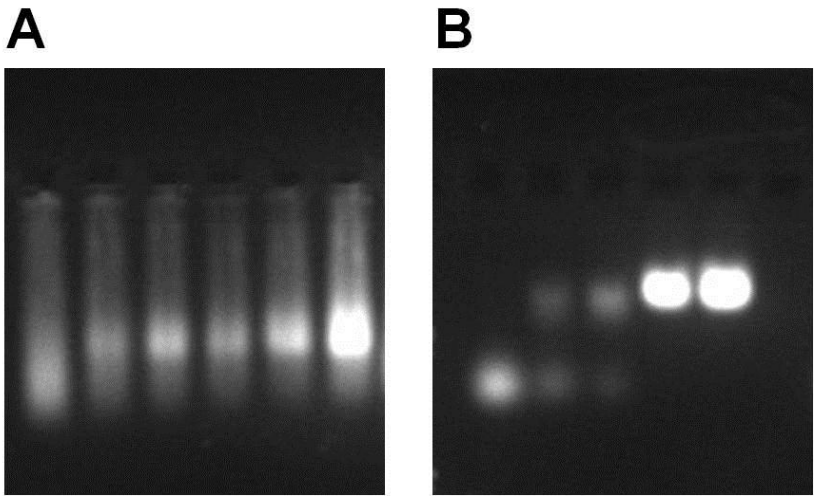

Figure 4.6. Agarose gel images comparing QD-HTL conjugates purified with different purification methods. QD-HTL conjugates were purified via (a) ultrafiltration, and (b) dialysis. In each gel image, QD-HTLs in leftmost lane are exposed to increasing amounts of HTP from left to right.

Effect of HaloTag Ligand Length on HaloTag Protein Binding Ability

Preliminary evidence from the literature suggests that the HaloTag ligand length—i.e. the length of the linker between the QD and the terminal chloroalkane group—can have a significant effect on the binding capability of the QD-HTL. So and coworkers utilized biotinylated HTLs of two different lengths, roughly 610 MW and 730 MW, that differed from each other by only 2 ethylene glycol repeats. They found that QD-HTLs comprised of the longer ligand had better water solubility, resulting in better cellular labeling efficiency, whereas QD-HTLs made using the shorter ligand tended to aggregate easily [125].

Studies performed by Liβe et al. also seem to suggest that the length of the HaloTag ligand may affect the binding rate constant. Liβe and coworkers compared two different nanoparticle-HTL conjugates, one functionalized with Promega's HaloTag thiol

O4 ligand, and one functionalized with a novel click-chemistry-based HTL. By monitoring the real time kinetics of HTP binding, they showed that the click-chemistry-based HTL exhibited a 10-fold faster binding reaction rate than the thiol-HTL. Although the authors attributed the difference in reaction rate to the presence of the hydrophobic "click" moiety, which they argue helps to stabilize the HaloTag enzyme-substrate complex, we noted that a difference in ligand length may be partially responsible for the improved reaction rate [149]. The Promega HaloTag thiol O4 ligand is only about 330 Da, whereas Liβe's novel click-based ligand is over 1400 Da in molecular weight. However, the authors did not independently examine the effects of ligand length and the presence of the click group on the binding reaction rate constant. We hypothesized that the increased ligand length could facilitate binding of the QD-HTL to HTP by reducing the effect of steric hindrance.

Our preliminary results suggested that chloroalkane ligands with long ethylene glycol linkers are indeed more effective at binding HaloTag protein (HTP) than their shorter counterparts. When commercially available succinimidyl ester O4 HTLs of ~500 MW (4 ethylene glycol repeats) were conjugated to multidentate polymer coated QDs, little binding to purified HTP could be detected. Figure 4.7 shows the results of a gel electrophoresis assay performed to assess the binding capacity of QDs conjugated to these succinimidyl ester O4 ligands. HTLs were reacted with QDs at a molar reaction ratio ranging from 1 to 100 ligands per QD, as denoted in green. In the presence of HaloTag protein (Lanes #6 – 9), most QD-HTL conjugates remain unbound to protein, and there is little evidence of a band shift to indicate protein binding. This holds true regardless of the number of ligands on the QD surface. As shown on the right-hand side

of Figure 4.7, the controls consist of QDs without any HaloTag ligands on their surface. In the presence of HaloTag protein, QDs without ligand exhibit low nonspecific binding (Lane #12).

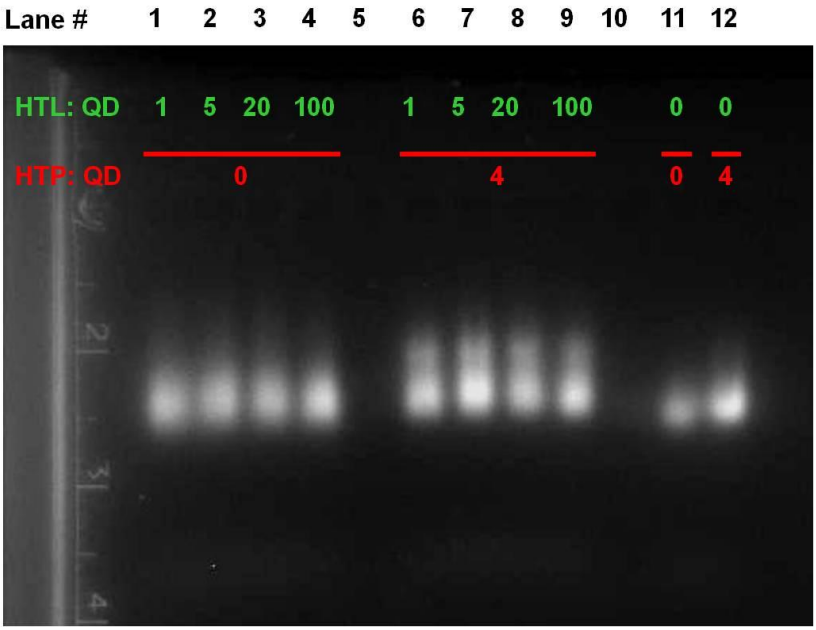

Figure 4.7. Gel electrophoresis mobility assay assessing the binding ability of QDs conjugated to O4-succinimidyl ester 500 MW HaloTag ligands. QDs were reacted with 500 MW HTLs at the HTL:QD molar ratio indicated in green. Resulting QD-HTLs were subsequently incubated with HaloTag protein at the HTP:QD molar ratio indicated in red.

In contrast, both 700 MW HTL (8 ethylene glycol repeats), and 2500 MW HTL (~50 ethylene glycol repeats) show effective binding to purified HTP upon QD conjugation. Figure 4.8 shows the results of an electrophoresis assay performed to simultaneously assess the effects of HaloTag ligand length and ligand density on QD-HTL binding capacity. Three different ligand densities (1:1, 5:1, and 20:1 HTL:QD) were studied for two ligand lengths (700 and 2500 MW). The controls are comprised of QDs

without any HaloTag ligands on their surface. In the presence of HaloTag protein, control QDs exhibit minimal nonspecific binding (Lane #8).

As shown in Figure 4.8, a band shift can be clearly seen when the QD-HTLs are incubated with HaloTag protein (Lanes #4 – 6). This shift is evident for both 700 and 2500 molecular weights, even when only one HaloTag ligand per QD is present (Lane #4). In these lanes, QD-HTLs that are bound to HTP can be clearly distinguished from those that remain unbound. In conclusion, both 700 and 2500 MW ligands retain their ability to bind soluble HaloTag protein specifically when conjugated to QDs. This holds true, even for low ligand densities down to one ligand per QD.

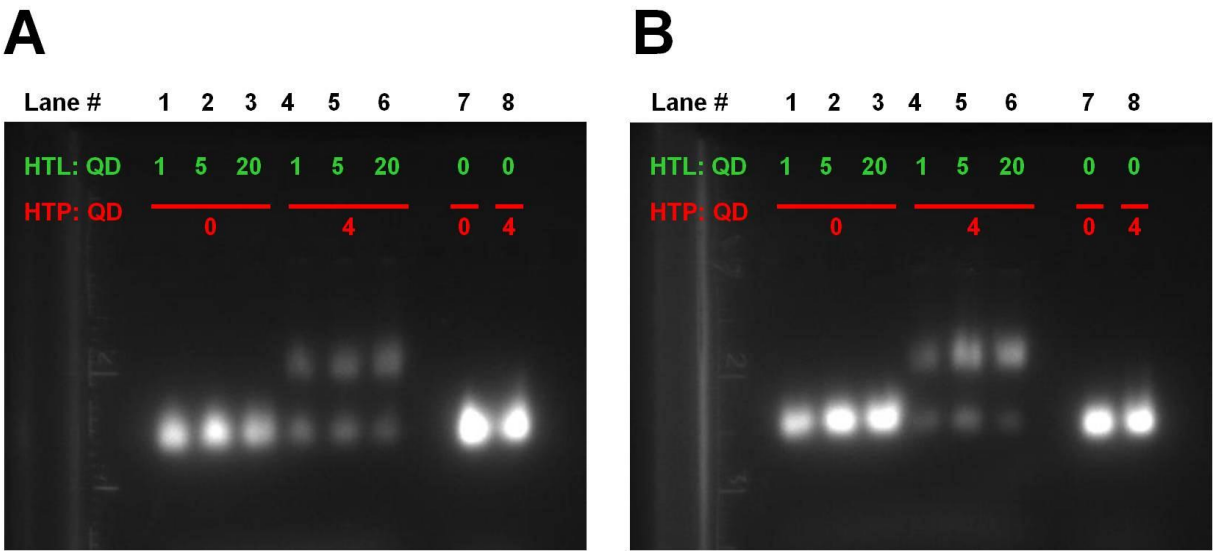

Figure 4.8. Gel electrophoresis mobility assay assessing quantum dot-HaloTag ligand (QD-HTL) conjugates of various ligand lengths and ligand densities. (A) QD-HTL conjugates with 700 MW HaloTag ligands. (B) QD-HTL conjugates with 2500 MW HaloTag ligands. QDs were reacted with HTLs at the HTL:QD molar ratio indicated in green. Resulting QD-HTLs were subsequently incubated with HaloTag protein at the HTP:QD molar ratio indicated in red.

Multidentate polymer coated QDs exhibited reasonably little nonspecific binding when incubated with less than 5 fold excess HTP for 30 minutes at RT. Nonetheless, Figures 4.7 and 4.8 still demonstrate that a small amount of nonspecific binding is always present. Due to the negative zeta potential of the QDs, we found that nonspecific binding became increasingly significant when incubated with larger amounts of HTP, especially at prolonged time periods or at elevated temperatures. In addition, nonspecific binding of the QD-HTL conjugates to cell lysate was nontrivial. Because this nonspecific binding could cause potential problems in cellular studies, we decided to investigate the effect of incorporating small molecular weight PEG chains into the surface coating. For studies involving pegylated QD-HTLs, the longer 2500 MW ligand was used to allow greater flexibility in the length of PEG chain that can be grafted on the QD-HTL surface.

Pegylation of Quantum Dot-HaloTag Ligand Conjugates

Polyethylene glycol is very widely used in biomedical applications to reduce the nonspecific binding of nanoparticles, medical implants, and drug delivery vehicles, etc. [151, 152]. As such, linear amine-terminated PEGs of three different sizes, 370, 1000, and 2000 MW were grafted onto QD-HTLs and investigated for their ability to reduce nonspecific binding while still providing adequate binding capacity. In these studies, amine-terminated PEGs were conjugated to the carboxyl groups of the multidentate polymer coating using carbodiimide chemistry. 1-ethyl-3-(3-dimethylaminopropyl) carbodiimide (commonly known as EDC) was used as the carbodiimide of choice because of its solubility in water. Unfortunately, initial attempts to with PEG using EDC resulted in QD instability and precipitation out of solution in as little as 24 hours.

To optimize the pegylation procedure, parameters affecting the stability of the PEG-QD conjugates were investigated. The amount of EDC (1,000 to 100,000 molar excess) and PEG (5 to 200,000 molar excess) used to pegylate the QD was varied, and the stability of the QD was monitored for at least one week. We also sought to determine whether the MES buffer used for the pegylation reaction had any effect on the stability of the QDs over time when compared to PBS buffer.

We found that excessive EDC was responsible for the instability of the QDs [153]. When the amount of EDC added exceeded the amount of PEG added, QDs would precipitate out of solution over time. Conversely, QDs would remain stable for several months if the amount of EDC was less than the amount of PEG added regardless of the length or amount of PEG used. We found that a molar ratio of 0.75:1 EDC to PEG was ideal for producing stable pegylated QDs, and found this value to be fairly consistent with previous reports [154]. Moreover, both pegylated and nonpegylated multidentate polymer QDs were able to remain stable in MES and PBS buffers for several months.

Activation of carboxylic acids with EDC occurs most efficiently in the pH 4.5-7.2 range. As a result, EDC reactions are typically carried out in MES buffer (pH 6), although reactions in buffers of higher pH such as PBS or borate can also be performed [72, 154]. We tested the pegylation of our multidentate polymer QDs in both MES and PBS buffers and found that reaction in PBS produced pegylated particles of much greater size distribution. When resolved using agarose gel electrophoresis, QDs pegylated in PBS produced broad smear-like bands whereas QDs pegylated in MES produced more compact bands indicating a greater degree of monodispersity (Figure 4.9). Henceforth, all

pegylation reactions were carried out in MES, and pegylated QDs were subsequently dialyzed into PBS prior to use in biological applications.

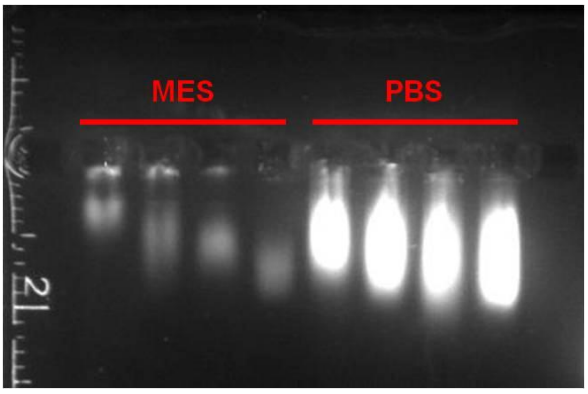

Figure 4.9. Agarose gel comparing QDs pegylated in MES buffer (pH 6) versus PBS buffer (pH 7.4).

For each length of PEG, we sought to determine (a), the amount of PEG needed to fully coat the QD surface under the given reaction conditions and (b), whether the PEG coating would be sufficient for fully neutralizing the surface. As shown in Figure 4.10, both 2000 and 1000 MW PEGs were able to fully neutralize the surface, preventing the QD from migrating out of the well during gel electrophoresis. Roughly 5000 excess of 2000 MW PEG or 10,000 excess of 1000 MW PEG was required to fully coat the QD surface. In contrast, 370 MW PEGs were unable to prevent electrophoretic movement out of wells, even when coated at 200,000 molar excess. This observation is consistent with results reported by Bentzen and coworkers, who likewise reported electrophoretic movement out of wells for amphiphilic polymer coated QDs fully coated with 350 MW PEGs [154].

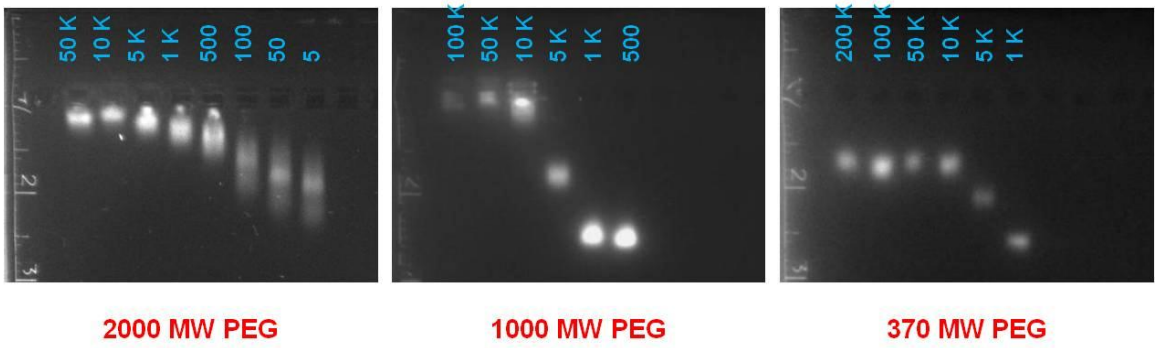

Figure 4.10. Gel electrophoresis mobility assay examining QDs coated with different PEG densities and molecular weights. QDs were reacted with various molar excesses of 370, 1000, and 2000 MW PEG, as indicated in blue. For example, "5 K" indicates that QDs were incubated with PEG at a 5000:1 PEG:QD molar incubation ratio.

Preliminary studies indicated that 2000 MW was the maximum PEG length that could be grafted onto the QD surface while still allowing QD-HTL conjugates composed of 2500 MW HaloTag Ligands to specifically bind to purified HaloTag protein. Figure 4.11 shows the results of an electrophoresis assay that was performed to simultaneously assess the effects of PEG coverage and HaloTag ligand density on QD-HTL binding capacity. Varying amounts of 2000 MW PEG ranging from 5,000 to 50,000 excess were used to coat QD-HTLs containing three different surface ligand densities (50:1, 5:1, and 1:1 HTL:QD molar incubation ratios). As shown on the far right-hand side of Figure 4.10, the controls are comprised of pegylated QDs without any ligands on their surface. In the presence of HaloTag protein, pegylated QDs without ligand exhibit minimal nonspecific binding (Lanes #22 – 24).

For pegylated QD-HTL constructs that have been coated with an excess of 5,000x or 10,000x PEG, a distinctive band shift can be seen in the presence of HaloTag protein, regardless of the ligand density (Lanes #5, 6, 11, 12, 17, 18). This shift, however, cannot

be seen for pegylated QD-HTL constructs that have been coated with 50,000x PEG. One important conclusion, therefore, is that the pegylated QD-HTL can lose its ability to bind target protein if the amount of PEG coverage on the surface is too great. One promising observation is that QD-HTLs of low ligand density, down to 1:1 HTL:QD, can still bind their target when pegylated, provided that the degree of pegylation is not too excessive. These studies indicate that the surface chemistry of the quantum dot plays a very important role in influencing the binding interaction between the HaloTag ligand and the HaloTag protein.

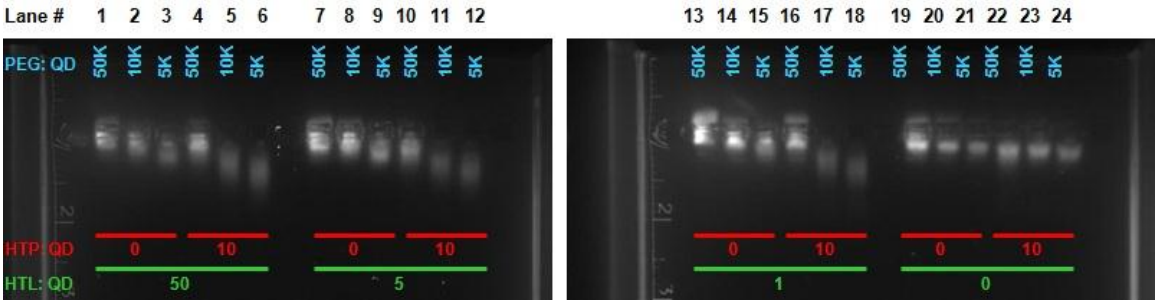

Figure 4.11. Gel electrophoresis mobility assay assessing pegylated quantum dot-HaloTag ligand (QD-HTL) conjugates of various ligand densities and amounts of 2000 MW PEG. QDs were reacted with 2500 MW HaloTag ligands at the HTL:QD molar ratio indicated in green. QDs were subsequently coated with 2000 MW PEG at the PEG:QD molar ratio indicated in blue. The final PEG-QD-HTL conjugates were incubated with HaloTag protein at the HTP:QD molar ratio indicated in red.

Pegylated QD-HTLs fully coated with 1000 MW PEG behave in much the same way as pegylated QD-HTLs fully coated with 2000 MW PEG. As shown in Figure 4.12, QD-HTLs coated with 10,000 excess 1000 MW PEG remain capable of binding HTP, while control pegylated QDs show minimal nonspecific binding to HTP. Pegylated QD-HTLs fully coated with either 1000 or 2000 MW PEG also remain resistant to

nonspecific binding when added to U2OS cell lysate (Figure 4.13). In contrast, we found that pegylated QDs and pegylated QD-HTLs fully coated with 30,000x 370 MW PEG still exhibit nonspecific binding when respectively added to HTP and cell lysate (data not shown).

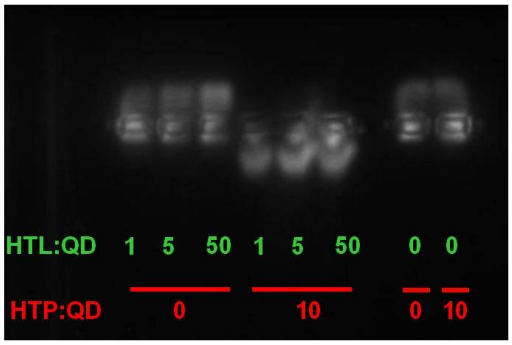

Figure 4.12. Gel electrophoresis mobility assay assessing HaloTag binding ability of quantum dot-HaloTag ligand (QD-HTL) conjugates of various ligand densities coated with 10,000 excess 1000 MW PEG. QDs were reacted with 2500 MW HaloTag ligands at the HTL:QD molar ratio indicated in green. Upon coating with 1000 MW PEG, the resulting PEG-QD-HTL conjugates were incubated with HaloTag protein at the HTP:QD molar ratio indicated in red.

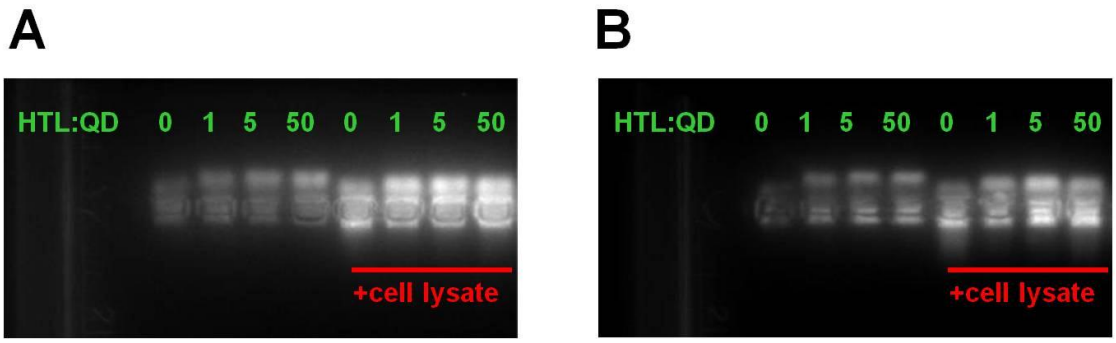

Figure 4.13. Agarose gel image depicting nonspecific binding of PEG-QD-HTL conjugates to cell lysate. (a) QD-HTL conjugates coated with 5000 excess of 2000 MW PEG and (b) QD-HTL conjugates coated with 10,000 excess of 1000 MW PEG are incubated either in PBS or cell lysate for 1 hour.

In summary, 1000 MW PEG and 2000 MW PEG coatings were able to fully abolish electrophoretic mobility of QDs during gel electrophoresis, whereas QDs coated with 370 MW PEG always retained their ability to migrate out of wells. Accordingly, 1000 MW PEG and 2000 MW PEG coatings were more effective at reducing nonspecific binding than 370 MW PEG coatings.

Characterization of Quantum Dot-HaloTag Ligand Conjugates

Multidentate polymer QD-HTL conjugates remain exceptionally compact, even after surface modification with PEG. Due to the limitless number of possible surface variations in the number of ligands, length of ligand, degree of PEG coating, and length of PEG, we sought to focus our characterization studies on QDs functionalized with 2500 MW ligand and coated with 10,000 excess of 1000 MW PEG. This combination was found to be ideal for cell staining, as later discussed in Chapter 5. As shown in Figure 4.14, a multidentate polymer coated CdSe(CdS/CdZnS/ZnS) QD with 629 nm emission that is originally 7.5 nm in hydrodynamic diameter (i) becomes an average of 8.5 nm in hydrodynamic diameter after surface modification with two-fold excess 2500 molecular weight HTL (ii). After complete coating with 10,000 excess 1000 MW PEG, the final PEG-QD-HTL conjugate reaches an average hydrodynamic diameter of 12 nm (iii), which is significantly smaller than conventional pegylated QDs, which typically range from 25-35 nm [155]. Modification of QDs with HTL and PEG did not result in any appreciable changes to the absorption or emission spectra of the QDs.

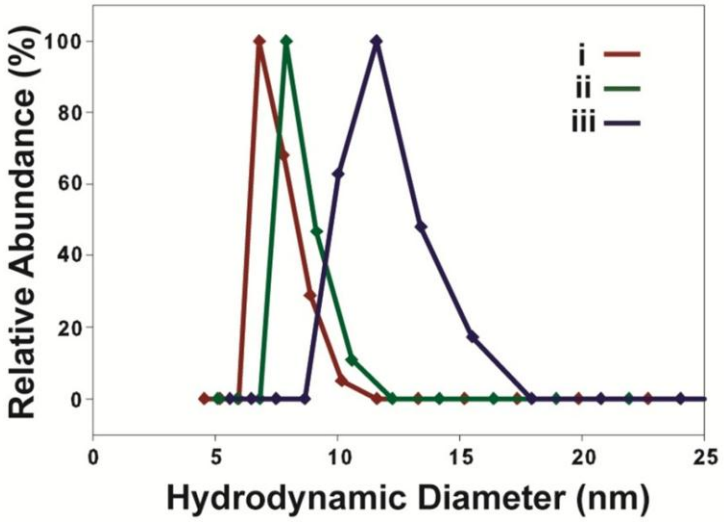

Figure 4.14. Hydrodynamic size of QD-HTLs before and after HaloTag ligand conjugation and PEG modification. Dynamic light scattering data of multidentate polymer coated QDs (i, red); multidentate polymer coated QDs reacted with 2-fold molar excess 2500 MW HTL (ii, green); multidentate polymer coated QDs reacted with 2-fold excess 2500 MW HTL and 10,000 excess 1000 MW PEG (iii, blue), in aqueous solution.

To estimate the number of PEGs on the surface of the quantum dot, we coated the multidentate polymer with PEG containing a terminal fluorescein dye. This strategy has been utilized by multiple researchers to quantitate the number of PEGs on nanoparticle surfaces [152, 156, 157]. Although this strategy is not entirely accurate because the fluorescein group adds a small amount of extra molecular weight (300 Da) to the PEG, it nonetheless provides a good estimate of the number of PEGs on the QD surface. A similar alternative strategy for quantifying the number of PEG molecules is to coat the nanoparticle with PEG containing a specific terminal functional group such as a thiol or amine. A fluorometric or colorimetric agent such as fluorescamine or Ellman's reagent can then be used to determine the number of functional group, and hence, the number of PEG molecules on the nanoparticle surface [158]. While eliminating problems with the

added molecular weight of the dye, this method is more difficult in our case due to the presence of thiols and amines in the multidentate polymer coating the QD. Nuclear magnetic resonance (NMR) can also be used to detect the ethylene protons on the nanoparticle surface, but this method is not as quantitative and requires large quantities of nanoparticles for analysis [152, 159].

In our strategy, red CdSe(CdS/CdZnS/ZnS) QDs were reacted with 10,000 excess of 1000 MW FITC-PEG (green) and 7,500 M EDC and subjected to extensive dialysis. An identical sample of QDs and PEG was prepared without EDC and purified alongside the FITC-PEG-QD as a control to ensure complete removal of FITC-PEG. For determining the number of FITC-PEG molecules, absorbance measurements are preferred over fluorescence intensity measurements due to possible effects of self-quenching when fluorescent molecules are present in high concentrations [160]. Figure 4.15 shows the UV-Vis spectrum of these samples after purification. The presence of a large absorbance peak at 490 nm indicates that FITC-PEG was indeed successfully conjugated to the QD surface (green). A comparison of the spectra of the control sample (blue) with a sample of multidentate polymer QDs (red) indicates that FITC-PEG was completely removed during purification. By using Beer's law and the extinction coefficient of FITC-PEG, the average number of 1000 MW PEGs on the QD surface was found to be approximately 500 molecules.

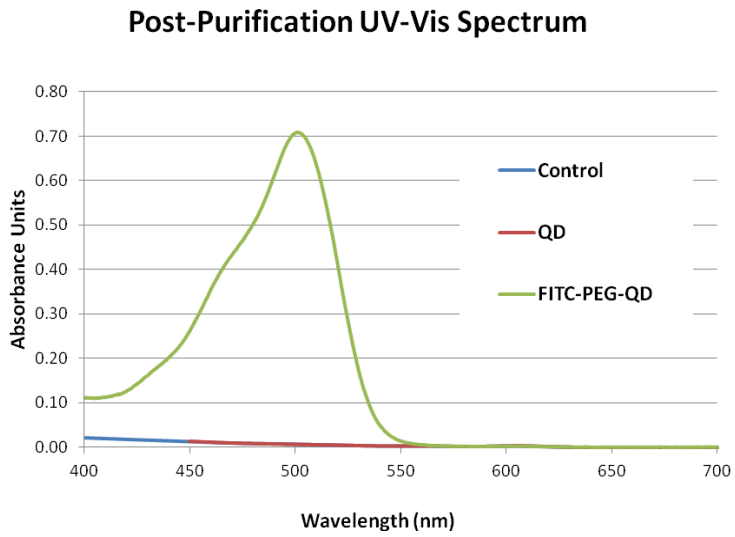

Figure 4.15. Estimation of the number of PEG molecules on the QD surface using FITC dye absorbance. QDs are reacted with 10,000 excess 1000 MW PEG containing a terminal FITC dye. Upon thorough purification of unreacted FITC-PEGs, the absorption spectrum of the FITC-PEG-QD conjugates (green) is compared with the absorption spectrum of QDs alone (red). The control (blue) contains a sample of QDs and 10,000 excess FITC-PEG without EDC that has been subjected to the same purification as the FITC-PEG-QDs. See text for details.

It is important to characterize the number of ligands on the QD surface to ensure that an increase in the number of HTLs reacted with QD actually results in an increase in valency on the nanoparticle surface. To estimate the number of ligands on the QD surface, we utilized a fluorescamine assay to measure the number of prior amines on the QD surface prior to and after to reaction with nitrophenol carbonate HTLs. Fluorescamine is a nonfluorescent compound that reacts with primary amines to form a highly fluorescent compound that emits at 470 nm [161]. One major advantage of using fluorescamine over absorbance based detection methods is that purification of excess fluorescamine is unnecessary due to the nonfluorescent nature of unreacted fluorescamine. Indeed, complete purification of unreacted dyes is extremely challenging

and artifacts can arise in absorbance data if purification is not consistently uniform across multiple samples. However, with all fluorescence based assays, special care should be taken to avoid self-quenching at high dye concentrations and to prevent photobleaching by working in the dark. In addition, special care must be taken when designing the experiment to account for possible fluorescence resonance energy transfer (FRET) effects between the QD and the fluorescent dye.

For FRET to occur, three conditions must be satisfied. First, the donor and acceptor molecules must be in close proximity to each other, usually 1 to 10 nm apart. Second, the donor's fluorescence emission spectrum must overlap with the acceptor's absorption spectrum. One basic implication of this is that the donor must be at higher energy than the acceptor. Finally, the transition dipole orientations of the donor and acceptor must be approximately parallel [162]. Because fluorescamine's emission at 470 nm overlaps with the QD's broadband absorption spectrum, fluorescamine could potentially serve as a FRET donor to a QD acceptor in our experiment. However, studies have shown that in general, fluorescence resonance energy does not transfer from a donor dye to an acceptor QD due to the fast radiative decay of the dye and the much longer exciton lifetime of the QD [163]. We tested this by adding increasing amounts of fluorescamine to a sample of QDs to see if there were any increases in QD fluorescence intensity, and found no evidence of FRET between the dye and QD.

To perform the assay, fluorescamine was first added to a standard of glycine molecules to determine the linear dynamic range for reaction with primary amines. The dynamic range was found to be linear for amine concentrations ranging from 250 nM to 10 μM, similar to previously reported results (Figure 4.16, left) [53]. Fluorescamine was

then added to multidentate polymer coated QD-HTL conjugates that had been reacted with 0, 5, 10, and 20 fold molar excess HTL.

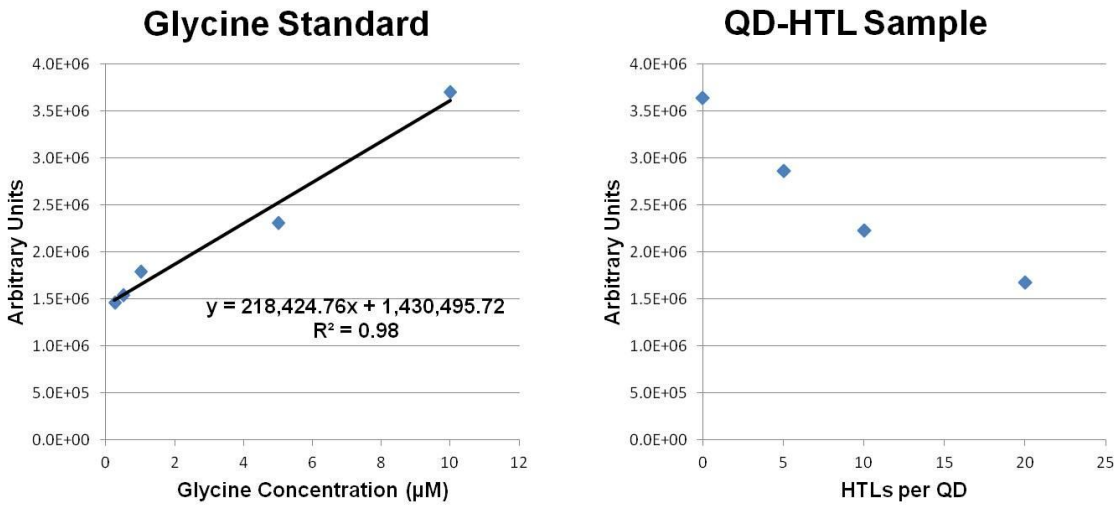

Figure 4.16. Estimation of the number of HaloTag ligands on the QD surface using a fluorescamine assay. A series of glycine standards are first reacted with fluorescamine to determine the linear dynamic range for detection of primary amines (left). Immediately afterward, QD-HTL conjugates with are reacted with fluorescamine to determine the number of free amines on the QD-HTL surface (right). The number of HTLs on the QD surface can be determined by subtracting the number of free amines on the QD surface before and after reaction with HTL. See text for details.

The right hand side of Figure 4.16 shows the results of a fluorescamine assay for QD samples assayed at 600 nM concentration. As expected, QDs without HTL have the highest fluorescamine signal intensity, while signal intensity progressively decreases for QD-HTLs containing increasing amounts of ligand on the surface. Since the nitrophenol carbonate HTL reacts with primary amines on the multidentate polymer QD coating, QD-HTLs with higher ligand content have fewer amines available for reaction with fluorescamine. As measured by the fluorescamine assay, red multidentate polymer coated

CdSe(CdS/CdZnS/ZnS) QDs that are 7.5 nm in hydrodynamic diameter have roughly 16-17 amines on the surface prior to ligand conjugation.

Table 4.2 and Table 4.3 list the average number of ligands empirically determined or interpolated for QD-HTL conjugates of various ligand densities. The results of this assay indicate that the number of ligands on the QD surface is fairly consistent with the number of ligands incubated with QD during reaction. For example, QDs reacted with HTL at a 1:1 molar ratio have roughly 1 ligand on the surface on average.

Table 4.2. Estimation of the number of HaloTag ligands on the QD surface using a fluorescamine assay.

HTL:QD molar ratio	Signal Intensity	Total amine concentration (μM)	Free amines per QD	Empirical # of HTLs per QD
0	3.64E+06	10.10	16.8	0.0
5	2.86E+06	6.55	10.9	5.9
10	2.23E+06	3.65	6.1	10.7
20	1.68E+06	1.14	1.9	14.9

Table 4.3. Interpolated data from a fluorescamine assay for estimating the number of surface HaloTag ligands for QD-HTLs with low ligand density.

HTL:QD molar ratio	Empirical # of HTLs per QD
0.5	0.546
1	1.092
2	2.184

This data is helpful for determining an appropriate molar reaction ratio for producing monovalent QD-HTLs for single-molecule imaging. Since the number of

ligands present on the QD surface is governed by a Poisson distribution, HTLs should be incubated with QDs at a HTL:QD ratio much less than 1 in order to produce monovalent QDs. At low ratios such as 0.5:1 HTL:QDs or smaller, most QDs will only contain 1 or 0 ligands on their surface, with a very low probability of QDs containing 2 or more ligands on their surface. In conclusion, the results of this fluorescamine assay indicate that HTLs can indeed be reacted with QDs at a well controlled stoichiometries required for live cell imaging.

4.4 Conclusions

We have developed a new strategy for HaloTagging of QDs based on the use of size-minimized multidentate polymer coated QDs. We have optimized synthesis and purification procedures for these QD-HTLs and further characterized their binding to purified HTP. These QD-HTLs demonstrate efficient binding to purified HTP when elongated HaloTag ligands of 700 and 2500 MW are utilized. Furthermore, these QD-HTLs are able to bind HTP even at low ligand densities, potentially down to 1 HTL per QD. These QD-HTLs retain their ability to bind HTP specifically even when coated with PEG, provided that the degree of pegylation is not too excessive. In conclusion, our studies show that QD surface chemistry plays an important role in the interaction between the QD-HTL and the HTP, and that QD binding to target protein can be enhanced by carefully tuning the QD surface parameters.

CHAPTER 5

SPECIFIC AND NONSPECIFIC BINDING OF QUANTUM DOT-HALOTAG LIGAND CONJUGATES TO CELLULAR SURFACES

5.1 Introduction

In order to be useful for cellular imaging applications, quantum dot probes must be able stain desired proteins of interest both specifically and efficiently. Especially for single-molecule imaging, nonspecific binding must be reduced as much as possible to prevent tracking of unintended proteins. Nonetheless, eliminating nonspecific binding has always been a fundamental challenge for all types of colloids due to their high surface energy and large available surface area for binding.

In Chapter 4, we have shown that Quantum Dot-HaloTag ligand conjugates are able to specifically bind purified HaloTag proteins in solution. While many trends are anticipated to be similar to those observed with purified HaloTag proteins, binding to cellular HaloTag proteins is more complex due to the heterogeneity of cellular surfaces. Binding interactions are also expected to be more sterically hindered when constrained to a 2-D surface rather than a 3-D volume.

In this chapter, we seek to identify the key parameters that govern the delicate balance between specific and nonspecific binding in the QD-HaloTag cellular system, making the appropriate modifications necessary to minimize the latter.

5.2 Materials and Methods

Cell Culture and Staining

U2OS cells stably expressing HaloTag protein fused to the extracellular domain of β1 integrin ("U2OS-ECS1-HTP") were a generous gift from Promega Corporation. Details of their cloning and expression are extensively described by Svendsen et al. [137]. U2OS cells (ATCC #HTB-96) were maintained in McCoy's 5A media supplemented with 10% FBS at 37 ^{0}C and 5% CO_2. Stable U2OS-ECS1-HTP cells were maintained in McCoy's 5A media supplemented with 10% FBS and 500 mg/ml Geneticin Sulfate at 37 ^{0}C and 5% CO_2.

For cell labeling, cells were plated on an 8-well Lab-Tek II chamber cover glass (Nunc) and allowed to grow to ~50% confluency for approximately 24 hrs. Prior to staining, cells were washed twice with imaging media consisting of phenol red-free McCoy's 5A media supplemented with 20 mM HEPES. Cells were then incubated with TMR ligand or QD-HTL conjugates in imaging media for 15 min at 37 ^{0}C and 5% CO_2. Afterward, cells were rinsed three times in imaging media at room temperature followed by a 15 minute incubation at 37 ^{0}C and 5% CO_2, in accordance with the manufacturer's recommended protocol [164]. Finally, the incubation media was replaced with fresh imaging media prior to fluorescence imaging.

For studies examining the effect of ligand density on staining specificity, PEG-QD-HTLs were applied to U2OS-ECS1-HTP cells (denoted as HTP+) and U2OS cells (denoted as HTP-) at a series of concentrations from 20 to 200 nM. For each ligand density, the concentration that resulted in greatest signal contrast between HTP+ and HTP- cells under the particular imaging conditions was selected for comparison. This

methodology accounts for the fact that QDs of lower ligand density require higher staining concentrations than QDs of higher ligand density to produce similar contrast.

For studies examining the effect of PEG molecular weight on staining specificity, PEG-QD-HTLs were likewise applied to U2OS-ECS1-HTP and U2OS cells at a series of concentrations from 20 to 250 nM. When comparing PEG coatings of different molecular weight, the total mass weight of PEG used to completely coat the QD was kept roughly constant (i.e. molecular weight (g/mol) x molar excess = constant). As such, QD-HTLs were either coated with (a) 5,000 excess 2000 MW PEG (b) 10,000 excess 1000 MW PEG or (c) 28,000 excess 370 MW PEG. This methodology takes into consideration the fact that PEG polymers of longer lengths require fewer numbers to completely coat the QD surface.

Live Cell Fluorescence Imaging

Cells were imaged on an Olympus IX71 epifluorescence inverted microscope equipped with a Hamamatsu C9100 EM-CCD camera using a 20x objective. All samples were illuminated using a mercury arc lamp. The following filters were used for visualization of Promega TMR ligand (555 excitation/585 emission): 535/30 excitation, 572 long pass emission, 565 dichroic. The following filters were used for visualization of QDs (629 emission): 330-385 excitation, 625/20 emission, 500 dichroic. Images were collected using Hamamatsu Wasabi software and analyzed with NIH ImageJ.

5.3 Results and Discussion

TMR Ligand Staining of Cellular Surface HaloTag Protein

Figure 5.1a shows a general schematic of the HaloTag expressing cells used throughout our studies. This cell line, known as "U2OS-ECS1-HTP", expresses β1 integrins with an extracellular domain that has been truncated and fused to the HaloTag protein. We selected this system because it has been previously used, thoroughly studied and well-characterized in the literature. Unlike many other surface display systems, the β1 integrin-HTP fusion has been shown to retain much of the activity of the original integrin. Svendsen et al. has shown that the β1 integrin-HTP fusion is localized, trafficked, and internalized in the same manner as native integrin, even undergoing the correct post-translational modifications [137]. β1 integrin plays critical roles in cell adhesion, invasion and migration [165, 166], and single-molecule studies could potentially uncover new insight on β1 integrin dynamics. Staining with TMR ligand, a commercially available fluorescent dye-HaloTag ligand conjugate from Promega, confirms that the β1 integrin-HTP is highly expressed and that the HaloTag protein remains functional in U2OS-ECS1-HTP cells (Figure 5.1b, c).

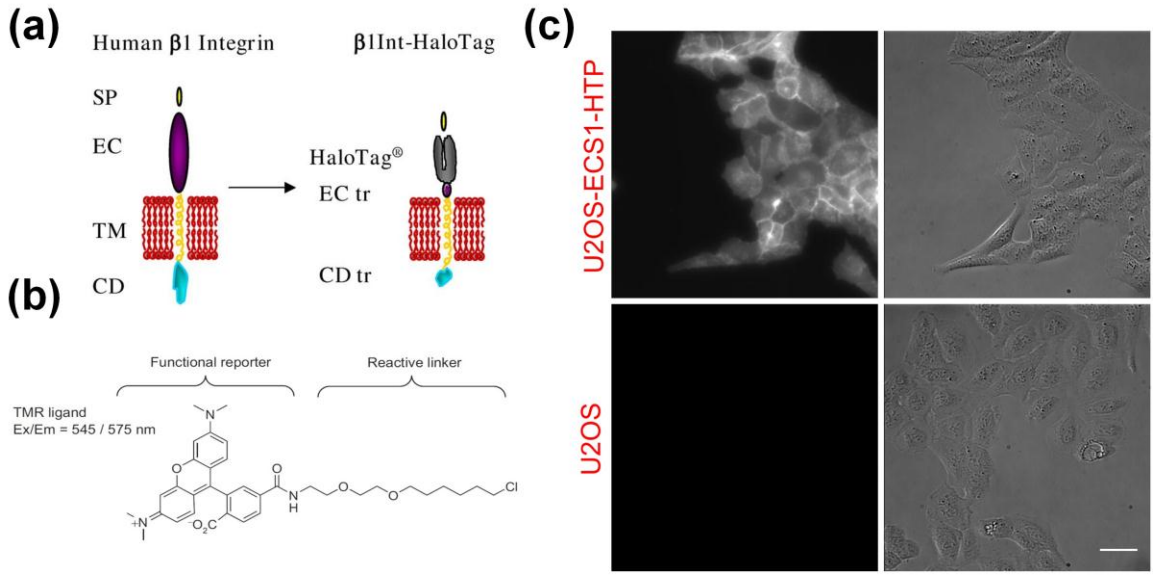

Figure 5.1. TMR staining of U2OS cells expressing a human β1 integrin-HaloTag fusion protein. Native human β1 integrin contains a cytoplasmic domain (CD), transmembrane domain (TM), extracellular domain (EC), and signal peptide (SP). U2OS-ECS1-HTP cells express a modified form of the β1 integrin, with the HaloTag protein fused to the truncated extracellular domain. (b) Chemical structure of TMR ligand. (c) Positive staining of U2OS-ECS1-HTP cells with 1 µM TMR ligand concentration. Images are shown at a dynamic range of 16000 units. Scale bar = 40 µm. 8a is adapted from [137]; 8b is adapted from [40].

Effect of Various Staining Conditions on HaloTag-Mediated Cell Staining

HaloTag-mediated staining differs from traditional methods of cellular staining because of the enzymatic nature of the HaloTag protein. While the behavior of traditional labeling strategies is typically described by receptor-ligand kinetic equations, the HaloTag protein-HaloTag ligand reaction is governed by Michaelis-Menten kinetics.

Enzymes typically require relatively high substrate concentrations for efficient reaction, and enzymatic activity is susceptible to changes in pH and temperature. In order to optimize the QD-HTL staining procedure, we first sought to qualitatively evaluate the

efficiency of the HaloTag labeling under various staining conditions, including different staining concentrations and temperatures, using the TMR ligand.

Staining Concentration

The Promega manufacturer's protocol recommends staining at 5 μM TMR ligand concentration [164]. To see if a high substrate concentration was necessary for efficient enzymatic activity, we tested different staining concentrations ranging from 1 nM to 5 μM. For all staining concentrations, the TMR ligand was able to specifically stain HTP expressing cells with respect to native cells (Figure 5.2). The fact that specific staining could be achieved at single-digit nanomolar concentrations served as promising evidence that HaloTag technology can be successfully applied to single-molecule tracking studies. Indeed, single-molecule imaging of an intracellular HaloTagged cAMP receptor using TMR ligand has already been reported in the literature [167].

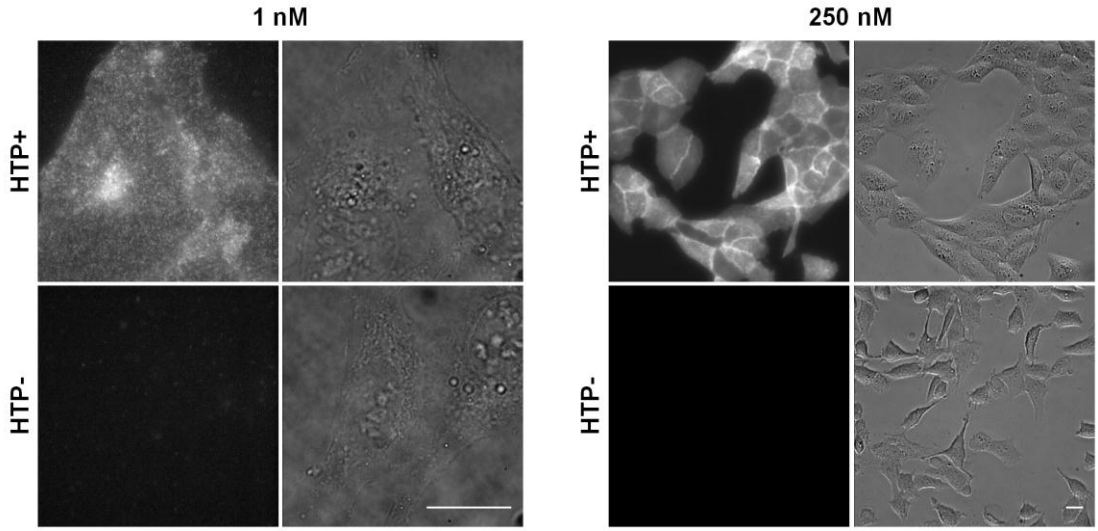

Figure 5.2. Staining of HaloTag protein expressing (HTP+) cells and control (HTP-) cells at different TMR ligand concentrations. TMR staining at 1 nM concentration (left) is shown at 160x magnification and dynamic range of 500 units. Staining at 250 nM concentration (right) is shown at 32x magnification at a higher dynamic range of 8000 units to avoid signal saturation. Scale bar = 20 μm.

Temperature

Cells are often kept on ice or at 4 ^{0}C as a common method of preventing endocytosis of probes bound to cell surface receptors [168]. Studies have shown that shown that cellular metabolic processes, especially membrane internalization and receptor trafficking, are drastically slowed at lower temperatures [169, 170]. Hence, fluorescence staining of cell surface proteins is often performed at 4 ^{0}C to confine fluorescence signal to the perimeter of the cell. Staining at 4 ^{0}C also reduces endocytosis of nonspecifically bound probes. Once probes are internalized into vesicles, they cannot be removed. By confining nonspecifically bound probes to the cellular membrane surface where they can be washed away, lowered staining temperature may help to reduce nonspecific binding.

However, lowered temperature may also adversely affect enzymatic activity. The effect of temperature on reaction rates is governed by the Arrhenius equation,

$$k = Ae^{-E_a/RT} \qquad \text{Equation 5.1}$$

where k is the reaction rate constant, T is the absolute temperature in kelvins, A is a constant, E_a is the activation energy, and R is the universal gas constant, and T is the absolute temperature in kelvins. For enzymes, a general rule of thumb is that a 10 ^{0}C increase in temperature will increase the activity of most enzymes from one to two-fold, until the temperature exceeds the denaturation point of the enzyme [171]. Consequently, we sought to investigate the effect of staining temperature on the HaloTag protein-ligand enzymatic reaction.

We performed cellular staining at both 37 ^{0}C and 4 ^{0}C and found that TMR ligand was able to specifically stain HaloTag protein expressing cells relative to control cells at both temperatures, as shown in Figure 5.3a. As expected, the enzymatic activity of the HaloTag protein was strongly temperature dependent, and the staining intensity of HaloTag protein expressing cells at 37 ^{0}C was over 6 times greater than the staining intensity at 4 ^{0}C (Figure 5.3b). Interestingly, we found that staining with TMR ligand at lowered temperature actually enhanced nonspecific binding to U2OS cells rather than reducing it (Figure 5.3c). We likewise observed a significant increase in nonspecific binding for QD-HTL conjugates at 4 ^{0}C compared to 37 ^{0}C (not shown). Our hypothesis is that lowered temperature reduces the diffusion of nonspecifically bound probes, making it more difficult to remove nonspecifically bound probes by washing. On the other hand, little endocytosis of TMR ligand was observed at 37 ^{0}C over the course of 15 minutes. Because lowered temperature worsened staining contrast between HaloTag

protein expressing cells and control cells, we chose to perform all subsequent staining experiments at 37 ^{0}C.

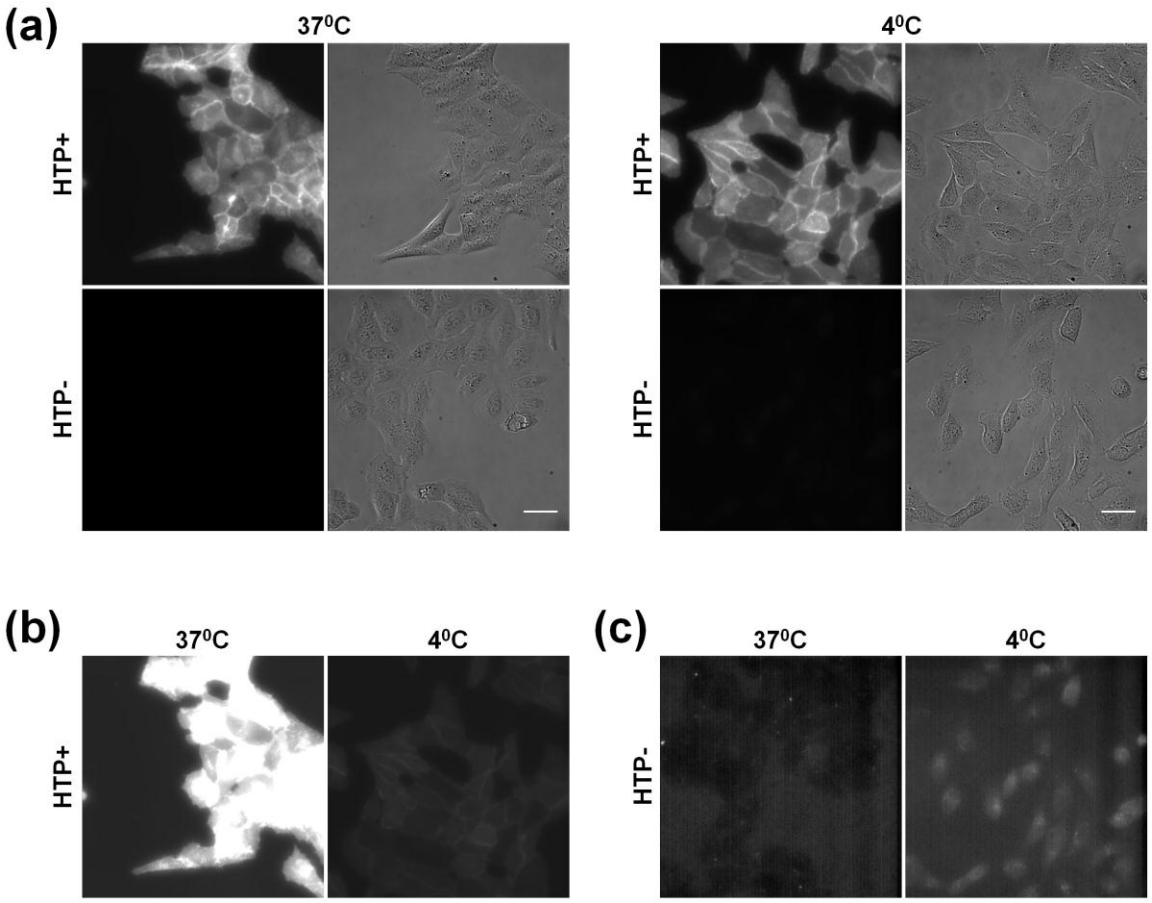

Figure 5.3. Effect of temperature on TMR ligand staining of HaloTag protein expressing (HTP+) cells and control (HTP-) cells. (a) TMR ligand exhibits specific staining to HTP+ cells with respect to control cells at both 37 ^{0}C and 4 ^{0}C. To depict contrast while avoiding signal saturation staining at 37 ^{0}C is shown over a different dynamic range than staining at 4 ^{0}C. (b) Specific staining of HTP+ cells at different temperatures is shown over a constant dynamic range of 6000 units. (c) Nonspecific staining of HTP- cells at different temperatures is shown over a constant dynamic range of 100 units. Scale bar = 40 µm. Lowered temperature results in decreased positive staining to HTP+ cells and increased nonspecific binding to HTP- cells.

pH

Nonspecific binding of QDs to cells has long been a major bottleneck in QD-mediated cellular staining studies due to the high surface energy and large surface area of QDs [21]. As one strategy to prevent nonspecific binding, Dahan and Triller have reported that nonspecific binding of QD-antibody conjugates to cells can be reduced by staining in borate buffer at pH 8.5 supplemented with 215 mM sucrose to provide the proper physiological osmolarity [172, 173]. The slightly elevated pH reduces the reactivity of attached antibodies to nonspecific protein targets. An additional benefit is that QDs typically exhibit excellent stability, reduced aggregation, and enhanced fluorescence in borate buffer.

In spite of the benefits of staining in borate buffer, elevated pH may be especially detrimental to enzymatic activity. Enzymatic activity generally exhibits a bell-shape dependence on temperature, with peak activity at an optimal pH specific to the enzyme [174]. Therefore, we sought to investigate for ourselves whether borate buffer would adversely affect the cellular staining specificity of TMR ligand. Figure 5.4 shows a comparison of cells stained with TMR ligand in borate buffer supplemented with 215 mM sucrose versus standard phenol red-free media. We found that borate buffer was effective in reducing nonspecific binding of TMR ligand to native U2OS cells (denoted HTP-) when compared to staining in cellular media. Borate buffer only slightly reduced specific binding of TMR ligand to U2OS-ECS1-HTP cells (denoted HTP+), resulting in a little decreased fluorescence staining intensity. However, we found that cells were unable to tolerate elevated pH conditions for extended time without changes in morphology, so we chose not to implement this staining strategy in subsequent experiments.

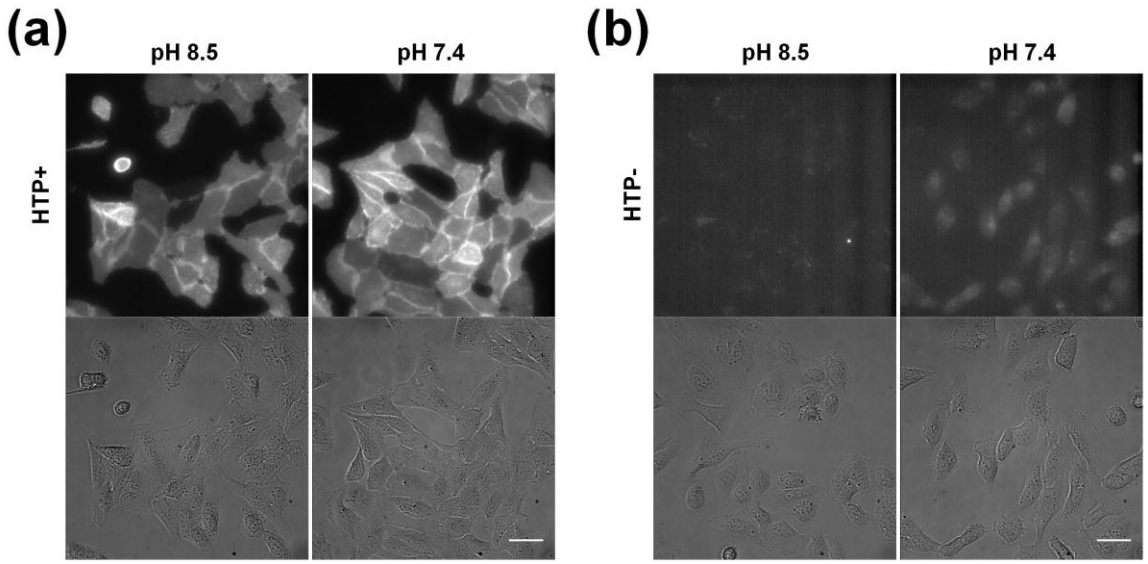

Figure 5.4. Effect of pH on TMR ligand staining of HaloTag protein expressing (HTP+) cells and control (HTP-) cells. Cells are either stained in cellular media (pH 7.4) or borate buffer supplemented with 215 mM sucrose (pH 8.5). Staining is performed at 4 ^{0}C to illustrate the effects of pH on nonspecific binding. (a) Specific staining of HTP+ cells at different pHs is shown over a constant dynamic range of 7000 units. (c) Nonspecific staining of HTP- cells at different pHs is shown over a constant dynamic range of 100 units. Elevated pH results in decreased nonspecific binding to HTP- cells and only slightly decreased specific binding to HTP+ cells. Scale bar = 40 μm.

Through our cell staining experiments with TMR ligand, we were able to optimize the staining conditions needed for QD-HTL staining of HTP expressing cells. Many of the same effects observed for TMR staining were also reflected with QD-HTL staining. For example, lowered temperature was found to exacerbate nonspecific binding of both TMR ligand and pegylated QD-HTLs. In this manner, the TMR staining experiments served as a positive control for our QD-HTL staining experiments. Upon successful optimization of the cell staining conditions, we directed our focus towards optimizing the QD surface parameters needed to achieve specific staining.

Effect of Ligand Density on Cellular Binding Specificity of Quantum Dot-HaloTag Ligand Conjugates

In the only work to date that has been published on quantum dot-HaloTag mediated cell staining, So and coworkers were only able to achieve specific labeling of surface HTP with QD conjugates of high ligand density—ideally, at least 50 HaloTag ligands per QD. They stated that QD conjugates with as many as 5 HTLs per QD displayed virtually no fluorescence in comparison with control QDs lacking HTL [125].

While So's preliminary results seemed discouraging for single-molecule imaging, we sought to systematically investigate for ourselves the dependency of specific binding on valency for two reasons. First, So's work did not examine the effects of different concentrations on specific staining for each valency. Naturally, QDs of lower ligand density would be expected to require higher staining concentrations than QDs of higher ligand density to achieve a similar staining intensity. Thus, it is possible that specific staining could be achieved with monovalent QD-HTLs if higher concentrations are employed. Secondly, So's work did not investigate staining specificity of QD-HTLs with regard to cells lacking HaloTag protein. This is an especially important control for single-molecule imaging, as it is imperative to know that QD-HTLs are not unintentionally tracking random, unwanted proteins.

We started our cell staining studies with PEG-QD-HTL conjugates containing high surface ligand density. Like So, we observed that PEG-QD-HTLs with high ligand density exhibited excellent cellular staining specificity in comparison to control PEG-QDs lacking HTLs. Unfortunately, a major problem was that these PEG-QD-HTLs labeled non-HTP expressing cells just as well as cells expressing HTP, such that staining

was not truly specific. Through systematic optimization of the staining parameters, we discovered QD ligand density to be a key mediator of HaloTag binding specificity.

As shown in Figure 5.5, no specific binding was observed for multivalent PEG-QD-HTLs (20:1, 4:1 HTL:QD molar reaction ratios) regardless of the staining concentration used. As the surface ligand density was decreased, the degree of nonspecific binding likewise decreased, such that staining contrast could finally be detected between HTP+ and control HTP- cells. In fact, specific staining was only observed for very low ligand densities (2:1, 1:1 HTL:QD molar reaction ratios). Our hypothesis is that nonspecifically bound PEG-QD-HTLs of higher valency exhibit much slower dissociation rates than PEG-QD-HTLs of low valency due to an increased number of nonspecific interactions between the HTL and cell surface proteins. These nonspecific interactions are likely mediated between the 6-carbon chain of the HTL and any hydrophobic proteins on the cell surface. Thus, while nonspecifically bound monovalent PEG-QD-HTLs are able to freely dissociate, it becomes increasingly difficult, if not effectively impossible, for nonspecifically bound PEG-QD-HTLs of higher valency to be washed out.

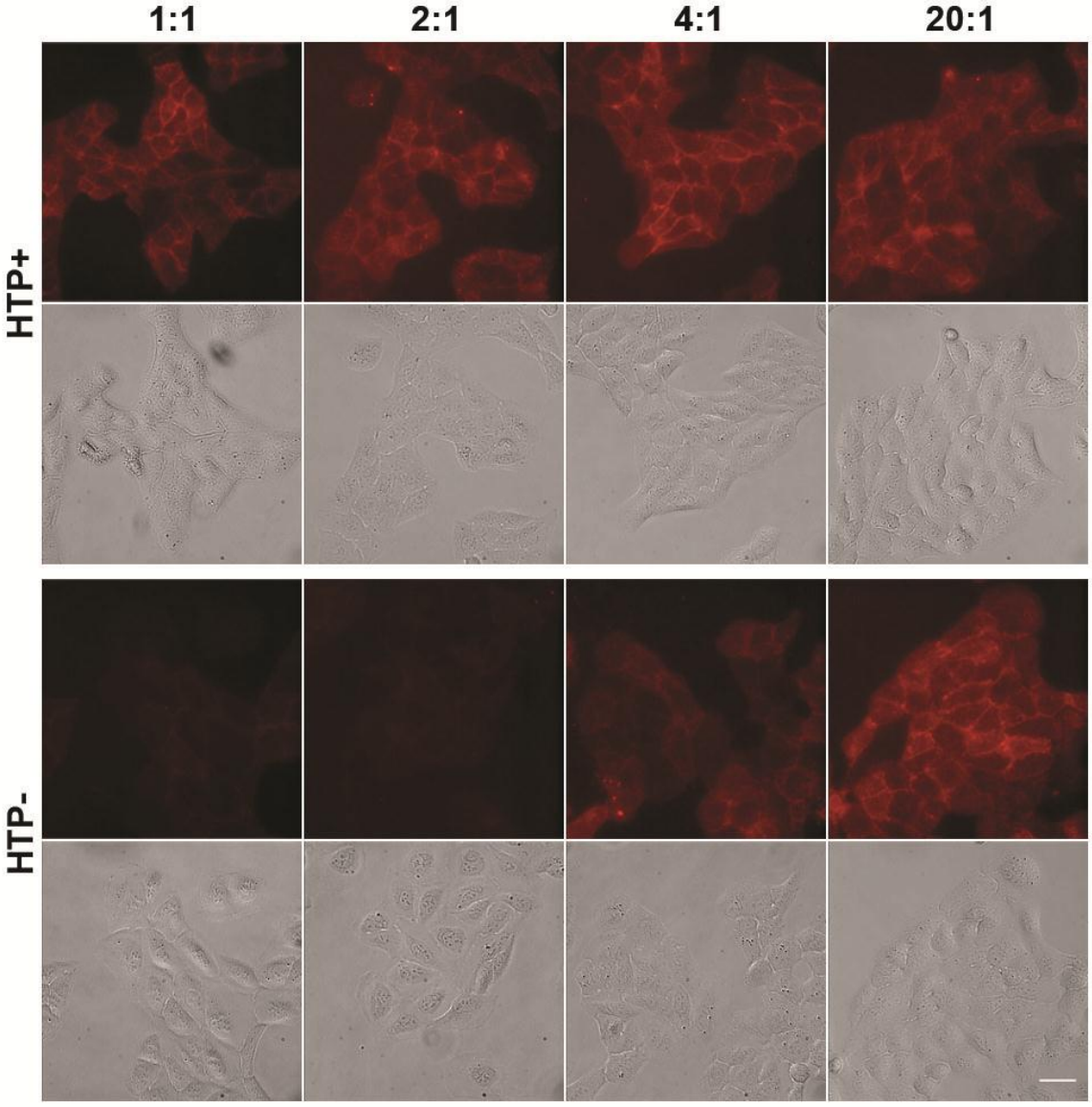

Figure 5.5. Effect of QD surface ligand density on the cell staining specificity of PEG-QD-HTLs. PEG-QD-HTLs with varying ligand densities (reflected by the HTL:QD molar ratio) are incubated with HaloTag protein expressing (HTP+) cells or control (HTP-) cells lacking HaloTag protein. Cells are stained with PEG-QD-HTL at (from left to right) 1:1, 2:1, 4:1, and 20:1 HTL:QD molar reaction ratio. All PEG-QD-HTLs are prepared using 2500 MW HTLs and 10,000 molar excess 1000 MW PEG. Scale bar = 40 μm.

Effect of PEG Length on Cellular Binding Specificity of Quantum Dot-HaloTag Ligand Conjugates

While valency plays a key role in staining specificity, it is not the sole factor. Our studies have shown that the length of PEG used to coat the QD surface is also critically important. As shown in Figure 5.6, we found that longer PEG lengths are more effective at reducing nonspecific binding of QD-HTL conjugates but are also capable of obstructing specific binding. When 2500 MW HTLs were reacted with QDs at a 1:1 molar ratio and coated with 2000 MW PEG, the resulting PEG-QD-HTLs exhibited very little binding to cells, either specific or nonspecific. As the PEG length was shortened to 1000 MW, specific binding was restored. As the PEG length was further decreased to 370 MW, the amount of nonspecific binding increased as the shorter PEG is less effective at preventing nonspecific binding. These results suggest that the HaloTag ligand may become buried in brush-like surface coatings that are too thick. It is also possible that QD-HTLs containing 2500 MW ligands experience more binding steric hindrance when coated with 2000 MW PEG when compared to smaller molecular weight PEGs. Although previous studies showed that QD-HTLs containing 2500 MW ligands are able to bind purified HTP when coated with 2000 MW PEG, (Figure 4.11) they may be unable to bind cellular HTP as effectively since binding interactions are more sterically hindered when constrained to a 2-D surface rather than a 3-D volume. In summary, these results suggest that the optimal size PEG used for coating QD-HTLs should be of an intermediate length.

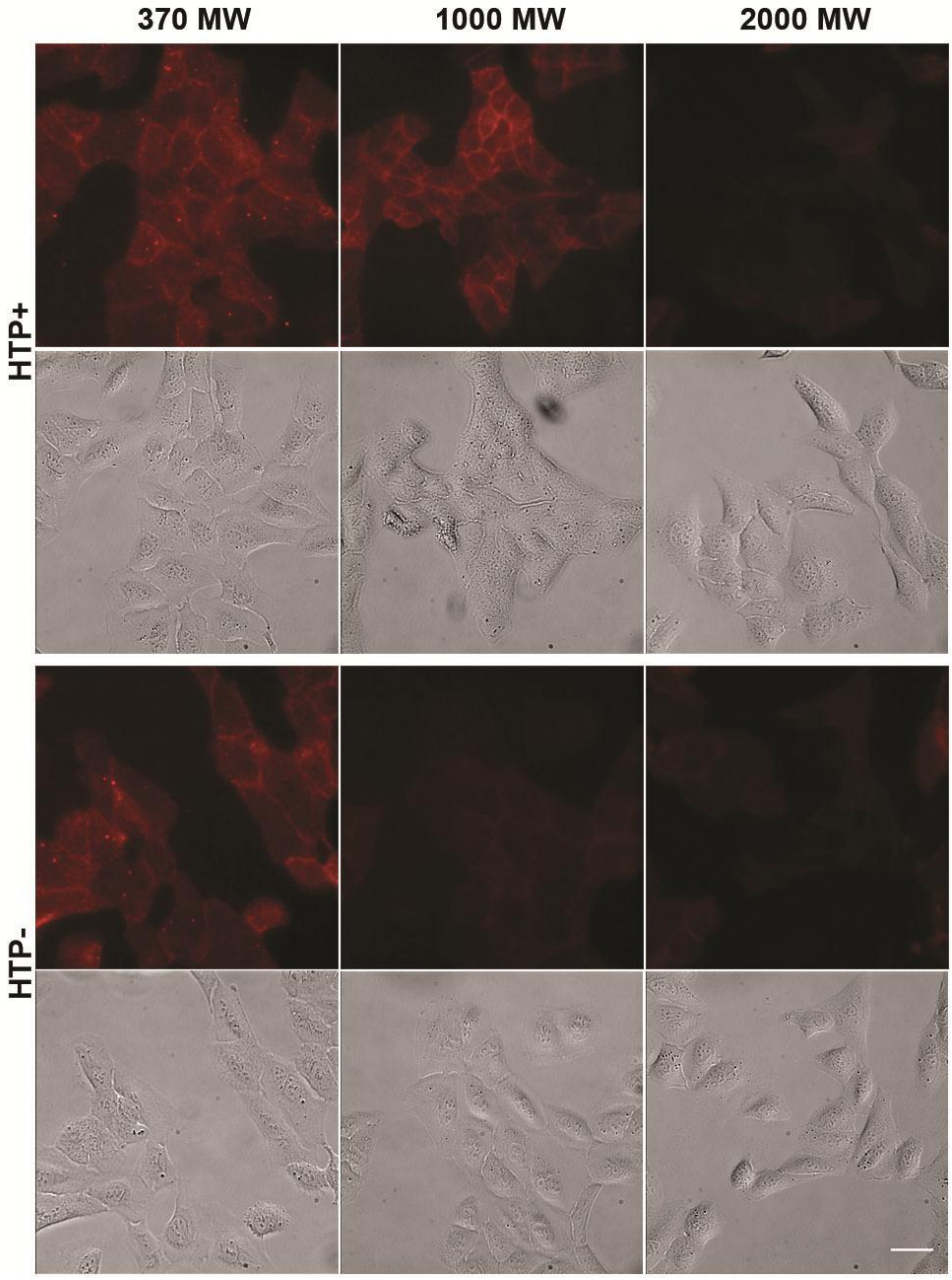

Figure 5.6. Effect of PEG length on the cell staining specificity of PEG-QD-HTLs. PEG-QD-HTLs coated using different PEG lengths are incubated with HaloTag protein expressing (HTP+) cells or control (HTP-) cells lacking HaloTag protein. Cells are stained with (left to right) QD-HTL coated using 28,000 molar excess 370 MW PEG; QD-HTL coated using 10,000 excess 1000 MW PEG; and QD-HTL coated using 5000 excess 2000 MW PEG. All PEG-QD-HTLs are prepared with 2500 MW HTL using a molar reaction ratio of 1:1 HTL:QD. Scale bar = 40 μm.

Staining Specificity of Pegylated Quantum Dot-HaloTag Ligand Conjugates

Together, our results suggested that QD-HTLs coated with 1000 MW PEG containing a low surface ligand valency were ideal for achieving cellular binding specificity. Figure 5.7 shows that these PEG-QD-HTL conjugates were able to successfully stain HTP expressing cells with respect to cells lacking HaloTag protein. Furthermore, pegylated QDs lacking HaloTag ligand exhibited very little nonspecific binding to both HTP expressing cells and native U2OS cells.

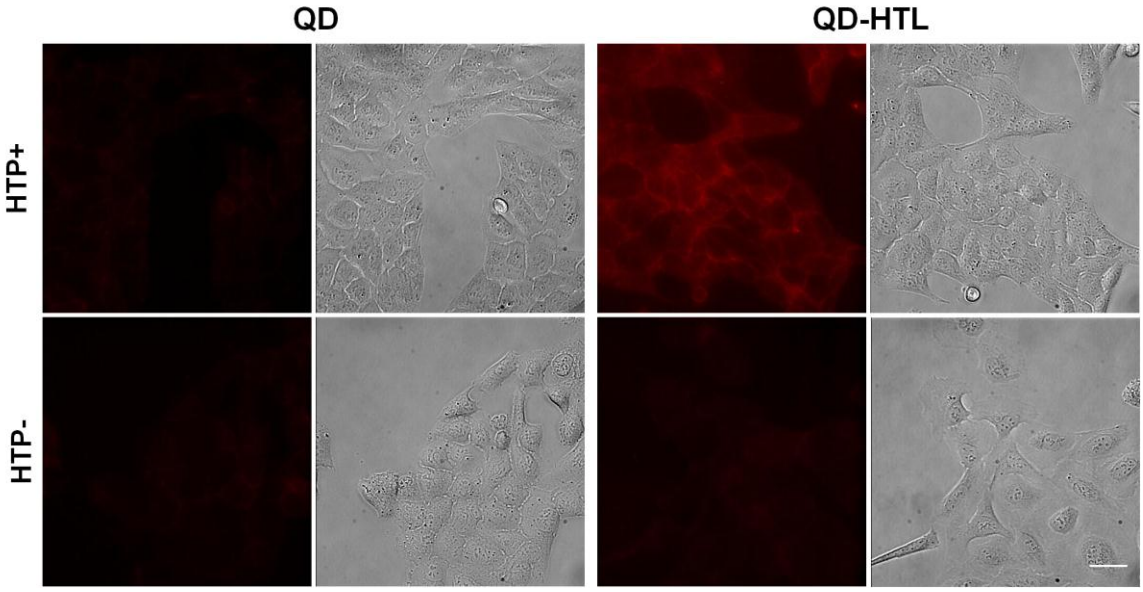

Figure 5.7. Staining specificity of PEG-QD-HTL conjugates to HaloTag protein expressing (HTP+) cells with respect to control (HTP-) cells and PEG-QDs lacking HaloTag ligand. Both PEG-QDs and PEG-QD-HTLs are coated with 10,000 excess of 1000 MW PEG. PEG-QD-HTLs of low surface ligand density are prepared using a 2:1 HTL:QD molar incubation ratio using 2500 MW HTLs. Scale bar = 40 μm.

Four Types of Binding

The results of our studies regarding interactions between QD-HTLs and cells can best be summarized into four different types of binding (Figure 5.8). The goal of our staining is to achieve "specific covalent binding" (Figure 5.8, far left). Unlike affinity based QD-ligand systems, QD-HTL binding to HTP is *covalent* and will never dissociate. An important corollary is that binding of QD-HTL to HTP cannot be washed out, while all nonspecifically bound QD-HTLs can be washed out—at least in theory, if not in practice. Thus, greatest efforts to eliminate nonspecific binding should focus on increasing the dissociation rate of nonspecifically bound QD-HTLs.

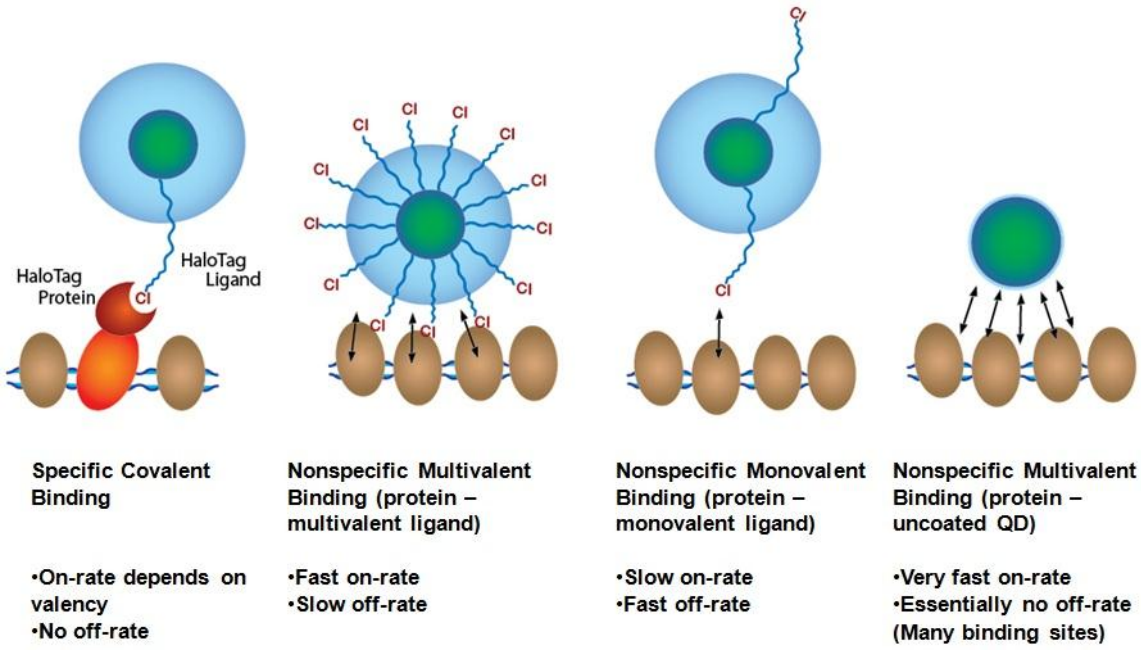

Figure 5.8. Summary of the four types of binding of quantum dot-HaloTag ligand conjugates to cellular systems.

Nonspecific binding can either be QD-mediated or ligand-mediated. If the QD-HTL is either uncoated or covered with a thin coating, then QD-mediated nonspecific multivalent binding is dominant (Figure 5.8, far right). An uncoated QD essentially contains an infinite number of binding sites; consequently, it is virtually impossible to wash out uncoated, nonspecifically bound QDs from cells. On the other hand, if the QD surface coating is adequately thick, then most of the nonspecific binding will be ligand-mediated.

Just as multivalent interactions can increase the effective on-rate of binding (i.e. through "avidity"), we have found that multivalent interactions can also decrease the effective off-rate of binding. For instance, if the probability of dissociation for a nonspecifically bound HTL is 50%, then the probability of dissociation for a nonspecifically bound monovalent QD-HTL is also 50%. However, the probability of dissociation for a multivalent QD-HTL containing three nonspecifically bound ligands would only be 12.5%. For the HaloTag system, monovalent QD-HTLs can be removed with repeated washing, whereas multivalent QD-HTLs cannot. Even QDs with two ligands on the surface can function effectively as "monovalent" probes if the ligands are well-spaced (Figure 5.8, center right). This phenomenon may account for the dramatic increase in nonspecific binding for QD-HTLs prepared with a 4:1 HTL:QD ratio as compared to QD-HTLs prepared with a 2:1 HTL:QD ratio, as shown in Figure 5.5.

5.4 Conclusions

In this study, we have optimized the labeling conditions to achieve specific cellular staining with Quantum Dot-HaloTag ligand probes. We have found that HaloTag ligand binding to cellular HaloTag protein is robust, able to withstand changes in staining

concentration, temperature, and even slight changes in pH. We further discover that staining at 37 ^{0}C is better than staining at 4 ^{0}C for reducing nonspecific binding of HaloTag probes.

Two especially interesting observations emerged from our studies of the interactions of Quantum Dot-HaloTag ligand probes with cellular surfaces. First, we found that low molecular weight ligands can become buried in nanoparticle surface coatings that are too thick, decreasing the effectiveness of binding. Second, we found that a low nanoparticle surface ligand density close to monovalency is essential for achieving specific HaloTag binding.

Monovalency has long been regarded as essential for single-molecule imaging as multivalent probes can crosslink receptors, prohibiting the imaging of single proteins [10, 12]. Our study now shows that monovalent systems may confer additional benefits such as reduced nonspecific binding.

Importantly, this work presents a clear example where increased surface ligand density can cause increased nonspecific binding. Due to their large surface area to volume ratio, nanoparticles are capable of presenting multiple surface ligands to target cells of interest with high avidity. Because of this "multivalency effect," nanoparticles have long been promoted as excellent carriers for targeted drug delivery and imaging [175-178]. However, just as multivalent ligands can increase the avidity of specific binding, they can also increase the avidity of nonspecific binding, such that specific targeting is no longer achieved. Since the effectiveness of the nanocarrier will largely depend on the properties of the receptor-ligand system employed, our results challenge researchers to make careful choices when designing multivalent nanocarrier systems.

This work presents one of the first illustrative examples of the effect of multivalency on nonspecific binding. It highlights the fundamental importance of carefully considering both kinetics and surface chemistry in nanoparticle ligand based probe designs. These considerations will help guide the design of next-generation nanoparticle-based imaging agents for visualization of cellular and biomolecular interactions, especially at the single-molecule level.

CHAPTER 6

QUANTUM DOT-HALOTAG LIGAND CONJUGATES FOR DYNAMIC IMAGING OF CELLULAR PROTEINS

6.1 Introduction

The commercialization of QD technology has greatly facilitated the widespread adoption of QDs into many fields of biomedical research, ranging from *in vivo* imaging to multiplexed disease detection [13]. Single-molecule imaging is one such field that has greatly benefited from the accessibility of commercial QDs. Nonetheless, the growing consensus is that commercial QDs are becoming increasingly limited in utility due to their large size and multivalency. Large QDs are unable to access confined areas of the cell, and multivalent QDs pose problems with receptor crosslinking. As our studies have shown, multivalent QDs may also exhibit increased propensity for nonspecific binding compared to their monovalent counterparts. Indeed, the development of high-quality QD imaging probes that are small and monovalent would generate a marked improvement over the current state-of-the-art technology, paving the way for future advances in cellular imaging [173].

Thus far, only a few studies integrating the use of size-minimized tagging strategies with size-minimized QDs for single-molecule imaging have been published. For example, Howarth et al. used dihydrolipoic acid QDs in conjunction with enzymatic BirA labeling to track glutamate receptors in hippocampal neurons [10]. Roullier and coworkers used gallate-PEG coated QD-Ni^{2+}-Tris-nitrilotriacetic acid conjugates to track

his-tagged interferon receptors [93]. The majority of these studies have been performed using noncovalent techniques that are incompatible with intracellular labeling.

Our study seeks to optimize the imaging parameters needed such that multidentate polymer coated QD-HaloTag ligands can become a viable alternative to the probes used in these studies. Such an alternative would prove especially useful in multi-color tracking experiments, in which different tagging strategies are needed to label each different type of protein. Additionally, our QD-HTL conjugates can potentially be used for intracellular imaging. We hope these initial optimization studies with cell surface proteins will help pave the way for the full potential of QD-HTLs to be achieved in the future, such that QD-HTLs can one day also be used for intracellular single-molecule imaging.

We have already demonstrated in previous chapters that small, monovalent QD-HTL conjugates can successfully bind target HaloTag proteins in cells and in solution. We now seek to evaluate their performance when applied to single-molecule imaging of cell surface proteins.

6.2 Materials and Methods

Quantum Dot-HaloTag Ligand Functionalization

To produce monovalent probes, quantum dots with a very low degree of HaloTag functionalization were prepared. Based on the estimate of actual number of ligands per QD for a given molar reaction ratio (Chapter 4), QD-HTL conjugates were prepared at a 0.5:1 HTL:QD molar reaction ratio. All QD-HTL probes were prepared with 2500 MW HaloTag ligands and subsequently coated with 10,000 excess 1000 MW PEG and 7,500 excess EDC according to the procedure described in Chapter 4.

Widefield Epifluorescence Microscopy

Cells were imaged on an Olympus IX71 epifluorescence inverted microscope equipped with a Hamamatsu C9100 EM-CCD camera using a 100x objective. All samples were illuminated using a mercury arc lamp. The following filters were used for visualization of QDs (629 emission): 480/40 excitation, 625/20 emission, 500 dichroic. Images were streamed continuously to a computer hard disk with exposure times ranging from 50-150 ms. For single-molecule imaging, a longer excitation wavelength (480/40) was chosen in comparison to the UV excitation used for ensemble imaging (335-380), as UV excitation has been attributed to increased blinking of QDs and higher autofluorescence compared to longer wavelengths [172, 173].

Total Internal Reflection Microscopy

Single molecule tracking of fluorescent dyes was performed using a TIRFM setup to enhance the signal-to-noise ratio (SNR) and reduce the effects of photobleaching during imaging. The TIRFM setup consists of an Olympus IX71 inverted microscope equipped with a 60x TIRFM objective and Hamamatsu C10600-10B CCD camera. TMR ligand (555 excitation, 585 emission) was illuminated using a 561 yellow green laser line and visualized with a standard TRITC emission filter (565-605).

Identification of Single Fluorophores and Single Fluorophore Tracking Analysis

Single fluorescent dyes were identified by their single-step photobleaching [7, 179]. Single quantum dots were identified from their blinking intermittency [78]. Fluorophore intensity analysis was performed using the MacBiophotonics plugin for ImageJ (McMaster University, Canada) [180]. Tracking software was modified from the open-source “Object Tracking Software” available from the Rowland Institute at Harvard

as described in detail in the Results and Discussion section [181]. When necessary, manual tracking was performed using the Manual Tracking plugin for ImageJ developed by Fabrice P. Cordelières (Institut Curie, France) to confirm the results of the automatic tracking algorithm [182].

6.3 Results and Discussion

Selection of Microscope Excitation and Emission Wavelengths

Due to their large extinction coefficients and absorption cross-sectional areas, QDs can be visualized on a standard epifluorescence microscope without need for special optical setups such as TIRF microscopy to enhance the signal-to-noise ratio. Nonetheless, to visualize single quantum dot trajectories, careful attention should be placed on optimizing the microscope settings and recording parameters. In general, widefield epifluorescence microscopy is preferred for single QD tracking over confocal microscopy due to the reduction in incident light caused by the confocal pinhole aperture [173]. We were able to visualize single QDs on a standard Olympus IX71 inverted epifluorescence microscope equipped with a highly sensitive EM-CCD camera and a mercury arc lamp.

QDs with 629 nm emission were selected for the single-molecule imaging studies since cellular autofluorescence is reduced in the red spectral region (600-700 nm) [173, 183]. Since the QD extinction coefficient increases at higher energy, shorter excitation wavelengths result in higher QD signal intensity, and UV excitation is often chosen to maximize signal output. Unfortunately, we found that UV excitation (335-380 nm) resulted in high cellular autofluorescence and greater cytotoxicity. Exciting at a slightly higher wavelength window, 440 – 520 nm, was found to be ideal, resulting in minimal cell death and reduced autofluorescence while still producing a high QD signal to

background ratio. Single QDs could be visualized using a 100x oil immersion objective with a 1.4 numerical aperture.

Cellular Staining Optimization

In order to accurately reconstruct the QD trajectories, staining must be performed at low density to avoid overlap of trajectories. We incubated cells with 0.2 nM QD conjugates for 2 minutes, and then performed five quick washes before recording trajectories on the microscope. Staining and imaging were performed as quickly as possible to minimize internalization of QD conjugates into cells. Since QDs should be monovalent to avoid crosslinking of receptors, QDs were functionalized with HTL at a 0.5:1 HTL to QD ratio. Under these conditions, Figure 6.1 shows that pegylated QD-HTL conjugates were able to specifically stain cells expressing a β1 integrin-HTP fusion with respect to native cells and pegylated QDs lacking HaloTag ligand.

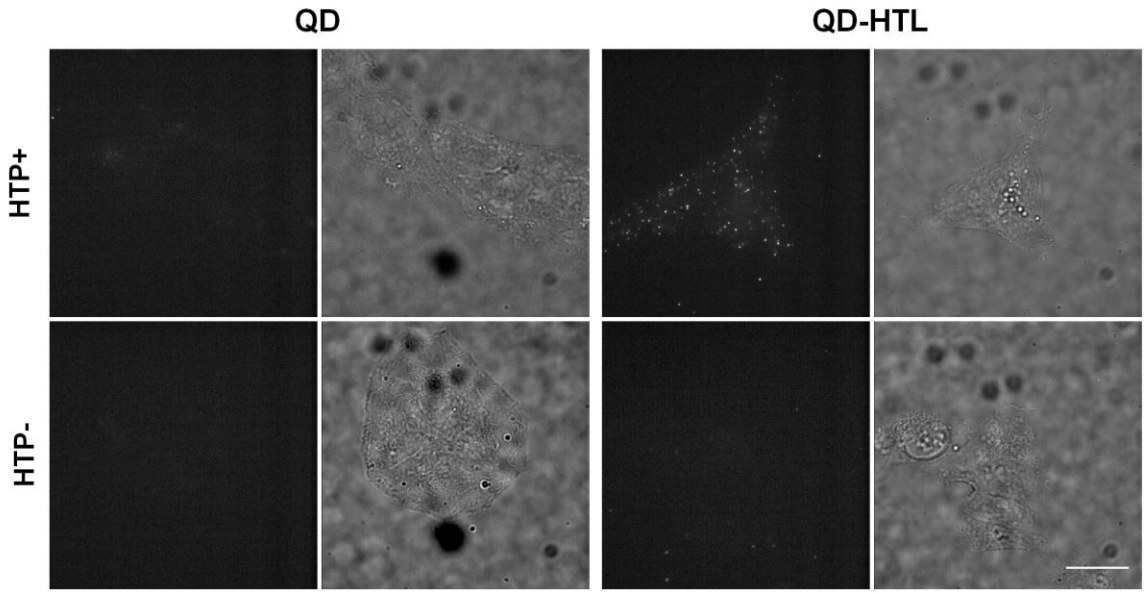

Figure 6.1. Staining specificity of PEG-QD-HTL conjugates to β1 integrin-HaloTag protein (HTP+) expressing cells at low staining density with respect to control (HTP-) cells and PEG-QDs lacking HaloTag ligand. Both PEG-QDs and PEG-QD-HTLs are coated with 10,000 excess of 1000 MW PEG. PEG-QD-HTLs are prepared using a 0.5:1 HTL:QD molar incubation ratio. Scale bar = 20 μm.

Quantum Dot Tracking Approaches and Limitations

Single QDs can be recognized by their signature blinking pattern, while QD aggregates do not blink [78]. This blinking process occurs essentially randomly, and involves transient moments when the QD fluorescence disappears ("off state") and quickly re-appears ("on state"). While QD blinking offers a facile method for identifying single QDs, it poses a logistical challenge for reconstructing QD trajectories. Because of QD blinking, it is also impossible to distinguish between QDs diffusing out of the focal plane and QDs simply in their off state.

The easiest method for tracking QDs while accounting for blinking is to perform manual tracking. In this method, the user clicks on the fluorescent spot corresponding to

the QD trajectory of interest through successive frames using a mouse cursor. Manual tracking allows the user to pick out desired QDs from aggregates, and allows the user to easily piece together tracks before and after each blink. However, manual analysis is extremely low throughput and may be subject to potential experimenter bias.

In previous years, a few algorithms have been developed that are able to piece together QD trajectories before and after each blink [184-188]. For example, Bonneau and coworkers developed an elegant algorithm for tracking QDs based on perceptual grouping of minimal paths in a 3-D volume (Figure 6.2). In their approach, QD trajectories are recorded and exported as a time series of 2-D images, each encoding the (x, y)-position of the QDs. The algorithm creates a 3-D volume of these frames with time as the third axis. In each frame, QDs are automatically detected and located by using Gaussian fitting of the intensity profile to identify fluorescent spots. Lastly, correspondence between spots is established by identifying the nearest neighbor spot within the volume and subsequently connecting the dots [185].

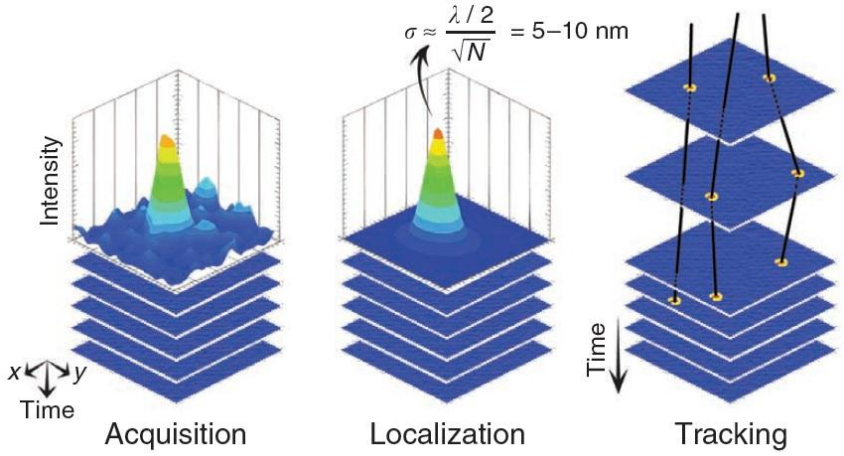

Figure 6.2. Example of an automatic QD tracking algorithm. First, QD trajectories are acquired as a series of 2-D images and arranged into a 3-D volume using time as the third axis. Second, QDs are automatically localized using Gaussian fitting of the point spread function (PSF) intensity profile. Finally, spots from each frame are connected by linking the centers of nearest-neighbor fluorescent spots across adjacent frames. The localization accuracy σ of the QD is a function of λ, the QD's emission wavelength and *N*, the total number of detected photons. Adapted from [173].

This example also illustrates some of the limitations inherent to automatic tracking algorithms. Since QDs are automatically detected by the software, it may be difficult to distinguish between desired QD trajectories and undesired trajectories. In general, the software will indiscriminately detect and track all spots in a given image, whether on the cell, in solution, or immobilized on the glass slide—in focus or out of focus. Consequently, special care must be taken to ensure that all detected spots are indeed on the cell surface in the proper focal plane. With automatic detection, it is also virtually impossible to distinguish between spots corresponding to single QDs and spots corresponding to QD aggregates. Because large aggregates are often less mobile or immobile, the calculated average diffusion coefficient may be lower than actual when aggregates are present. Another limitation is that these algorithms generally rely on the

assumption that the distance between two different QDs is larger than then diffusion distance of each individual QD. While this is generally true when the staining density is low, a possibility exists that the algorithm may fail to correctly piece together trajectories of extremely fast-diffusing QDs. In summary, automatic tracking algorithms offer the advantage of being able to process large populations of QDs for long periods of time. However, possible inaccuracies that may arise from the automation process must be taken into consideration. Trajectories analyzed using automatic tracking algorithms should be carefully reviewed to ensure they accurately reflect desired QD labeled proteins of interest. To date, the number of commercially available or freely downloadable algorithms that account for QD blinking still remain limited.

In our study, we sought to combine the best of both worlds of automatic and manual tracking by implementing a semi-automatic tracking procedure. While populations of particles were automatically tracked, we manually pieced together interrupted trajectories between blinks. We also manually isolated desired trajectories in order to ensure QDs were located on the cell surface and that aggregates were excluded from analysis.

Quantum Dot Tracking Algorithm

We adapted our tracking algorithm from the open-source "Object Tracking Software" available from the Rowland Institute at Harvard [181]. We chose this software primarily because of its open-source nature and its Matlab runtime environment, which would allow us to easily make modifications to the software code when needed. An image sequence is first converted into a stack of 2-D images and uploaded into the software. The general algorithm can be summarized into the following basic steps:

1. Retrieve an image frame.
2. Define an intensity threshold for each particle in the frame.
3. Locate the center of each particle.
4. Define a circle with distance cutoff radius, "R" = the maximum distance a particle can move from one frame to the next.
    - If 1 particle is in the circle, continue tracking
    - If 2 or more particles are in the circle, retire old track, start 2+ new tracks
    - If 0 particles are in the circle, retire old track
5. Complete tracking.
6. Isolate tracks of interest and/or delete unwanted tracks.
7. Piece together interrupted tracks.
8. Output coordinate information for further analysis.
9. Compute the mean squared displacement and diffusion coefficient.

Several alterations were made to the original open source software. For instance, we modified the program to output track coordinates into Microsoft Excel, where tracks could be reviewed. At this point, tracks that did not reflect blinking QDs were eliminated. We wrote additional code that would allow the computation of the mean squared displacement (MSD) versus time and the diffusion coefficient from the track data.

Quantum Dot Tracking Example

An example of a single QD tracking sequence is shown in the multimedia file associated with Figure 6.3. To determine the locations of the QDs, the first step is to

define an intensity threshold for detecting the fluorescent spots. This threshold is selected as a number from 0 to 255 for an 8-bit grayscale image. As shown in Figure 6.4, if the intensity threshold is too low (e.g. set at "30"), the tracking algorithm picks up too much noise. If the threshold is too high (e.g. set at "70"), the tracking algorithm fails to detect several QDs, and instead primarily detects aggregates, which often appear brighter than single QDs. For our tracking example, an intensity threshold of "50" was found to be appropriate.

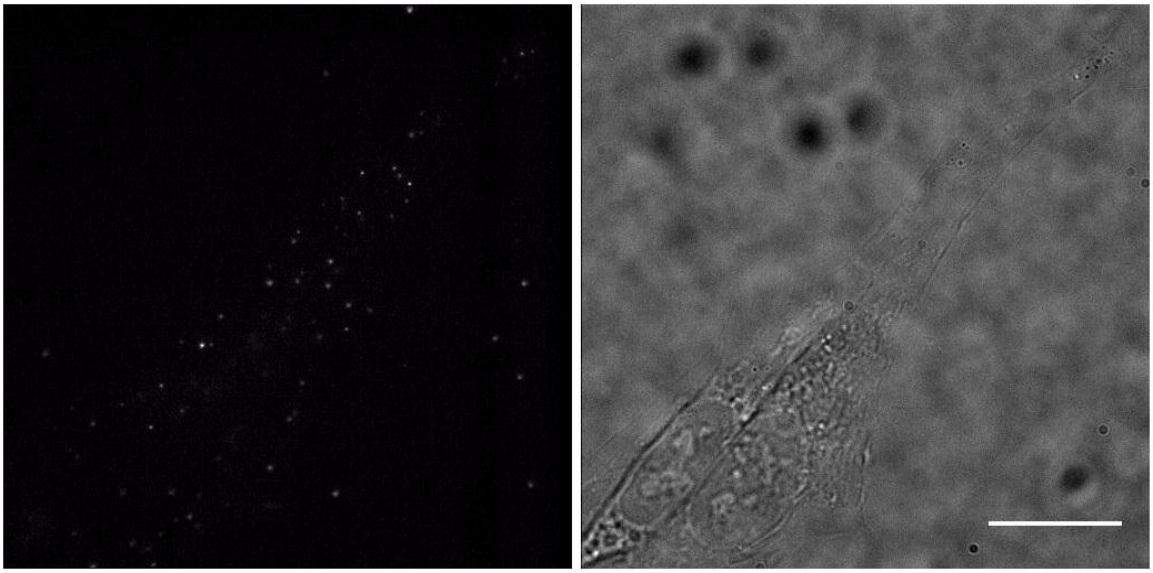

Figure 6.3. Single-molecule tracking of cell surface β1 integrin-HTPs labeled with PEG-QD-HTL conjugates (wen_mary_m_201308_phd_fig63_qdtracking.avi). Images were streamed continuously using an exposure time of 150 ms. Movie sequence is shown at 7 frames per second (fps). Scale bar = 20 μm.

The next step is to define the distance cutoff radius, "R," as the maximum distance in pixels a QD can travel from one frame to the next. Figure 6.5 shows histograms of all single-frame displacements, also known as the distance traveled by each

QD within a particular frame, up to each given value of "R". When the R value is too low (e.g. R = 1), the histogram abruptly terminates at the designated R value. The fact that the histogram never smoothly "levels off" at R =1 suggests that several displacements greater than 1 pixel exist in reality. When the R value is too high (e.g. R = 25), the search radius starts to pick up other QDs in the vicinity. An R value of 6 pixels was found to be reasonable for our example. Due to the presence of immobilized aggregates that have not yet been filtered out at this stage in the tracking process, many QDs exhibit very low displacement values < 0.2 pixels.

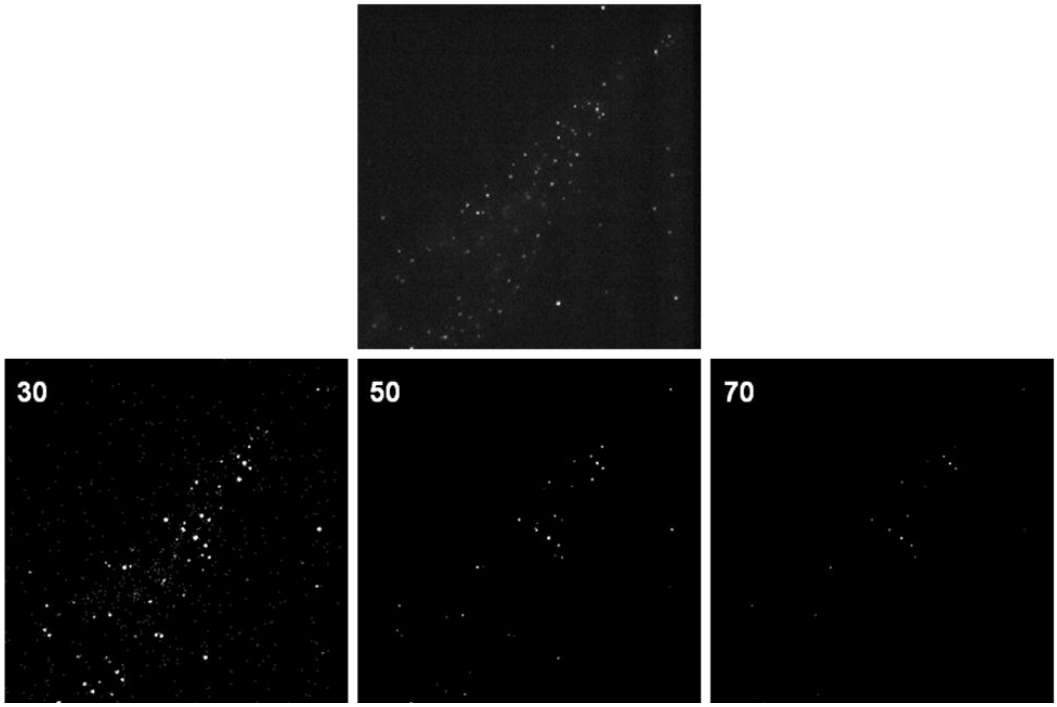

Figure 6.4. Setting the intensity threshold for identification of quantum dots in the tracking procedure. For an 8-bit grayscale image, the intensity threshold is given as a number between 0 and 255.

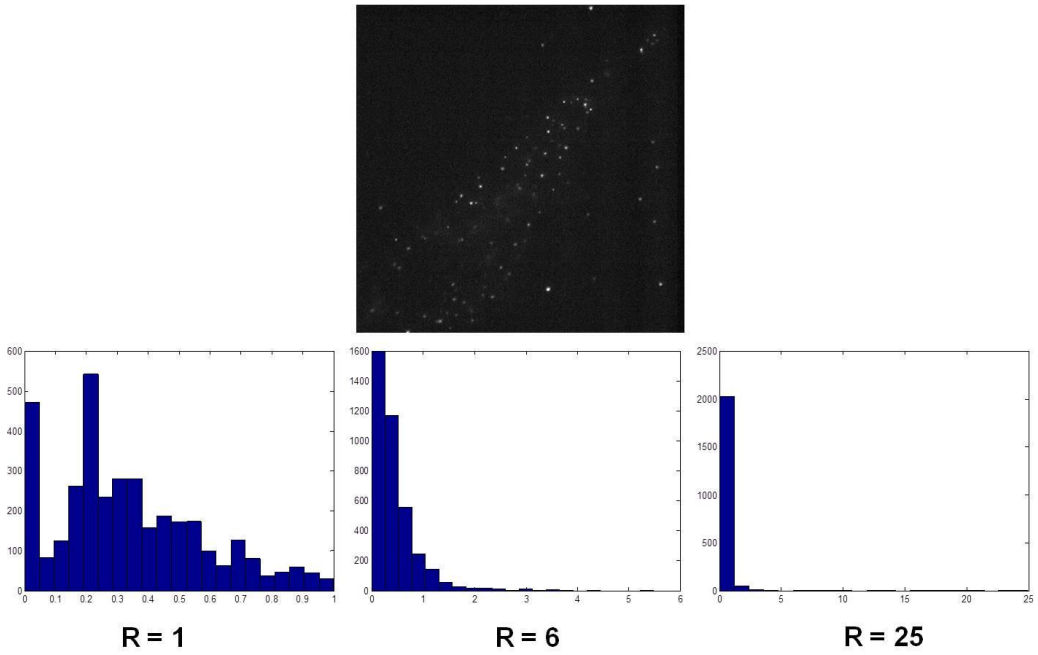

Figure 6.5. Setting the distance-cutoff radius "R," also known as the maximum distance a quantum dot can travel between two image frames in pixels.

Upon successful optimization of the intensity threshold and distance cutoff radius, tracking can be performed. Figure 6.6 shows the tracking results for our example, along with the subsequent processes of deleting unwanted tracks and manually piecing together interrupted tracks.

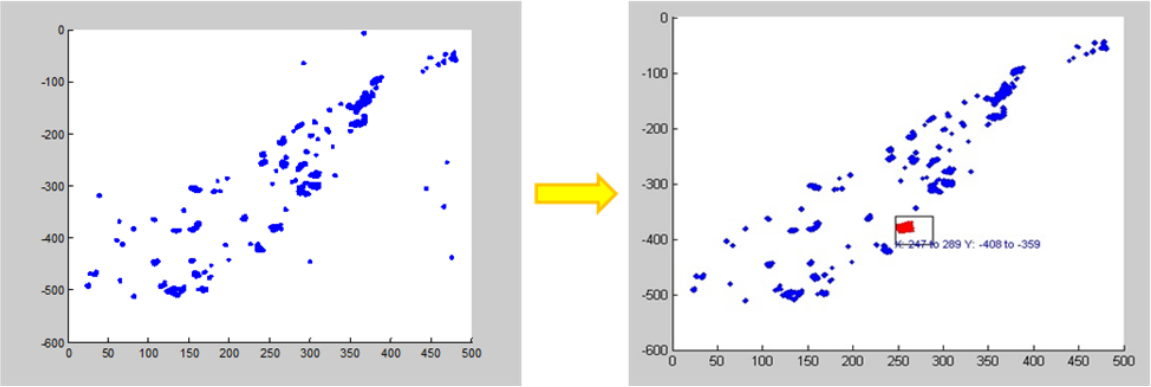

Figure 6.6. Results of QD tracking and subsequent isolation of desired tracks.

For each trajectory (x(t), y(t)), the mean squared displacement can be calculated using the following formula,

$$\mathrm{MSD}(n\tau) = \frac{1}{N-n}\sum_{i=1}^{N-n}\left[\left(x((i+n)\tau) - x(i\tau)\right)^2 + \left(y((i+n)\tau) - y(i\tau)\right)^2\right] \qquad \text{Equation 6.1}$$

where N is the total number of frames, τ is the acquisition time, and time $t = n\tau$ [172, 173, 189]. Once the MSD vs. time plot has been established, the diffusion coefficient (D) can be determined by fitting the first four points of the curve using the following equation:

$$\mathrm{MSD}\ (n\tau) = 4Dn\tau + b \qquad \text{Equation 6.2}$$

The type of motion exhibited by the QD trajectory can be determined by examining the shape of the curve [190-192]. When $b = 0$, the QD exhibits normal Brownian diffusion:

Normal diffusion $\mathrm{MSD}\ (n\tau) = 4Dn\tau$ Equation 6.3

When directed motion with velocity *v* is present, as in the case of active transport with molecular motors, the MSD curve can be described as follows:

Directed motion $\text{MSD}(n\tau) = 4Dn\tau + v^2n^2\tau^2$ Equation 6.4

Finally, when the trajectory undergoes diffusion in a confined area, the MSD curve approaches a horizontal asymptote of value L:

Confined diffusion $MSD(n\tau) = \frac{L^2}{3}\left(1 - exp\left(-\frac{12Dn\tau}{L^2}\right)\right)$ Equation 6.5

The shape of the MSD versus time curves for different types of diffusion is depicted in Figure 6.7.

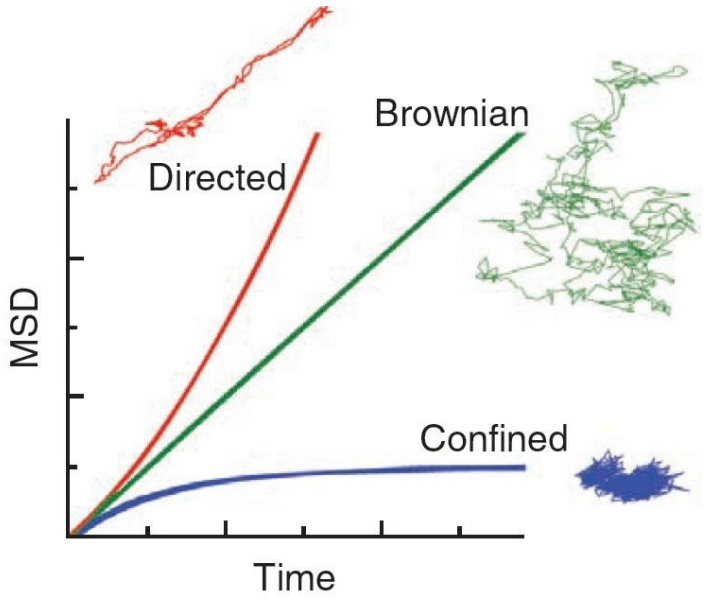

Figure 6.7. Different types of single-molecule motion as classified by the mean squared displacement. Single molecules may exhibit Brownian diffusion (green), confined diffusion (blue), or directed motion via active transport (red). Adapted from [173].

Diffusion Characteristics of Quantum Dot-HaloTag Ligand Labeled β1 Integrin-HaloTag Proteins

Figure 6.8 shows examples of some MSD curves calculated for the PEG-QD-HTL labeled β1 integrin-HTPs diffusing on the cell surface. The vast majority of the proteins exhibited confined diffusion, with less than 5% exhibiting free diffusion. In this example, no evidence of directed motion was found.

This behavior is consistent with the behavior of β1 integrins described in the literature. While tracking the mobility of α5β1 integrins on the surface of fibroblasts using polystyrene beads, Hirata and coworkers likewise observed that the vast majority of beads exhibited restricted diffusion, with only two beads exhibiting Brownian diffusion [193].

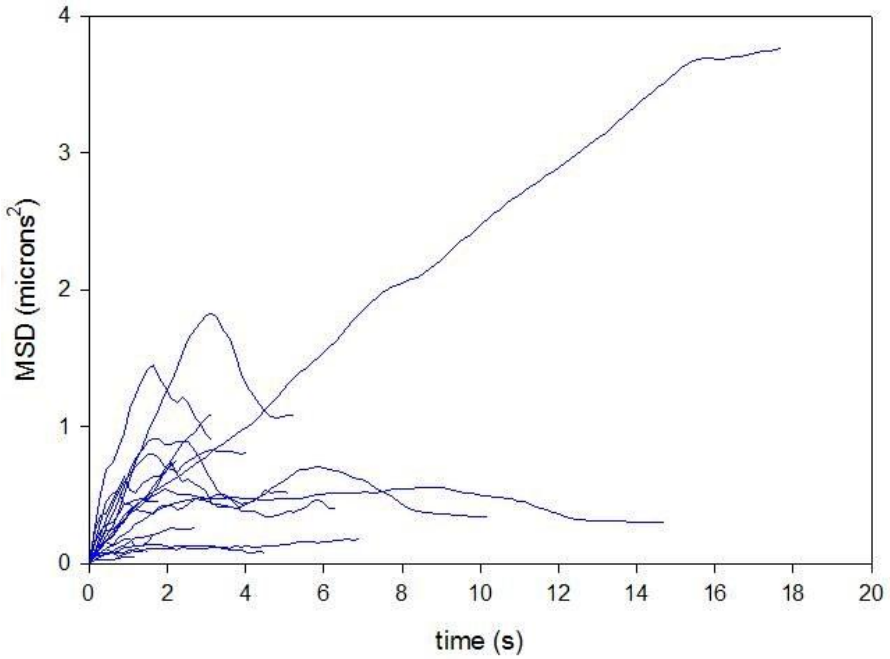

Figure 6.8. Examples of various mean squared displacement curves over time for cell surface β1 integrin-HaloTag proteins labeled with pegylated QD-HTL conjugates.

We determined the average diffusion coefficient for β1 integrin-HTPs diffusing on the surface of the U2OS-ECS1-HTP cells to be $2.41 \times 10^{-10} \pm 1.94 \times 10^{-10}$ cm^2/s. This is fairly consistent with the values of diffusion coefficients reported in the literature. Using Invitrogen 655 QD-antibody conjugates, Chen and coworkers determined the diffusion coefficient of β1 integrins on the surface of human osteoblasts to be in the range of $1 - 5 \times 10^{-10}$ cm^2/s [28]. Using fluorescence recovery after photobleaching (FRAP) to study β1 integrin mobility, Duband and coworkers determined the range of diffusion coefficients to fall within $2 \times 10^{-10} \leq D \leq 4 \times 10^{-10}$ cm^2/s [194]. Virtually all of these studies reported a broad distribution of diffusion coefficients for β1 integrin movement. For example Hirata et al. observed a 15-fold difference between their lowest and highest diffusion coefficient value, with values as high as 2×10^{-9} cm^2/s for some integrins [193].

Comparison of β1 Integrin-HaloTag Proteins Labeled with Quantum Dot-HaloTag Ligands versus TMR Ligands

The above results show that the activity of β1 integrin-HTPs labeled with QD-HTLs is consistent with the activity of β1 integrin reported in the literature, as measured using a wide variety of different techniques. To see if differences in labeling probe would affect integrin activity, we sought also to evaluate the activity of β1 integrin-HTPs labeled with QD-HTLs with respect to β1 integrin-HTPs labeled with TMR ligand.

Figure 6.9 shows the difference between HTP-β1 integrins tracked using PEG-QD-HTLs versus TMR ligand using widefield microscopy. This figure highlights the inherent challenges of performing single-molecule imaging with fluorescent dyes with standard epifluorescence microscopy. Even when TMR ligand, the brightest commercially available dye-HaloTag ligand conjugate, was used, the signal-to-noise ratio

was so low that the image sequences could neither be tracked automatically or manually (Figure 6.9b). Instead, total internal reflectance microscopy (TIRFM) was needed to obtain adequate signal from TMR ligand-labeled integrins for tracking purposes (Figure 6.10).

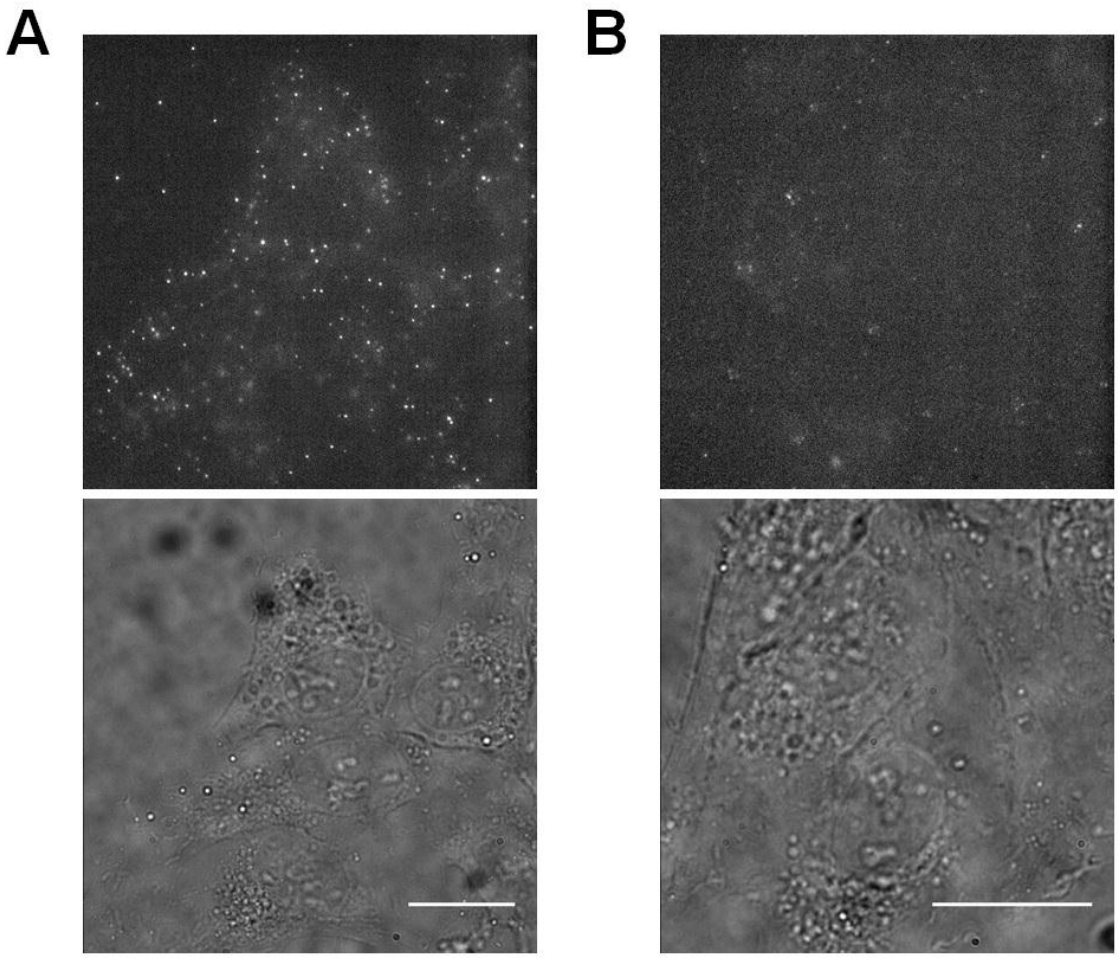

Figure 6.9. Comparison of single-molecule tracking of cell surface β1 integrin-HTPs labeled with PEG-QD-HTLs versus TMR ligands using widefield microscopy. (a) β1 integrin-HTPs labeled with PEG-QD-HTLs (wen_mary_m_201308_phd_fig69a_qdtracking.avi). (b) β1 integrin-HTPs labeled with TMR ligand (wen_mary_m_201308_phd_fig69b_tmrtracking.avi). Movie sequences are shown at the same dynamic range, same frame rate (7 fps), and same exposure time (150 ms). Scale bar = 20 μm.

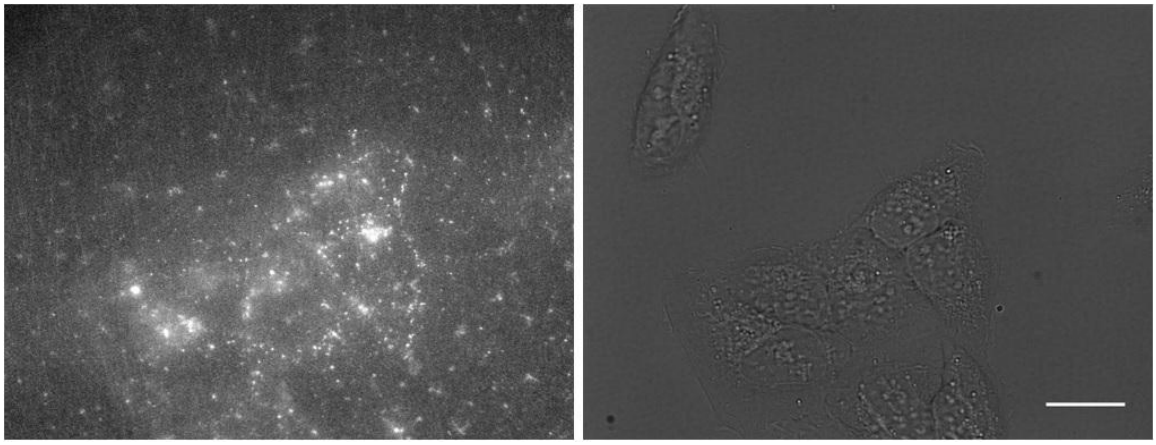

Figure 6.10. Single-molecule tracking of cell surface β1 integrin-HTPs labeled with TMR ligands using total internal reflectance microscopy (wen_mary_m_201308_phd_fig610_tmrtirf.avi). In this example, images were streamed continuously using an exposure time of 500 ms. Movie sequence is shown at 2 frames per second. Scale bar = 20 μm.

Figure 6.11 shows the results of our study comparing the distributions of PEG-QD-HTL vs. TMR-ligand labeled β1 integrin-HTPs. The mean diffusion coefficients for PEG-QD-HTL labeled integrins and TMR ligand labeled integrins were found to be 2.41 x 10^{-10} cm^2/s and 2.67 x 10^{-10} cm^2/s, respectively. The median diffusion coefficient for PEG-QD-HTL labeled integrins was 2.08 x 10^{-10} cm^2/s, while the median diffusion coefficient for TMR ligand labeled integrins was 1.62 x 10^{-10} cm^2/s. The diffusion coefficient values for β1 integrin-HTPs labeled with PEG-QD-HTL and TMR ligand were found not to be significantly different according to the Mann Whitney U Test ($p>0.05$). Together, these results indicate that the QD-HTL label does not drastically alter β1 integrin activity compared to the fluorescent dye label.

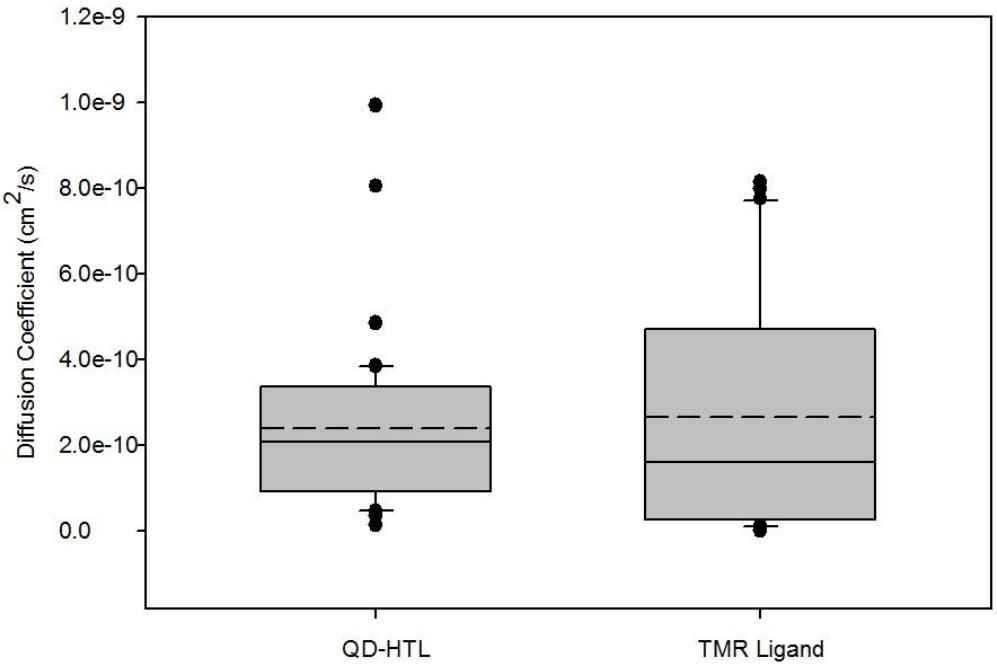

Figure 6.11. Box plots comparing diffusion coefficients of β1 integrin-HTPs labeled with pegylated QD-HTLs and TMR ligands. The median is denoted by a horizontal solid line (—) while the mean is denoted by a horizontal dotted line (---). Upper and lower box boundaries indicate the 75th and 25th percentiles, while the whiskers above and below the box indicate the 90th and 10th percentiles respectively. Outliers are indicated by dots.

6.4 Conclusions

In this chapter we have shown that QD-HTL conjugates can be used for single-molecule imaging of cell surface proteins. We have developed a semi-automatic tracking algorithm that allows us to automatically track proteins labeled with QDs while manually identifying tracks of interest. We show that QD-HTLs exhibit enhanced signal-to-noise ratio and greater resistance to photobleaching when compared to fluorescent dyes, allowing facile tracking of single proteins on a standard epifluorescence microscope. Importantly, we demonstrate that the behavior of cell surface β1 integrin-HaloTag fusion proteins labeled with QD-HTLs exhibit behavior that is similar to the behavior of β1

integrins reported in the literature. These QD-HTL labeled β1 integrin-HaloTag fusion proteins exhibit similar diffusion coefficients and confined diffusion behavior as native β1 integrins, as reported in the literature using a wide variety of techniques including bead labeling and fluorescence recovery after photobleaching. Altogether, these results demonstrate that size minimized quantum dot-HaloTag ligand conjugates are a promising new technology for visualizing single molecules in live cells at high resolution.

CHAPTER 7

SUMMARY AND FUTURE DIRECTIONS

7.1 Summary

The goal of this dissertation, as outlined in Chapter 1, was to develop new tagging strategies that better enable quantum dots to be used for tracking receptors in dynamic live cell imaging. In Chapter 2, we discussed the advantages of quantum dots over fluorescent dyes for live cell imaging, especially single-molecule imaging. We also discussed some of the major limitations of current QD probes and how the next generation of QD probes should be improved to better facilitate imaging.

In Chapter 3, we specifically focused on improvements that can be made in reducing the size of current QDs and in improving their targeting strategies. We identified HaloTagging as a potential strategy that would meet both the demand of reducing QD probe size while offering improved binding characteristics to target receptors. We proposed that low molecular HaloTag ligands could be grafted onto the surface of size-minimized QDs, and that the resulting conjugates could be used to covalently bind and track cellular receptors genetically fused to a HaloTag protein.

In Chapters 4 through 6, we sought to develop the proposed quantum dot-HaloTag ligand conjugates and to test their binding to cellular proteins before applying them to the single molecule tracking of cellular receptors. The first purpose of Chapter 4 was to develop a synthesis procedure for reacting HaloTag ligands with compact multidentate-polymer coated QDs to produce size-minimized QD-HTL conjugates. The second purpose was to optimize the QD surface chemistry needed to achieve specific

binding between QD-HTL conjugates and purified HaloTag proteins in solution. Several variables were investigated including the length of the HaloTag ligand, the number of HTLs on the surface, and the amount of PEG coverage needed to reduce nonspecific binding. Our results showed that longer HaloTag ligands bind more effectively to target proteins compared to shorter ligands when coupled to nanoparticle surfaces. One promising observation was that QDs displaying a low density of surface ligands were able to bind target protein just as effectively as QDs displaying a high surface ligand density. While addition of PEG molecules to the surface coating helped to reduce nonspecific binding, excessive PEG was found to obscure HaloTag ligand binding, thereby proving that a careful balance was needed to achieve specific binding.

The focus of Chapter 5 was to optimize the conditions needed to achieve specific binding between QD-HTL conjugates and cells expressing HaloTag proteins. Several major trends observed in Chapter 4 regarding binding to soluble proteins were again mirrored with binding to cellular protein. As shown in Chapter 4, PEG was needed to prevent nonspecific binding to cells, but excessive PEG could block specific HaloTag binding. This was especially manifest when longer PEG lengths, which could easily bury the ligand, were used. Again, QDs with low surface ligand density were found to bind cellular HaloTag protein just as well as QDs containing a high ligand density. In Chapter 5, however, an important new observation emerged: QDs containing a high surface ligand density were found to exhibit higher nonspecific binding to cells than those containing low surface ligand density. In fact, only QDs with very low ligand densities near monovalency were found to exhibit specific staining of HaloTag protein expressing cells with respect to controls.

One important theme that has resounded throughout this thesis is the delicate balance between specific and nonspecific binding. This fine interplay is strongly mediated by the QD surface parameters, including ligand length, ligand valency, PEG length and PEG density. In Chapter 5, we were able to strike an appropriate balance among these variables to create QD-HTLs capable of specifically labeling β1 integrin-HaloTag fusion proteins on cell surfaces.

Finally, in Chapter 6 we extended these QD-HTL conjugates to the live cell imaging of β1 integrin-HaloTag fusion proteins on a single-molecule level. We showed that these QD-HTLs exhibit superior performance to fluorescent dyes in terms of photostability and signal-to-noise ratio. We also showed that these QD-HTLs convey accurate information regarding integrin movements compared to other reported studies.

This work is *significant* because it is the first to successfully synthesize size-minimized QD-HTLs that bind specifically to purified and cellular HTP. It is also the first study to utilize these QD-HTLs for dynamic single-molecule imaging of cellular proteins. For the first time, we have identified the binding parameters that govern the interactions between QD-HTLs and cellular HTP, and we have further shown that monovalency is ideal for achieving specific HaloTag binding. Altogether, our results show that size-minimized QD-HTLs exhibit promise for use as single-molecule imaging probes for dynamic live cell imaging.

Opportunities now arise for extending the application of the QD-HTL conjugates to the detailed investigation of other biological receptors in living cells. Below, we detail some of the most exciting opportunities for advancing and applying this quantum dot-HaloTag technology.

7.2 Future Directions

Intracellular Protein Targeting of Quantum Dot-HaloTag Ligand Conjugates

Direct QD labeling of intracellular proteins is arguably the most important hurdle that must be overcome for QD-tracking to gain widespread utility in live cell imaging applications; yet for many reasons, it remains a highly ambitious goal fraught with many challenges. One of the most promising hallmarks of the HaloTag labeling strategy is its compatibility with intracellular protein labeling. To evaluate whether QD-HTLs can be used to directly target intracellular proteins, QD-HTLs would first need to be successfully delivered intracellularly and found to be freely diffusing inside the cytoplasm. We have already shown that our size-minimized multidentate polymer coated QDs can be successfully delivered monodispersely into cell cytoplasms using pinocytic loading (Chapter 3). Our studies have also shown that red core-shell QD-HTL conjugates coated with 1000 MW PEG are ~12 nm in hydrodynamic diameter (Chapter 4), thus meeting the general size requirement for free diffusion on cellular interiors (Chapter 3) [3, 106]. As shown in Chapter 4, another promising observation is that these PEG-QD-HTL conjugates exhibit minimal nonspecific binding to whole cell lysates.

One of the fundamental obstacles to intracellular QD targeting is the impossibility of removing unbound QDs from intracellular compartments. Since QDs are membrane-impermeable and cannot be washed out like fluorescent dyes, it is advantageous to pick a system in which a hallmark behavior can be used to distinguish QDs that are bound to their target from those that are not. For example, Courty and coworkers utilized the stepwise processivity of QD-kinesin conjugates to evaluate successful targeting to

microtubules. Through their linear directed motions, microtubule-bound QD-kinesins could be distinguished from unbound QD-kinesins freely diffusing in the cytoplasm [89].

Los and coworkers have already developed a model system utilizing the TNFα/NF-κB pathway that can potentially be used to evaluate intracellular targeting of QD-HTLs. Upon binding of the proinflammatory cytokine TNFα to its receptor, NF-κB, is released from cytosolic sequestration and freely moves into the nucleus to induce transcription of genes encoding various inflammatory cytokines [195]. NF-κB is a heterodimer composed of two subunits, p65 and p50. In a 2008 study performed by Los et al. the HaloTag protein was successfully fused to p65 and imaged with TMR ligand using traditional ensemble imaging methods. Upon addition of TNFα to the cellular medium, the TMR signal could be observed to shift from the cytosol to the nucleus [40].

The p65-HaloTag fusion is a promising candidate for pilot intracellular QD-tracking studies. Previous literature reports have consistently indicated that QDs above 3 nm in size do not spontaneously move into the nucleus [32, 114, 115]. Hence, any translocation of QD-HTLs from the cytosol into the nucleus should theoretically be mediated by the p65-HaloTag fusion protein. It will be interesting to evaluate the direct intracellular targeting capabilities of QD-HTLs on this system and others like it.

Development of Orthogonal Labeling Strategies for Multiplexed Quantum Dot Imaging

One of the great advantages of QDs is their ability to be easily used in multiplexed assays and multi-color tracking experiments [21, 49]. Since all QDs intrinsically possess broad absorption bands and narrow emission bands, a single light source can be used to concurrently excite multiple QDs with different emission

wavelengths. As such, quantum dots of different colors can be used to label different proteins and their movements and interactions can be simultaneously tracked [79, 93, 196]. To facilitate multi-color tracking while yet harnessing the advantages of covalent, monovalent labeling, it would be advantageous to develop orthogonal QD labeling strategies compatible with the HaloTag technology. One of the most apparent choices for an orthogonal labeling strategy would be to use the SNAP-Tag, a 20 kDa mutant form of the human DNA repair protein O^6-alkylguanine-DNA-alkyltransferase (hAGT), which reacts covalently with the nucleobase O^6-benzylguanine (BG) [126]. Like the HaloTag strategy, the SNAP-Tag strategy is compatible with intracellular labeling. QDs functionalized with BG ligands can bind covalently to cellular target proteins expressing a SNAP-Tag fusion in the same manner that QD-HTLs bind to HaloTag fusion proteins. One early study has shown that commercial QDs functionalized with BG molecules exhibit binding to purified SNAP-Tag proteins *in vitro*, although the reaction remains to be optimized [127]. We expect that many of the parameters used to optimize QD-HTL binding to cells would also apply to QD-benzylguanine conjugates.

Non-Blinking Quantum Dots for Single-Molecule Imaging

While the hallmark blinking characteristic of QDs facilitates the identification of single QDs, it also poses challenges for reconstructing trajectories. When blinking QDs are used for cellular imaging, QDs that are in their "off-state" cannot be distinguished from QDs transiently diffusing out of the focal plane. As a result, it is especially difficult to perform 3-D tracking with blinking QDs [197]. 3-D tracking will become even more important for intracellular QD tracking, when diffusion is no longer as localized to a 2-D surface as it is with cell membrane diffusion.

Because of this, many research groups have set forth efforts to produce non-blinking QDs. Early studies showed that blinking could be greatly suppressed if very thick shells were grown on top of the quantum dot core. Although blinking could not be entirely abolished using this method, these thick-shelled QDs were found to be in their "on-state" for greater than 97% of the time [198, 199]. Unfortunately, the advantages of size-minimization discussed in this thesis are abolished when thick-shelled QDs are used (Chapter 3). Thus, while thick-shelled QDs can still be used for tracking membrane receptors in unconfined regions of the cell, their widespread applicability in live cell imaging remains limited.

Recently, Wang and coworkers published the first report of entirely non-blinking QDs. They found that blinking could be entirely eliminated if core-shell QDs were prepared with a smooth composition gradient from the core to the shell. Although this mechanism remains poorly understood and somewhat controversial, this work demonstrates progress towards producing nonblinking QDs at more compact sizes (<10 nm in diameter) [200].

As advances continue to be made in the development of non-blinking QDs, it will be interesting to incorporate non-blinking QDs with HaloTagging or other site-specific tagging strategies for single-molecule imaging.

Super-Resolution Live Cell Imaging

While the advent of QD technology has allowed researchers to visualize dynamic cellular events with much greater clarity than previously possible with fluorescent dyes, new opportunities now exist for imaging these events at an unprecedented resolution. Previously, fluorescence microscopy imaging techniques were limited in spatial

resolution to ~200 nm, but the recent emergence of super-resolution imaging has allowed researchers to overcome the diffraction limit of light [8].

Common super-resolution techniques used in cell biology include RESOLFT [201], STED [202], PALM [203], FPALM [204], and STORM [205]. Many of these techniques require the use of photoswitchable fluorophores in order to produce super-resolution images.

For example, the stochastic optical reconstruction microscopy (STORM), photoactivated localization microscopy (PALM) and fluorescence photoactivation localization microscopy (FPALM) techniques all function by stochastically switching on and off individual fluorophores. These techniques rely on the fact that the signal from a single fluorophore can be localized at up to 1 nm accuracy if no other fluorophores are emitting the same signal within 200 nm of its location [206]. If a photoswitchable fluorophore is used to stain a cellular structure, individual fluorophores can be stochastically turned on at low density and their positions can be recorded at single-digit nanometer accuracy. These fluorophores are then turned off and the process is repeated by stochastically activating another set of fluorophores. After numerous repetitions, the entire cellular structure can be resolved at single-digit nanometer accuracy [8].

In these techniques, the maximum spatial resolution achievable is directly determined by the photon output of the fluorophore [207]. In this regard, quantum dots are potentially great candidates for super-resolution imaging due to their high extinction coefficients and large quantum yields. Research in producing photoswitchable QDs has already begun. In 2008, Irvine et al. demonstrated that signal from manganese doped ZnSe QDs can be reversibly activated and depleted with up to 90% efficiency. The

authors were able to image clusters of these QDs *in vitro* using super-resolution RESOLFT imaging [208].

The possibility of using quantum dots for super-resolution imaging in living cells is an exciting frontier to be explored in years to come. In the future, we believe that continued improvements in quantum dot probe design will help extend their applicability into far-reaching areas of biology and medicine. Meanwhile, the developments presented here will help guide the design of next-generation nanoparticle-based imaging probes, enabling a new chapter of cellular and molecular discoveries to be written.

REFERENCES

1. Coons, A.H., H.J. Creech, and R.N. Jones, *Immunological properties of an antibody containing a fluorescent group.* Proceedings of the Society for Experimental Biology and Medicine, 1941. **47**(2): p. 200-202.

2. Shimomura, O., F.H. Johnson, and Y. Saiga, *Extraction, purification and properties of aequorin, a bioluminescent protein from luminous hydromedusan, aequorea.* Journal of Cellular and Comparative Physiology, 1962. **59**(3): p. 223-&.

3. Smith, A.M., M.M. Wen, and S. Nie, *Imaging dynamic cellular events with quantum dots The bright future.* Biochemist (London), 2010. **32**(3): p. 12.

4. Lackowiz, J.R., *Principles of Fluorescence Spectroscopy*. 3 ed. 2006, New York: Springer. 759-766.

5. Ambrose, E.J., *Surface contact microscope for the study of cell movements*. Nature, 1956. **178**(4543): p. 1194-1194.

6. Axelrod, D., *Cell-substrate contacts illuminated by total internal-reflection fluorescence.* Journal of Cell Biology, 1981. **89**(1): p. 141-145.

7. Sako, Y. and T. Yanagida, *Single-molecule visualization in cell biology.* Nature Cell Biology, 2003: p. SS1-SS5.

8. Fernandez-Suarez, M. and A.Y. Ting, *Fluorescent probes for super-resolution imaging in living cells.* Nature Reviews Molecular Cell Biology, 2008. **9**(12): p. 929-943.

9. Hell, S.W., *Far-field optical nanoscopy.* Science, 2007. **316**(5828): p. 1153-1158.

10. Howarth, M., et al., *Monovalent, reduced-size quantum dots for imaging receptors on living cells.* Nature Methods, 2008. **5**(5): p. 397-399.

11. Eggeling, C., et al., *Photobleaching of fluorescent dyes under conditions used for single-molecule detection: Evidence of two-step photolysis.* Analytical Chemistry, 1998. **70**(13): p. 2651-2659.

12. Smith, A.M. and S. Nie, *Next-generation quantum dots.* Nature Biotechnology, 2009. **27**(8): p. 732-733.

13. Smith, A.M., et al., *Bioconjugated quantum dots for in vivo molecular and cellular imaging.* Advanced Drug Delivery Reviews, 2008. **60**(11): p. 1226-1240.

14. Michalet, X., et al., *Quantum dots for live cells, in vivo imaging, and diagnostics.* Science, 2005. **307**(5709): p. 538-544.

15. Smith, A.M., et al., *Engineering luminescent quantum dots for In vivo molecular and cellular imaging.* Annals of Biomedical Engineering, 2006. **34**(1): p. 3-14.

16. Dubertret, B., et al., *In vivo imaging of quantum dots encapsulated in phospholipid micelles.* Science, 2002. **298**(5599): p. 1759-1762.

17. Gao, X.H., et al., *In vivo cancer targeting and imaging with semiconductor quantum dots.* Nature Biotechnology, 2004. **22**(8): p. 969-976.

18. Kim, S., et al., *Near-infrared fluorescent type II quantum dots for sentinel lymph node mapping.* Nature Biotechnology, 2004. **22**(1): p. 93-97.

19. Yezhelyev, M.V., et al., *In situ molecular profiling of breast cancer biomarkers with multicolor quantum dots.* Advanced Materials, 2007. **19**(20): p. 3146-+.

20. Yezhelyev, M.V., et al., *Emerging use of nanoparticles in diagnosis and treatment of breast cancer.* Lancet Oncology, 2006. **7**(8): p. 657-667.

21. Xing, Y., et al., *Bioconjugated quantum dots for multiplexed and quantitative immunohistochemistry.* Nature Protocols, 2007. **2**(5): p. 1152-1165.

22. Wu, X.Y., et al., *Immunofluorescent labeling of cancer marker Her2 and other cellular targets with semiconductor quantum dots.* Nature Biotechnology, 2003. **21**(1): p. 41-46.

23. Dahan, M., et al., *Diffusion dynamics of glycine receptors revealed by single-quantum dot tracking.* Science, 2003. **302**(5644): p. 442-445.

24. Lidke, D.S., et al., *Quantum dot ligands provide new insights into erbB/HER receptor-mediated signal transduction.* Nature Biotechnology, 2004. **22**(2): p. 198-203.

25. Young, S.H. and E. Rozengurt, *Qdot Nanocrystal Conjugates conjugated to bombesin or ANG II label the cognate G protein-coupled receptor in living cells.* American Journal of Physiology-Cell Physiology, 2006. **290**(3): p. C728-C732.

26. Echarte, M.M., et al., *Quantitative single particle tracking of NGF-receptor complexes: Transport is bidirectional but biased by longer retrograde run lengths.* Febs Letters, 2007. **581**(16): p. 2905-2913.

27. Rajan, S.S. and T.Q. Vu, *Quantum dots monitor TrkA receptor dynamics in the interior of neural PC12 cells.* Nano Letters, 2006. **6**(9): p. 2049-2059.

28. Chen, H.F., et al., *Altered membrane dynamics of quantum dot-conjugated integrins during osteogenic differentiation of human bone marrow derived progenitor cells.* Biophysical Journal, 2007. **92**(4): p. 1399-1408.

29. Lieleg, O., et al., *Specific integrin Labeling in living Celts using functionalized nanocrystals.* Small, 2007. **3**(9): p. 1560-1565.

30. Derfus, A.M., W.C.W. Chan, and S.N. Bhatia, *Intracellular delivery of quantum dots for live cell labeling and organelle tracking.* Advanced Materials, 2004. **16**(12): p. 961-+.

31. Ruan, G., et al., *Imaging and tracking of tat peptide-conjugated quantum dots in living cells: new insights into nanoparticle uptake, intracellular transport, and vesicle shedding.* Journal of the American Chemical Society, 2007. **129**(47): p. 14759-14766.

32. Nabiev, I., et al., *Nonfunctionalized nanocrystals can exploit a cell's active transport machinery delivering them to specific nuclear and cytoplasmic compartments.* Nano Letters, 2007. **7**(11): p. 3452-3461.

33. Duan, H.W. and S.M. Nie, *Cell-penetrating quantum dots based on multivalent and endosome-disrupting surface coatings.* Journal of the American Chemical Society, 2007. **129**(11): p. 3333-3338.

34. Howarth, M., et al., *Targeting quantum dots to surface proteins in living cells with biotin ligase.* Proceedings of the National Academy of Sciences of the United States of America, 2005. **102**(21): p. 7583-7588.

35. Hainfeld, J.F., et al., *Ni-NTA-gold clusters target his-tagged proteins.* Journal of Structural Biology, 1999. **127**(2): p. 185-198.

36. Soh, N., *Selective chemical labeling of proteins with small fluorescent molecules based on metal-chelation methodology.* Sensors, 2008. **8**(2): p. 1004-1024.

37. O'Hare, H.M., K. Johnsson, and A. Gautier, *Chemical probes shed light on protein function.* Current Opinion in Structural Biology, 2007. **17**(4): p. 488-494.

38. Marks, K.M. and G.P. Nolan, *Chemical labeling strategies for cell biology.* Nature Methods, 2006. **3**(8): p. 591-596.

39. Chen, I. and A.Y. Ting, *Site-specific labeling of proteins with small molecules in live cells.* Current Opinion in Biotechnology, 2005. **16**(1): p. 35-40.

40. Los, G.V., et al., *HatoTag: A novel protein labeling technology for cell imaging and protein analysis.* Acs Chemical Biology, 2008. **3**(6): p. 373-382.

41. Whitesides, G.M., *The 'right' size in nanobiotechnology.* Nature Biotechnology, 2003. **21**(10): p. 1161-1165.

42. Ferrari, M., *Cancer nanotechnology: Opportunities and challenges.* Nature Reviews Cancer, 2005. **5**(3): p. 161-171.

43. Schaller, R.D. and V.I. Klimov, *High efficiency carrier multiplication in PbSe nanocrystals: Implications for solar energy conversion.* Physical Review Letters, 2004. **92**(18).

44. Schaller, R.D., V.M. Agranovich, and V.I. Klimov, *High-efficiency carrier multiplication through direct photogeneration of multi-excitons via virtual single-exciton states.* Nature Physics, 2005. **1**(3): p. 189-194.

45. Bowers, M.J., J.R. McBride, and S.J. Rosenthal, *White-light emission from magic-sized cadmium selenide nanocrystals.* Journal of the American Chemical Society, 2005. **127**(44): p. 15378-15379.

46. Loss, D. and D.P. DiVincenzo, *Quantum computation with quantum dots.* Physical Review A, 1998. **57**(1): p. 120-126.

47. Medintz, I.L., et al., *Quantum dot bioconjugates for imaging, labelling and sensing.* Nature Materials, 2005. **4**(6): p. 435-446.

48. Chan, W.C.W., et al., *Luminescent quantum dots for multiplexed biological detection and imaging.* Current Opinion in Biotechnology, 2002. **13**(1): p. 40-46.

49. Arnspang, E.C., J.R. Brewer, and B.C. Lagerholm, *Multi-Color Single Particle Tracking with Quantum Dots.* Plos One, 2012. **7**(11).

50. Smith, A.M., et al., *Size-Minimized Quantum Dots for Molecular and Cellular Imaging*, in *Proceedings of the Nobel Symposium: Single Molecule Spectroscopy in Chemistry, Physics and Biology*. p. 187-201.

51. Smith, A.M. and S. Nie, *Minimizing the hydrodynamic size of quantum dots with multifunctional multidentate polymer ligands.* Journal of the American Chemical Society, 2008. **130**(34): p. 11278-+.

52. Kairdolf, B.A., et al., *Minimizing nonspecific cellular binding of quantum dots with hydroxyl-derivatizied surface coatings.* Analytical Chemistry, 2008. **80**(8): p. 3029-3034.

53. Liu, W., et al., *Compact biocompatible quantum dots functionalized for cellular imaging.* Journal of the American Chemical Society, 2008. **130**(4): p. 1274-1284.

54. Liu, W., et al., *Compact Biocompatible Quantum Dots via RAFT-Mediated Synthesis of Imidazole-Based Random Copolymer Ligand.* Journal of the American Chemical Society, 2010. **132**(2): p. 472-483.

55. Susumu, K., et al., *Enhancing the stability and biological functionalities of quantum dots via compact multifunctional ligands.* Journal of the American Chemical Society, 2007. **129**(45): p. 13987-13996.

56. Ekimov, A.I. and A.A. Onushchenko, *Quantum size effect in the optical-spectra of semiconductor micro-crystals.* Soviet Physics Semiconductors-Ussr, 1982. **16**(7): p. 775-778.

57. Efros, A.L., *Interband absorption of light in a semiconductor sphere.* Soviet Physics Semiconductors-Ussr, 1982. **16**(7): p. 772-775.

58. Bertino, M.F., et al., *Quantum dots by ultraviolet and x-ray lithography.* Nanotechnology, 2007. **18**(31).

59. Tachibana, K., T. Someya, and Y. Arakawa, *Nanometer-scale InGaN self-assembled quantum dots grown by metalorganic chemical vapor deposition.* Applied Physics Letters, 1999. **74**(3): p. 383-385.

60. Joyce, P.B., et al., *Effect of growth rate on the size, composition, and optical properties of InAs/GaAs quantum dots grown by molecular-beam epitaxy.* Physical Review B, 2000. **62**(16): p. 10891-10895.

61. Adelmann, C., et al., *Self-assembled InGaN quantum dots grown by molecular-beam epitaxy.* Applied Physics Letters, 2000. **76**(12): p. 1570-1572.

62. Murray, C.B., D.J. Norris, and M.G. Bawendi, *Synthesis and characterization of nearly monodisperse Cde (e = S, Se, Te) semiconductor nanocrystallites.* Journal of the American Chemical Society, 1993. **115**(19): p. 8706-8715.

63. Xie, R.G., et al., *Synthesis and characterization of highly luminescent CdSe-Core CdS/Zn0.5Cd0.5S/ZnS multishell nanocrystals.* Journal of the American Chemical Society, 2005. **127**(20): p. 7480-7488.

64. Talapin, D.V., et al., *CdSe/CdS/ZnS and CdSe/ZnSe/ZnS core-shell-shell nanocrystals.* Journal of Physical Chemistry B, 2004. **108**(49): p. 18826-18831.

65. Bleuse, J., S. Carayon, and P. Reiss, *Optical properties of core/multishell CdSe/Zn(S,Se) nanocrystals.* Physica E-Low-Dimensional Systems & Nanostructures, 2004. **21**(2-4): p. 331-335.

66. Li, J.J., et al., *Large-scale synthesis of nearly monodisperse CdSe/CdS core/shell nanocrystals using air-stable reagents via successive ion layer adsorption and reaction.* Journal of the American Chemical Society, 2003. **125**(41): p. 12567-12575.

67. Aldana, J., Y.A. Wang, and X.G. Peng, *Photochemical instability of CdSe nanocrystals coated by hydrophilic thiols.* Journal of the American Chemical Society, 2001. **123**(36): p. 8844-8850.

68. Ma, J., et al., *Photochemical instability of thiol-capped CdTe quantum dots in aqueous solution and living cells: Process and mechanism.* Journal of Physical Chemistry B, 2007. **111**(41): p. 12012-12016.

69. Pellegrino, T., et al., *Hydrophobic nanocrystals coated with an amphiphilic polymer shell: A general route to water soluble nanocrystals.* Nano Letters, 2004. **4**(4): p. 703-707.

70. Moffitt, M. and A. Eisenberg, *Size control of nanoparticles in semiconductor-polymer composites .1. control via multiplet aggregation numbers in styrene-based random ionomers.* Chemistry of Materials, 1995. **7**(6): p. 1178-1184.

71. Smith, A.M. and S.M. Nie, *Chemical analysis and cellular imaging with quantum dots.* Analyst, 2004. **129**(8): p. 672-677.

72. Hermanson, G.T., *Bioconjugate Techniques*. 1st ed. 1996, London: Elsevier.

73. Yezhelyev, M.V., et al., *Proton-sponge coated quantum dots for siRNA delivery and intracellular imaging.* Journal of the American Chemical Society, 2008. **130**(28): p. 9006-9012.

74. Medintz, I.L., et al., *Self-assembled nanoscale biosensors based on quantum dot FRET donors.* Nature Materials, 2003. **2**(9): p. 630-638.

75. Ojida, A., et al., *Oligo-Asp Tag/Zn(II) complex probe as a new pair for labeling and fluorescence imaging of proteins.* Journal of the American Chemical Society, 2006. **128**(32): p. 10452-10459.

76. Green, N.M., *Avidin and streptavidin.* Methods in Enzymology, 1990. **184**: p. 51-67.

77. Choi, H.S., et al., *Renal clearance of quantum dots.* Nature Biotechnology, 2007. **25**(10): p. 1165-1170.

78. Nirmal, M., et al., *Fluorescence intermittency in single cadmium selenide nanocrystals.* Nature, 1996. **383**(6603): p. 802-804.

79. Lidke, D.S., et al., *Reaching out for signals: filopodia sense EGF and respond by directed retrograde transport of activated receptors.* Journal of Cell Biology, 2005. **170**(4): p. 619-626.

80. O'Connell, K.M.S., et al., *Kv2.1 potassium channels are retained within dynamic cell surface microdomains that are defined by a perimeter fence.* Journal of Neuroscience, 2006. **26**(38): p. 9609-9618.

81. Tamkun, M.M., K.M.S. O'Connell, and A.S. Rolig, *A cytoskeletal-based perimeter fence selectively corrals a sub-population of cell surface Kv2.1 channels.* Journal of Cell Science, 2007. **120**(14): p. 2413-2423.

82. Crane, J.M., et al., *Aquaporin-4 dynamics in orthogonal Arrays in live cells visualized by quantum dot single particle tracking.* Molecular Biology of the Cell, 2008. **19**(8): p. 3369-3378.

83. Crane, J.M. and A.S. Verkman, *Long-range nonanomalous diffusion of quantum dot-labeled aquaporin-1 water channels in the cell plasma membrane.* Biophysical Journal, 2008. **94**(2): p. 702-713.

84. Groc, L., et al., *Surface trafficking of neurotransmitter receptor: Comparison between single-molecule/quantum dot strategies.* Journal of Neuroscience, 2007. **27**(46): p. 12433-12437.

85. Heine, M., et al., *Surface mobility of postsynaptic AMPARs tunes synaptic transmission.* Science, 2008. **320**(5873): p. 201-205.

86. Levi, S., et al., *Homeostatic regulation of synaptic GlyR numbers driven by lateral diffusion.* Neuron, 2008. **59**(2): p. 261-273.

87. Groc, L., et al., *NMDA receptor surface mobility depends on NR2A-2B subunits.* Proceedings of the National Academy of Sciences of the United States of America, 2006. **103**(49): p. 18769-18774.

88. Geng, L., et al., *Transmembrane mechanisms in the assembly of the postsynaptic apparatus at the neuromuscular junction.* Chemico-Biological Interactions, 2008. **175**(1-3): p. 108-112.

89. Courty, S., et al., *Tracking individual kinesin motors in living cells using single quantum-dot imaging.* Nano Letters, 2006. **6**(7): p. 1491-1495.

90. Pierobon, P., et al., *Velocity, Processivity, and Individual Steps of Single Myosin V Molecules in Live Cells.* Biophysical Journal, 2009. **96**(10): p. 4268-4275.

91. Ribrault, C., K. Sekimoto, and A. Triller, *From the stochasticity of molecular processes to the variability of synaptic transmission.* Nature Reviews Neuroscience, 2011. **12**(7): p. 375-387.

92. Delehanty, J.B., H. Mattoussi, and I.L. Medintz, *Delivering quantum dots into cells: strategies, progress and remaining issues.* Analytical and Bioanalytical Chemistry, 2009. **393**(4): p. 1091-1105.

93. Roullier, V., et al., *High-Affinity Labeling and Tracking of Individual Histidine-Tagged Proteins in Live Cells Using Ni(2+) Tris-nitrilotriacetic Acid Quantum Dot Conjugates.* Nano Letters, 2009. **9**(3): p. 1228-1234.

94. Pinaud, F., et al., *Bioactivation and cell targeting of semiconductor CdSe/ZnS nanocrystals with phytochelatin-related peptides.* Journal of the American Chemical Society, 2004. **126**(19): p. 6115-6123.

95. Dif, A., et al., *Small and Stable Peptidic PEGylated Quantum Dots to Target Polyhistidine-Tagged Proteins with Controlled Stoichiometry.* Journal of the American Chemical Society, 2009. **131**(41): p. 14738-14746.

96. Clarke, S., et al., *Covalent Monofunctionalization of Peptide-Coated Quantum Dots for Single-Molecule Assays.* Nano Letters, 2010. **10**(6): p. 2147-2154.

97. Bruchez, M., et al., *Semiconductor nanocrystals as fluorescent biological labels.* Science, 1998. **281**(5385): p. 2013-2016.

98. Chan, W.C.W. and S.M. Nie, *Quantum dot bioconjugates for ultrasensitive nonisotopic detection.* Science, 1998. **281**(5385): p. 2016-2018.

99. Albanese, A., P.S. Tang, and W.C.W. Chan, *The Effect of Nanoparticle Size, Shape, and Surface Chemistry on Biological Systems.* Annual Review of Biomedical Engineering, Vol 14, 2012. **14**: p. 1-16.

100. Chithrani, B.D., A.A. Ghazani, and W.C.W. Chan, *Determining the size and shape dependence of gold nanoparticle uptake into mammalian cells.* Nano Letters, 2006. **6**(4): p. 662-668.

101. Jiang, W., et al., *Nanoparticle-mediated cellular response is size-dependent.* Nature Nanotechnology, 2008. **3**(3): p. 145-150.

102. Park, M.V.D.Z., et al., *The effect of particle size on the cytotoxicity, inflammation, developmental toxicity and genotoxicity of silver nanoparticles.* Biomaterials, 2011. **32**(36): p. 9810-9817.

103. Perrault, S.D., et al., *Mediating Tumor Targeting Efficiency of Nanoparticles Through Design.* Nano Letters, 2009. **9**(5): p. 1909-1915.

104. Huang, K., et al., *Size-Dependent Localization and Penetration of Ultrasmall Gold Nanoparticles in Cancer Cells, Multicellular Spheroids, and Tumors in Vivo.* Acs Nano, 2012. **6**(5): p. 4483-4493.

105. Luby-Phelps, K., *Cytoarchitecture and physical properties of cytoplasm: Volume, viscosity. diffusion, intracellular surface area.* International Review of Cytology - a Survey of Cell Biology, Vol 192, 2000. **192**: p. 189-221.

106. Verkman, A.S., *Solute and macromolecule diffusion in cellular aqueous compartments.* Trends in Biochemical Sciences, 2002. **27**(1): p. 27-33.

107. Fulton, A.B., *How crowded is the cytoplasm.* Cell, 1982. **30**(2): p. 345-347.

108. Goodsell, D.S., *The Machinery of Life* 1993 New York Springer-Verlag.

109. Lubyphelps, K., et al., *Hindered diffusion of inert tracer particles in the cytoplasm of mouse 3T3 cells.* Proceedings of the National Academy of Sciences of the United States of America, 1987. **84**(14): p. 4910-4913.

110. Popov, S. and M.M. Poo, *Diffusional transport of macromolecules in developing nerve processes.* Journal of Neuroscience, 1992. **12**(1): p. 77-85.

111. Seksek, O., J. Biwersi, and A.S. Verkman, *Translational diffusion of macromolecule-sized solutes in cytoplasm and nucleus.* Journal of Cell Biology, 1997. **138**(1): p. 131-142.

112. ArrioDupont, M., et al., *Mobility of creatine phosphokinase and beta-enolase in cultured muscle cells.* Biophysical Journal, 1997. **73**(5): p. 2667-2673.

113. Okada, C.Y. and M. Rechsteiner, *Introduction of macromolecules into cultured mammalian-cells by osmotic lysis of pinocytic vesicles.* Cell, 1982. **29**(1): p. 33-41.

114. Lovric, J., et al., *Differences in subcellular distribution and toxicity of green and red emitting CdTe quantum dots.* Journal of Molecular Medicine-Jmm, 2005. **83**(5): p. 377-385.

115. Williams, Y., et al., *Probing Cell-Type-Specific Intracellular Nanoscale Barriers Using Size-Tuned Quantum Dots.* Small, 2009. **5**(22): p. 2581-2588.

116. Xu, Y., et al., *Cell nucleus penetration by quantum dots induced by nuclear staining organic fluorophore and UV-irradiation.* Advanced Materials, 2008. **20**(18): p. 3468-+.

117. Weis, K., *Regulating access to the genome: Nucleocytoplasmic transport throughout the cell cycle.* Cell, 2003. **112**(4): p. 441-451.

118. Smith, A.M., *Engineering semiconductor nanocrystals for molecular, cellular, and in vivo imaging*. Ph.D. Thesis, 2008, Georgia Institute of Technology.

119. Algar, W.R. and U.J. Krull, *Adsorption and hybridization of oligonucleotides on mercaptoacetic acid-capped CdSe/ZnS quantum dots and quantum dot-oligonucleotide conjugates.* Langmuir, 2006. **22**(26): p. 11346-11352.

120. Doose, S., et al., *Comparison of photophysical and colloidal properties of biocompatible semiconductor nanocrystals using fluorescence correlation spectroscopy.* Analytical Chemistry, 2005. **77**(7): p. 2235-2242.

121. Medintz, I.L., et al., *A fluorescence resonance energy transfer-derived structure of a quantum dot-protein bioconjugate nanoassembly.* Proceedings of the National Academy of Sciences of the United States of America, 2004. **101**(26): p. 9612-9617.

122. Sapsford, K.E., et al., *Kinetics of metal-affinity driven self-assembly between proteins or peptides and CdSe-ZnS quantum dots.* Journal of Physical Chemistry C, 2007. **111**(31): p. 11528-11538.

123. Clapp, A.R., et al., *Two-photon excitation of quantum-dot-based fluorescence resonance energy transfer and its applications.* Advanced Materials, 2007. **19**(15): p. 1921-+.

124. Medintz, I.L., et al., *Intracellular delivery of quantum dot-protein cargos mediated by cell penetrating peptides.* Bioconjugate Chemistry, 2008. **19**(9): p. 1785-1795.

125. So, M.-K., H. Yao, and J. Rao, *HaloTag protein-mediated specific labeling of living cells with quantum dots.* Biochemical and Biophysical Research Communications, 2008. **374**(3): p. 419-423.

126. Keppler, A., et al., *A general method for the covalent labeling of fusion proteins with small molecules in vivo.* Nature Biotechnology, 2003. **21**(1): p. 86-89.

127. Petershans, A., D. Wedlich, and L. Fruk, *Bioconjugation of CdSe/ZnS nanoparticles with SNAP tagged proteins.* Chemical Communications, 2011. **47**(38): p. 10671-10673.

128. Bonasio, R., et al., *Specific and covalent labeling of a membrane protein with organic fluorochromes and quantum dots.* Proceedings of the National Academy of Sciences of the United States of America, 2007. **104**(37): p. 14753-14758.

129. Griffin, B.A., S.R. Adams, and R.Y. Tsien, *Specific covalent labeling of recombinant protein molecules inside live cells.* Science, 1998. **281**(5374): p. 269-272.

130. Gautier, A., et al., *An engineered protein tag for multiprotein labeling in living cells.* Chemistry & Biology, 2008. **15**(2): p. 128-136.

131. George, N., et al., *Specific labeling of cell surface proteins with chemically diverse compounds.* Journal of the American Chemical Society, 2004. **126**(29): p. 8896-8897.

132. Iyer, G., et al., *High Affinity scFv-Hapten Pair as a Tool for Quantum Dot Labeling and Tracking of Single Proteins in Live Cells.* Nano Letters, 2008. **8**(12): p. 4618-4623.

133. Charalambous, A., M. Andreou, and P.A. Skourides, *Intein-mediated site-specific conjugation of Quantum Dots to proteins in vivo.* Journal of Nanobiotechnology, 2009. **7**: p. 9-Article No.: 9.

134. Genin, E., et al., *CrAsH-quantum dot nanohybrids for smart targeting of proteins.* Journal of the American Chemical Society, 2008. **130**(27): p. 8596-+.

135. Bernardin, A., et al., *Copper-Free Click Chemistry for Highly Luminescent Quantum Dot Conjugates: Application to in Vivo Metabolic Imaging.* Bioconjugate Chemistry, 2010. **21**(4): p. 583-588.

136. Han, H.-S., et al., *Development of a Bioorthogonal and Highly Efficient Conjugation Method for Quantum Dots Using Tetrazine-Norbornene Cycloaddition.* Journal of the American Chemical Society, 2010. **132**(23): p. 7838-+.

137. Svendsen, S., et al., *Spatial separation and bidirectional trafficking of proteins using a multi-functional reporter.* Bmc Cell Biology, 2008. **9**.

138. Straszewski-Chavez, S.L., et al., *XAF1 mediates tumor necrosis factor-alpha-induced apoptosis and X-linked inhibitor of apoptosis cleavage by acting through the mitochondrial pathway.* Journal of Biological Chemistry, 2007. **282**(17): p. 13059-13072.

139. Reck-Peterson, S.L., et al., *Single-molecule analysis of dynein processivity and stepping behavior.* Cell, 2006. **126**(2): p. 335-348.

140. Hasegawa, Y., et al., *Cell-based in vivo dual imaging probes using genetically expressed tags and chemical contrast agents.* Chemical Communications, 2009(27): p. 4040-4042.

141. Kosaka, N., et al., *In Vivo Stable Tumor-Specific Painting in Various Colors Using Dehalogenase-Based Protein-Tag Fluorescent Ligands.* Bioconjugate Chemistry, 2009. **20**(7): p. 1367-1374.

142. He, Y.Z., et al., *Identification of a Lysosomal Pathway That Modulates Glucocorticoid Signaling and the Inflammatory Response.* Science Signaling, 2011. **4**(180).

143. Zhang, Y., et al., *HaloTag protein-mediated site-specific conjugation of bioluminescent proteins to quantum dots.* Angewandte Chemie-International Edition, 2006. **45**(30): p. 4936-4940.

144. Chen, O., et al., *Synthesis of Metal-Selenide Nanocrystals Using Selenium Dioxide as the Selenium Precursor.* Angewandte Chemie-International Edition, 2008. **47**(45): p. 8638-8641.

145. Yu, W.W., et al., *Experimental determination of the extinction coefficient of CdTe, CdSe, and CdS nanocrystals.* Chemistry of Materials, 2003. **15**(14): p. 2854-2860.

146. Jasieniak, J., et al., *Re-examination of the Size-Dependent Absorption Properties of CdSe Quantum Dots.* Journal of Physical Chemistry C, 2009. **113**(45): p. 19468-19474.

147. Leatherdale, C.A., et al., *On the absorption cross section of CdSe nanocrystal quantum dots.* Journal of Physical Chemistry B, 2002. **106**(31): p. 7619-7622.

148. Ramirez, J.C., M. Sanchezchaves, and F. Arranz, *Dextran functionalized by 4-nitrophenyl carbonate groups - aminolysis reactions.* Angewandte Makromolekulare Chemie, 1995. **225**: p. 123-130.

149. Liβe, D., et al., *Selective Targeting of Fluorescent Nanoparticles to Proteins Inside Live Cells.* Angewandte Chemie-International Edition, 2011. **50**(40): p. 9352-9355.

150. *Fundamentals of Membrane Dialysis, Spectrum Labs*. [cited 2013 February]; Available from: http://www.spectrumlabs.com/dialysis/Fund.html.

151. Ratner, B.D., Allan S. Hoffman, Frederick J. Schoen, Jack E. Lemons ed. *Biomaterials Science:: An Introduction to Materials in Medicine* 1st ed. 1997, Academic Press: San Diego, California. 484

152. Jokerst, J.V., et al., *Nanoparticle PEGylation for imaging and therapy.* Nanomedicine, 2011. **6**(4): p. 715-728.

153. Shen, H., A.M. Jawaid, and P.T. Snee, *Poly(ethylene glycol) Carbodiimide Coupling Reagents for the Biological and Chemical Functionalization of Water-Soluble Nanoparticles.* Acs Nano, 2009. **3**(4): p. 915-923.

154. Bentzen, E.L., et al., *Surface modification to reduce nonspecific binding of quantum dots in live cell assays.* Bioconjugate Chemistry, 2005. **16**(6): p. 1488-1494.

155. Smith, A.M. and S. Nie, *Compact quantum dots for single-molecule imaging.* J Vis Exp, 2012(68).

156. Jokerst, J.V., et al., *Affibody-Functionalized Gold-Silica Nanoparticles for Raman Molecular Imaging of the Epidermal Growth Factor Receptor.* Small, 2011. **7**(5): p. 625-633.

157. Demers, L.M., et al., *A fluorescence-based method for determining the surface coverage and hybridization efficiency of thiol-capped oligonucleotides bound to gold thin films and nanoparticles.* Analytical Chemistry, 2000. **72**(22): p. 5535-5541.

158. Huang, X.H., et al., *A Reexamination of Active and Passive Tumor Targeting by Using Rod-Shaped Gold Nanocrystals and Covalently Conjugated Peptide Ligands.* Acs Nano, 2010. **4**(10): p. 5887-5896.

159. Garcia-Fuentes, M., et al., *Application of NMR spectroscopy to the characterization of PEG-stabilized lipid nanoparticles.* Langmuir, 2004. **20**(20): p. 8839-8845.

160. Barzykin, A.V., V.F. Razumov, and M.V. Alfimov, *Fluorescence concentration self-quenching dynamics in monodisperse micellar systems.* Journal of Physical Chemistry, 1991. **95**(12): p. 4814-4818.

161. Udenfriend, S., et al., *Fluorescamine - reagent for assay of amino-acids, peptides, proteins, and primary amines in picomole range.* Science, 1972. **178**(4063): p. 871-&.

162. *Fluorescence Resonance Energy Transfer (FRET)—Note 1.2, Life Technologies*. [cited 2013 February]; Available from: http://www.invitrogen.com/site/us/en/home/References/Molecular-Probes-The-Handbook/Technical-Notes-and-Product-Highlights/Fluorescence-Resonance-Energy-Transfer-FRET.html.

163. Clapp, A.R., et al., *Can luminescent quantum dots be efficient energy acceptors with organic dye donors?* Journal of the American Chemical Society, 2005. **127**(4): p. 1242-1250.

164. *HaloTag Technology: Focus on Imaging Protocol*. [cited 2013 February]; Available from: http://www.promega.com/resources/protocols/technical-manuals/0/halotag-technology-focus-on-imaging-protocol/.

165. Hood, J.D. and D.A. Cheresh, *Role of integrins in cell invasion and migration.* Nature Reviews Cancer, 2002. **2**(2): p. 91-+.

166. Mizejewski, G.J., *Role of integrins in cancer: Survey of expression patterns.* Proceedings of the Society for Experimental Biology and Medicine, 1999. **222**(2): p. 124-138.

167. Miyanaga, Y., S. Matsuoka, and M. Ueda, *Single-Molecule Imaging Techniques to Visualize Chemotactic Signaling Events on the Membrane of Living Dictyostelium Cells*, in *Chemotaxis: Methods and Protocols*, T. Jin and D. Hereld, Editors. 2009. p. 417-435.

168. Lauffenberger, D.A., *Receptors: Models for Binding, Trafficking, and Signaling*. 1996, New York: Oxford University Press, Inc. .

169. Weigel, P.H. and J.A. Oka, *Endocytosis and degradation mediated by the asialoglycoprotein receptor in isolated rat hepatocytes.* Journal of Biological Chemistry, 1982. **257**(3): p. 1201-1207.

170. Tomoda, H., Y. Kishimoto, and Y.C. Lee, *Temperature effect on endocytosis and exocytosis by rabbit alveolar macrophages.* Journal of Biological Chemistry, 1989. **264**(26): p. 15445-15450.

171. *Temperature Effects (Introduction to Enzymes) - Worthington Biochemical Corporation*. [cited 2013 February]; Available from: http://www.worthington-biochem.com/introbiochem/tempeffects.html.

172. Bannai, H., et al., *Imaging the lateral diffusion of membrane molecules with quantum dots.* Nature Protocols, 2006. **1**(6): p. 2628-2634.

173. Pinaud, F., et al., *Probing cellular events, one quantum dot at a time.* Nature Methods, 2010. **7**(4): p. 275-285.

174. Nielsen, S.S., *Food Analysis*. 4th ed. 2010, New York: Springer.

175. Ehrlich, P.H., *Effect of multivalency on the specificity of protein and cell-interactions.* Journal of Theoretical Biology, 1979. **81**(1): p. 123-127.

176. Wang, J., et al., *The Complex Role of Multivalency in Nanoparticles Targeting the Transferrin Receptor for Cancer Therapies.* Journal of the American Chemical Society, 2010. **132**(32): p. 11306-11313.

177. Escorcia, F.E., et al., *Targeted nanomaterials for radiotherapy.* Nanomedicine (Lond), 2007. **2**(6): p. 805-15.

178. Byrne, J.D., T. Betancourt, and L. Brannon-Peppas, *Active targeting schemes for nanoparticle systems in cancer therapeutics.* Adv Drug Deliv Rev, 2008. **60**(15): p. 1615-26.

179. Ueda, M., et al., *Single-molecule analysis of chemotactic signaling in Dictyostelium cells.* Science, 2001. **294**(5543): p. 864-867.

180. *MacBiophotonics, McMaster University Biophotonics Facility*. [cited 2013 February]; Available from: http://www.macbiophotonics.ca/downloads.htm.

181. *Tracking Software - The Rowland Institute at Harvard*. [cited 2013 February]; Available from: http://www.rowland.harvard.edu/labs/bacteria/software/index.php.

182. *Manual Tracking Plugin*. [cited 2013 February]; Available from: http://rsbweb.nih.gov/ij/plugins/track/Manual%20Tracking%20plugin.pdf.

183. Murphy, D.B., *Fundamentals of Light Microscopy and Electronic Imaging*. 1st ed. 2001, New York: Wiley-Liss.

184. Bonneau, S., et al., *A multiple target approach for single quantum dot tracking,* in *2004 2nd IEEE International Symposium On Biomedical Imaging: Macro To Nano, VOLS 1 and 2*. 2004. p. 664-667.

185. Bonneau, S., M. Dahan, and L.D. Cohen, *Single quantum dot tracking based on perceptual grouping using minimal paths in a spatiotemporal volume.* IEEE Transactions on Image Processing, 2005. **14**(9): p. 1384-1395.

186. Serge, A., et al., *Dynamic multiple-target tracing to probe spatiotemporal cartography of cell membranes.* Nature Methods, 2008. **5**(8): p. 687-694.

187. Jaqaman, K., et al., *Robust single-particle tracking in live-cell time-lapse sequences.* Nature Methods, 2008. **5**(8): p. 695-702.

188. Meijering, E., I. Smal, and G. Danuser, *Tracking in molecular bioimaging.* Ieee Signal Processing Magazine, 2006. **23**(3): p. 46-53.

189. Courty, S., et al., *Tracking individual proteins in living cells using single quantum dot imaging,* in *Measuring Biological Responses with Automated Microscopy*. 2006. p. 211-228.

190. Saxton, M.J. and K. Jacobson, *Single-particle tracking: Applications to membrane dynamics.* Annual Review of Biophysics and Biomolecular Structure, 1997. **26**: p. 373-399.

191. Wieser, S. and G.J. Schuetz, *Tracking single molecules in the live cell plasma membrane-Do's and Don't's.* Methods, 2008. **46**(2): p. 131-140.

192. Qian, H., M.P. Sheetz, and E.L. Elson, *Single-particle tracking - analysis of diffusion and flow in 2-dimensional systems.* Biophysical Journal, 1991. **60**(4): p. 910-921.

193. Hirata, H., K. Ohki, and H. Miyata, *Mobility of integrin alpha 5 beta 1 measured on the isolated ventral membranes of human skin fibroblasts.* Biochimica Et Biophysica Acta-General Subjects, 2005. **1723**(1-3): p. 100-105.

194. Duband, J.L., et al., *Fibronectin receptor exhibits high lateral mobility in embryonic locomoting cells but is immobile in focal contacts and fibrillar streaks in stationary cells.* Journal of Cell Biology, 1988. **107**(4): p. 1385-1396.

195. Lodish, H., Arnold Berk, Chris A. Kaiser, Monty Krieger, Matthew P. Scott, Anthony Bretscher, Hidde Ploegh, Paul Matsudaira, *Molecular Cell Biology*. 6 ed. 2007, New York: W.H. Freeman. 973.

196. Gralle, M., M.G. Botelho, and F.S. Wouters, *Neuroprotective Secreted Amyloid Precursor Protein Acts by Disrupting Amyloid Precursor Protein Dimers.* Journal of Biological Chemistry, 2009. **284**(22): p. 15016-15025.

197. Marchuk, K., et al., *High-Precision Tracking with Non-blinking Quantum Dots Resolves Nanoscale Vertical Displacement.* Journal of the American Chemical Society, 2012. **134**(14): p. 6108-6111.

198. Chen, Y., et al., *"Giant" multishell CdSe nanocrystal quantum dots with suppressed blinking.* Journal of the American Chemical Society, 2008. **130**(15): p. 5026-+.

199. Mahler, B., et al., *Towards non-blinking colloidal quantum dots.* Nature Materials, 2008. **7**(8): p. 659-664.

200. Wang, X., et al., *Non-blinking semiconductor nanocrystals.* Nature, 2009. **459**(7247): p. 686-689.

201. Hofmann, M., et al., *Breaking the diffraction barrier in fluorescence microscopy at low light intensities by using reversibly photoswitchable proteins.* Proceedings of the National Academy of Sciences of the United States of America, 2005. **102**(49): p. 17565-17569.

202. Hell, S.W. and J. Wichmann, *Breaking the diffraction resolution limit by stimulated-emission - stimulated-emission-depletion fluorescence microscopy.* Optics Letters, 1994. **19**(11): p. 780-782.

203. Betzig, E., et al., *Imaging intracellular fluorescent proteins at nanometer resolution.* Science, 2006. **313**(5793): p. 1642-1645.

204. Hess, S.T., T.P.K. Girirajan, and M.D. Mason, *Ultra-high resolution imaging by fluorescence photoactivation localization microscopy.* Biophysical Journal, 2006. **91**(11): p. 4258-4272.

205. Rust, M.J., M. Bates, and X. Zhuang, *Sub-diffraction-limit imaging by stochastic optical reconstruction microscopy (STORM).* Nature Methods, 2006. **3**(10): p. 793-795.

206. Bobroff, N., *Position measurement with a resolution and noise-limited instrument.* Review of Scientific Instruments, 1986. **57**(6): p. 1152-1157.

207. Yildiz, A., et al., *Myosin V walks hand-over-hand: Single fluorophore imaging with 1.5-nm localization.* Science, 2003. **300**(5628): p. 2061-2065.

208. Irvine, S.E., et al., *Direct light-driven modulation of luminescence from Mn-doped ZnSe quantum dots.* Angewandte Chemie-International Edition, 2008. **47**(14): p. 2685-2688.